PIV-BASED EXAMINATION OF DYNAMIC STALL ON AN

OSCILLATING AIRFOIL

THESIS

Daniel E. Fredberg
Second Lieutenant, USAF

AFIT/GAE/ENY/08-M09

DEPARTMENT OF THE AIR FORCE
AIR UNIVERSITY

AIR FORCE INSTITUTE OF TECHNOLOGY

Wright-Patterson Air Force Base, Ohio

AFIT/GAE/ENY/08-M09

PIV-BASED EXAMINATION OF DYNAMIC STALL

ON AN OSCILLATING AIRFOIL

THESIS

Presented to the Faculty

Department of Aeronautics and Astronautics

Graduate School of Engineering Management

Air Force Institute of Technology

Air University

Air Education and Training Command

in Partial Fulfillment of the Requirements for the

Degree of Master of Science in Aeronautical Engineering

Daniel E. Fredberg, BS

Second Lieutenant, USAF

March 2008

PIV-BASED EXAMINATION OF DEEP STALL

ON AN OSCILLATING AIRFOIL

Daniel E. Fredberg, BS
Second Lieutenant, USAF

Approved:

_____   _____
Dr. Mark F. Reeder (Chairman)   11 Mar 08
                                          Date

_____   _____
Maj Andrew J. Lofthouse (Member)   11 Mar 08
                                          Date

_____   _____
Lt Col Raymond C. Maple (Member)   11 Mar 08
                                          Date

AFIT/GAE/ENY/08-M09

Abstract

A number of studies suggest that the deep stall flow fields produced by a pure-pitch and a pure-plunge oscillating airfoil are equivalent, when effective angles of attack are matched. This assumption is examined using particle image velocimetry (PIV). Sinusoidal oscillations of a pure-plunge and pure-pitch airfoil with matched reduced frequency k = 3.93 and with kinematically equivalent amplitudes of effective angle of attack are comparatively examined using results of PIV in a free surface water tunnel at AFRL/RB, Wright Patterson AFB. Experiments were conducted at Re = 10,000 and Re = 40,000, based on free stream velocity and airfoil chord, in order to observe the legitimacy of assuming Reynolds number insensitivity on the respective flow fields. Comparisons are made to computational flow field results collected in a separate, but coordinated, CFD effort. Results for both the pure-plunge case and the pure-pitch case confirm the Reynolds number insensitivity for the high frequency motions researched here. The resulting flow fields for pure-plunge case and the pure-pitch case were vastly different. Experimental results for the pure-plunge case closely resembled those achieved by computation. However, the pure-pitch case experimental and computation results were dissimilar even after considering possible wall effects of the water tunnel. The flow field disagreement between the two motions is not surprising considering trailing edge kinematic dissimilarities.

For my Wife and Daughter

You are my home and my motivation for all things.

Acknowledgements

Table of Contents

List of Figures

List of Tables

List of Symbols

A   characteristic width of the created jet flow [m]

b   distance from the leading edge [m]

c   chord length [m]

D displacement of particle [m]

f physical frequency [cycles/s]

h heave distance or displacement perpendicular to free stream [m]

h_o heave distance non-dimensionalized by the chord

k reduced frequency

Re   Reynolds number

St   Strouhal number

t   time [s]

u   velocity in free stream directions [m/s]

U_∞ free stream velocity [m/s]

v   velocity perpendicular to free stream [m/s]

$\vec{V}$ velocity [m/s]

$\vec{V}_a$ actual velocity of fluid [m/s]

v_{TEmax} maximum trailing edge velocity perpendicular to free stream flow [m/s]

$\vec{V}_{t.p.}$ velocity of tracer particle [m/s]

X   particle position [m]

α	angle of attack or effective incidence [radians]
α_o	offset angle or static angle of attack [radians]
θ	pitching amplitude [radians]
μ	dynamic viscosity [kg/m/s]
ρ	density [kg/m^3]
υ	kinematic viscosity [m^2/s]
φ_h	plunge phase angle [radians]
φ_θ	pitch phase angle [radians]
ω	frequency [cycles/s]
ω_z	vorticity [1/s]

1. Introduction

1.1. Motivation and Hypothesis

For thousands of years humankind has been fascinated with flight. Although many of the mysteries of flight have been answered by science and research, details of the sublimity for how creatures such as hummingbirds and dragonflies fly still fascinates and, to an extent, baffle scientist today. Better understanding of the aerodynamic phenomenon surrounding our winged earthly cohabitants would likely enable development in flight vehicles. This form of development is currently being sought by the Department of Defense (DoD), which is spending a great deal of funding and research on biometrically inspired flapping wing technology for micro air vehicles (MAV's) (Office of the Assistant Secretary of Defense, 1997).

One promising attribute of an oscillating airfoil is that it can theoretically achieve a very high propulsive efficiency. A wing has shown that, in steady forward motion and with steady-state flapping motion, it produces thrust in the form of a jet downstream of the trailing edge (Anderson, Streitlien, Barrett, & Trientafyllou, 1998). Efficiency of flight is critical to achieve for MAV's since size and fuel source are among the most important design parameters.

The flow fields created by a flapping, or oscillating, airfoil are highly complicated and are not fully understood by researchers and scientists. One aerodynamic phenomena contributing to the complexity of an oscillating airfoil, especially its application to

MAV's, is dynamic stall. On an oscillating airfoil the angle of incidence is changing rapidly, such that the onset stall can be delayed to an angle of attack significantly greater than where static stall would occur. Furthermore, dynamic stall is more severe and persistent than the stall of a static airfoil (McCroskey, 1981).

Dynamic stall regimes include light stall and deep stall. Light stall shares characteristics of classical static stall, whereas deep stall produces a dynamic stall, followed by a reattachment process. Deep stall has been experimentally characterized by the shedding and passing of vortex-like disturbances on the upper surface of the lifting surface, leading edge to trailing edge (Maresca, Favier, & Rebont, 1981). A potential benefit of dynamic stall is that the vortex structures present in dynamic stall affect the flow field such that a negative pressure region is formed, contributing to a lift much greater than the maximum lift experienced in steady flow (Wernert, Koerberg, Wietrich, Raffel, & and Kompenhans, 1997).

Experimentally observing and quantifying the complex flow fields of an airfoil in dynamic stall can be a difficult task. However, a water tunnel offers unique advantages to researchers as opposed to a wind tunnel. The significant benefits of using a water tunnel for dynamic testing are the reduced rate of the fluid and higher density. For a given Reynolds number, the velocity in a water tunnel is approximately one order of magnitude slower than in a wind tunnel. Furthermore, a water tunnel offers the ability to achieve a relatively low rate of physical motion for a given cycle, simplification in terms of inertial vs. aerodynamic effects, and simplicity of flow visualization by passive markers (dye) nominally tracking vortical structures [Kramer (2002), Erm (2006)]. The reduced physical frequency, in particular, is especially useful because one can examine

the anticipated vortex dominated flow fields of a high incidence oscillating airfoil over longer periods of time compared to that of a wind tunnel.

We are at an age where scientists and researchers have built and are improving mathematical models that can simulate the flow of fluids. These computational models have proven very useful and do not require the logistics and funding that a wind tunnel or water tunnel would require. However, the computational fluid dynamic (CFD) models and the assumption upon which they are built require validation. Such evidence is found by physical experimentation that can empirically confirm the CFD results.

Much effort has been placed in nonintrusive measures to gather results in order to increase our ability to better predict and understand the complex behavior of fluids. One nonintrusive technique commonly accepted and used to capture velocities in the flow field is particle image velocimetry (PIV). PIV, in its modern form, is described as an "accurate, quantitative measurement of fluid velocity vectors at a very large number of points simultaneously" (Adrian R. , 2005). PIV is accomplished by tracking indiscriminate particles in the flow at discrete points in time in order to find their velocity and direction. These particles are tracked using digital photographs at specific instances in time and then computationally examining the images to determine their velocity and direction. Titanium dioxide, TiO_2, is commonly used as tracer particles, or *seeds*, for water tunnel PIV because its size causes negligible disturbance to the fluid flow, and it can be effectively illuminated for PIV purposes. The resultant velocity vector maps and contour maps of PIV offer researches a valuable and quantifiable picture of fluid flow.

A study often referenced in regards to oscillating airfoils in deep stall was completed by McCroskey (1981). McCroskey claims that "common engineering practice

is to assume that the resulting flow fields and airloads (of plunging oscillations) are equivalent to those due to pitching oscillations" for airfoils in deep stall (1981). It is proposed that the accuracy of this assumption deserves further research into the similarities and/or dissimilarities of the resulting flow fields of the pure-pitch and pure-plunge sinusoidal oscillations of an airfoil. The comparison will be completed using a water tunnel PIV system. In a separate effort, CFD has been utilized to solve many of the same cases empirically examined in this research effort (McGowan, Gopalarathnam, Ol, Edwards, & Fredberg, 2008).

1.2. Research Focus and Goals

There are three main objectives for the PIV research detailed in this report. One is to examine the flow fields created by the pure-plunge and pure-pitch sinusoidal oscillations of an SD7003 airfoil (Selig, 2006), and to investigate the Reynolds number sensitivity of the resulting deep stall flow fields. The second is to empirically test the limitations of the engineering assumption that the 2-D deep stall flow fields of a pure-plunge case and pure-pitch case are equivalent when the effective incidence is matched (McCroskey, 1981). Lastly, to provide a baseline for comparison to CFD results of a separate coordinated effort. Given the benefits for dynamic experiments, PIV experiments were conducted in a water tunnel.

2. Background and Theory

2.1. Oscillating Airfoils

Two types of motion of an oscillating airfoil are pitching and plunging. Combining pitching and plunging for an oscillating airfoil can create innumerous flapping cases of interest for research. However, examining the two motions independently offers less complicated experiments that still offer a great deal of insight. Plunging refers to an airfoil in oscillation perpendicular to the undisturbed free stream flow at amplitude, h (Maresca, Favier, & Rebont, 1981). Pitching is the angular rotation, θ, of the airfoil oscillating about a certain point at distance, b, from the leading edge, typically the quarter-chord. Both pitching and plunging can be further offset by the static angle of attack of the airfoil, α_o. Figure 1 shows the definition of the principle motion parameters for an oscillating airfoil, plunge and pitch.
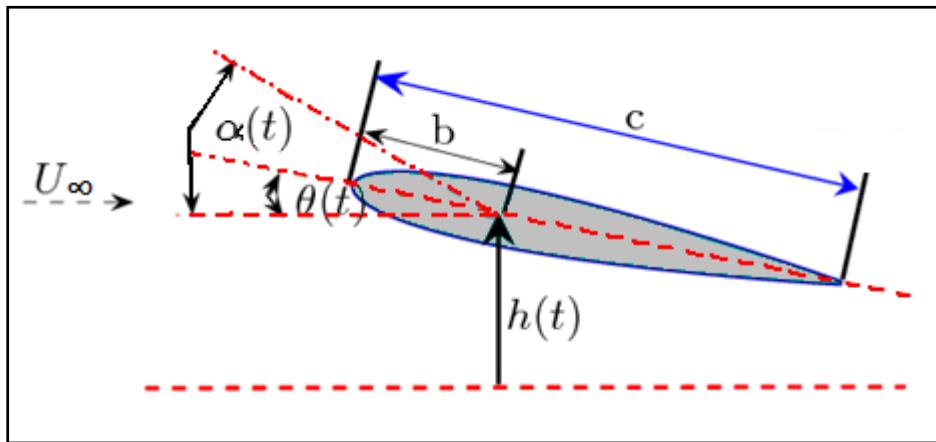
Figure 1: Principle motion parameters for oscillating airfoil; plunge h(t), pitch θ(t).

5

The kinematics for a pure-plunge case is defined by Equation1 (McGowan, Gopalarathnam, Ol, Edwards, & Fredberg, 2008).

$$h(t) = h_o c \, cos(\omega t + \varphi_h) \qquad (1)$$

$$\theta(t) = constant$$

where

h = plunge position (m)

h_o = plunging amplitude non-dimensionalized by the airfoil chord (unitless)

c = chord length (m)

ω = frequency (radians/s)

t = time (s)

φ_h = phase angle of the plunge (radians)

For the pure-pitch case, Equation 2 applies to the airfoil (McGowan, Gopalarathnam, Ol, Edwards, & Fredberg, 2008).

$$\theta(t) = \theta_o \, cos(\omega t + \varphi_\theta) + \alpha_o \qquad (2)$$

$$h(t) = constant$$

where

θ_o = pitching amplitude (radians)

φ_θ = phase angle of the pitch (radians)

α_o = offset angle, or static angle of attack (radians)

Although the kinematic motions of the plunge case are vastly different than those of the pitch case, under deep stall, it is commonly assumed that, with matched effective angles of attack, the resulting flow fields are equivalent according to McCroskey (1981). In order to properly investigate similarities and dissimilarities of each case it is important to find kinematic parameters that can be matched. Which parameters to match for a valid comparison remains ambiguous since there are many parameters used that have shown affects on deep stall flow fields. However, parameters often used when describing oscillating airfoils and considered for matching are reduced frequency, Strouhal number, and effective angle of attack [McCroskey (1981), Lian, Ol, Shyy (2008), Anderson, Streitlien, Barrett, & Trientafyllou (1998)]. The reduced frequency, k, is defined by Equation 3.

$$k = \frac{\omega c}{2U_\infty} \tag{3}$$

where

ω = frequency (radians/s)

k = reduced frequency (unitless)

U_∞ = free stream velocity (m/s)

c = chord (m)

and

$$\omega = 2\pi f \tag{4}$$

where

f = physical frequency of motion (cycles/s)

The physical frequency f can be thought of as the inverse of the time required to complete one phase or cycle. Therefore, for the plunge case the physical frequency is based upon one cycle, the translating motion perpendicular to the free stream flow. For the pitch case the physical frequency is based upon one cycle of rotational motion about the quarter-chord of the airfoil (Anderson, Streitlien, Barrett, & Trientafyllou, 1998). In a similar experiment examining a 2-D oscillating *and* translating airfoil, results showed that the reduced frequency was the dominant parameter of the flow [Ohmi, Coutanceau, Loc, & Dulieu (1990), Ohmi, Coutanceau, Daube, & Loc (1991)]. The reduced frequency for the pure-plunge case and pure-pitch case were matched in the current experiment.

Another non-dimensional frequency often referred to in regards to oscillating airfoils is the Strouhal number. The Strouhal, St, is defined by Equation 5 (Anderson, Streitlien, Barrett, & Trientafyllou, 1998).

$$St_A = \frac{fA}{U_\infty} \tag{5}$$

where

$$A = \text{characteristic width of the created jet flow (m)}$$

However, since the characteristic width of the created jet flow, A, is unknown prior to performing the experiment, it is taken to be equal to twice the heave amplitude (i.e. A = 2h) following Anderson et al (1998). Matching the Strouhal number can be disputed since heave amplitude is zero at the quarter-chord for a pure-pitch oscillation. For the pure-pitch case, the motion is based upon a rotation about the quarter-chord and not a translation, as in the plunge case. Any heave-type translation for the pitch case would

increase with the distance away from the quarter-chord, unraveling the matching of the reduced frequency based at the quarter-chord. Using the chord, c, as the length scale for the Strouhal number would only reproduce the reduced frequency, different only by a factor of π. However, using the trailing edge for the pitch-case (Anderson, Streitlien, Barrett, & Trientafyllou, 1998) can lead to a means for comparison between the pure plunge and pure pitch case, since the heave amplitude is constant for the pure-plunge along the chord. Therefore, Equation 6 shows the trailing edge's Strouhal number for the pure-plunge oscillating airfoil.

$$St_{T.E.\cdot h} = \frac{f(2h)}{U_\infty}$$
(6)

The trailing edge Strouhal number for the pure-pitch case is defined by Equation 7. In essence, the length scale for each Strouhal number is the vertical distance moved over one cycle.

$$St_{T.E.\cdot \theta} = \frac{2f\left(\theta_{\frac{3}{4}}c\right)}{U_\infty}$$
(7)

Lai and Platzer completed research examining the different flow fields of plunging airfoils, varying the maximum non-dimensional plunge velocity, kh_o (1999). The maximum non-dimensional plunge velocity is, in essence, equivalent to the Strouhal number for the pure-plunge case. The reduced frequency, k, term incorporates the physical frequency term, f, and the heave amplitude, h_o, as in the Strouhal number, but

non-dimensionalized by the chord. Furthermore, for a pure-pitch oscillating airfoil, the non-dimensional "plunge" velocity would have to be matched with a pure-plunge case at a location other than the quarter-chord of the airfoil, since it is not translating at that point. Although not matched in this research, using the trailing edge displacement as a value for h (i.e. $h_o = \frac{3}{4}\theta$ for pure-pitch case) to find kh_o for both the pure-plunge and pure pitch cases still offers a valuable tool for comparing the results of Lai and Platzer (1999) to some of those achieved in this research.

In order to relate the amplitude of the plunge case to the rotation of the pitch case, the kinematic angle of attack will be matched, as inferred by the dynamic stall literature (McCroskey, 1981). For the pitch case, the kinematic angle of attack time history α(t), shown in Equation 8, is based upon the geometric angle of attack about the offset angle α$_o$ (McGowan, Gopalarathnam, Ol, Edwards, & Fredberg, 2008).

$$\alpha(t) = \alpha_o + \theta_o \cos\left[\omega t + \varphi_\theta\right] \tag{8}$$

where

$$\theta_o = \text{geometric angle of attack}$$

The kinematic angle of attack time history for the plunge case, shown in Equation 9, is based upon the motion-induced angle of attack formed by the flow as a result of the plunge motion.

$$\propto (t) = \alpha_o + \arctan\left[\frac{\omega c h_o \left(t - \frac{\pi}{2}\right)}{U_\infty}\right] = \alpha_o + \arctan\left[2kh_o\left(t - \frac{\pi}{2}\right)\right] \tag{9}$$

In order to equate the geometric angle of attack of pitch with the plunge-induced angle of attack, Equation 10 was used.

$$\theta_o = arctan\left[2kh(t - \tfrac{\pi}{2})\right] \tag{10}$$

Therefore, the maximal extent of the pure-plunge case angle of attack is shown in Equation 11 and used to match the upper and lower bounds of $\alpha(t)$ to that of the pitch case (McGowan, Gopalarathnam, Ol, Edwards, & Fredberg, 2008).

$$\alpha_T = \alpha_o \pm arctan\left[2kh_o\right] \tag{11}$$

Following a previous plunge case experiment conducted at the Naval Postgraduate School (Lai & Platzer, 1999) in deep stall, the subsequent values will be used: $k = 3.93$, $h_o = 0.05$, and $\alpha_o = 4^o$ giving a $\alpha(t) = 4^o \pm 21.5^o cos(\omega t)$ for the pure-pitch cases, matched by the pure-plunge cases.

2.2.   Water Tunnel

For a dynamic experiment such as this one, there are a number of benefits to using a water tunnel. For example, when examining forces impinged on a test specimen by the flow, the same dynamic pressure can be achieved at a lower flow rate with a water tunnel compared to a wind tunnel. For a given Reynolds number, the flow speed is approximately one order of magnitude slower than that of a wind tunnel due to the lower kinematic viscosity of water. The Reynolds number, Re, for a 2-D airfoil is defined by Equation 12.

$$Re_c = \frac{cU_\infty}{\nu} \tag{12}$$

where

$$\nu = \text{kinematic viscosity (m}^2\text{/s)},$$

and

$$\nu = \frac{\mu}{\rho} \tag{13}$$

where

$$\rho = \text{density (kg/m}^3)$$

$$\mu = \text{dynamic viscosity (kg/m/s)}$$

This is useful for static experiments (i.e. airfoil sitting on a sting), but especially for dynamic experiments like that detailed in this report. Recalling the reduced frequency, having a slower free stream velocity means that the physical frequency can also be slower

without sacrificing a larger reduced frequency (i.e. a reduced frequency closer to what is experienced by a MAV with oscillating wings). The benefit of this is that, typically, as the physical frequency increases, so does the complexity of the apparatus and procedure for a dynamic experiment such as this one (i.e. flapping apparatus and PIV acquisition).

Furthermore, the use of water eases flow visualization (i.e. dye) and flow seeding (i.e. PIV) compared to a wind tunnel. Slower flow allows for better observation of flow visualization. In regards to PIV, the aforementioned lower physical frequency benefit of a water tunnel alleviates camera CCD refresh-rate and laser trigger timing issues. Also, the seeding apparatus and mixing are less of an issue since a running tunnel disperses the particles after only a short period of time.

Water tunnels also have certain experimental disadvantages, although most can be neglected with proper procedure. Given that water is corrosive, there are limitations to what materials can be used in the tunnel. Debris from corrosion or elsewhere can produce inaccurate results in experimental measurements (i.e. create disturbances in flow and problematic PIV measurements). The conductivity of water places constraints on parameters that can otherwise be measured in a wind tunnel, such as strain gage load measurements.

2.3.   PIV Overview

Particle image velocimetry (PIV) theory has been discussed, developed, and used for over 20 years (Adrian R. , 2005) as a tool for researchers to quantify flow fields. PIV can be described as the observation of particle flow images over a discrete time period with the purpose of attaining velocity vectors representing the flow field of a gas or liquid.

PIV data is collected using a camera to capture high resolution images of tracer particles illuminated by a planar stroboscopic light source, typically a high powered laser. Two images of the flow, taken at a desired time increment Δt apart, are used to measure the displacement of the tracer particle and indirectly solve for the velocity using Equation 14 (Westerweel, 1997).

$$D(X; t', t'') = \int_{t'}^{t''} \vec{V}_{t.p.}[X(t), t]dt \qquad \text{Equation (14)}$$

where

$$D = \text{the displacement of a particular seed particle}$$

$$\vec{V}_{t.p.}[X(t)] = \text{velocity of the tracer particles}$$

$$X = \text{position of seed}$$

$$t = \text{time (s)}$$

and

$$\Delta t = t'' - t'$$

Ideally tracer particles would precisely follow the motion of the fluid, would not create any disturbances in the flow, and would not interact with each other (Westerweel, 1997). However, the ideal tracer particle, or seed, concept can only be approximated since tracer particles have mass and inertia which affect their directional reaction time in the fluid. Tracer particles, unless perfect, have a slight delay in reaction to motions in the fluid, as shown in Figure 2.
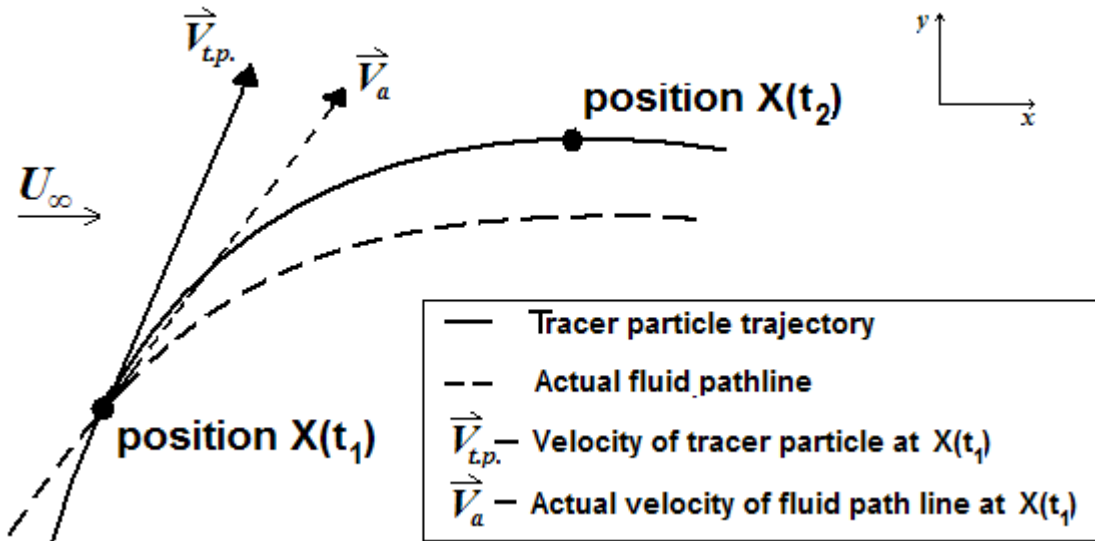
Figure 2: Displacement as it relates to the approximation of velocity for PIV.

Choosing a tracer particle for the flow requires a balance between a particle small enough to closely follow the motion of the flow and yet large enough to become suitably illuminated by the light source for photo recognition.

It is important to realize that PIV processing does not find the velocity and direction by tracing individual particles; instead the velocity is inferred by the

observation of the motion of the seed pattern over discrete subregions of the images. Tracer particles create a random pattern that is connected to flow, and the fluid motion is determined by visible changes to the tracer pattern, shown in Figure 3.
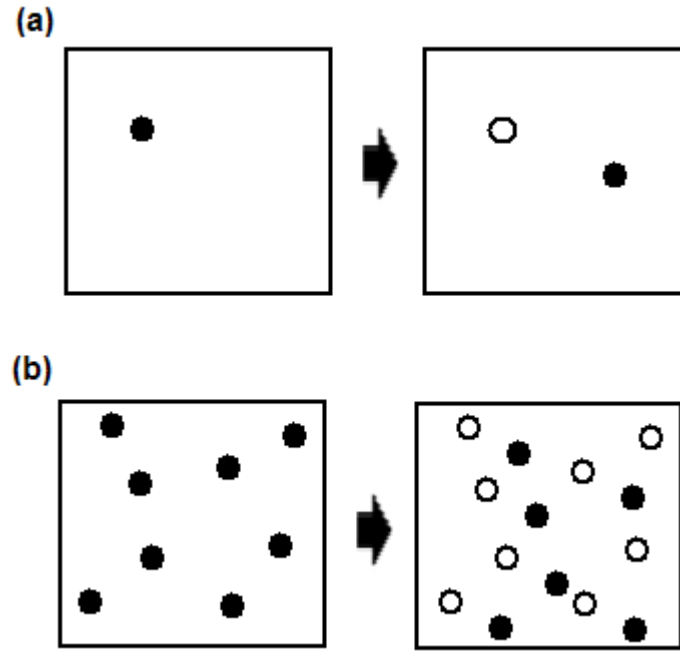
Figure 3: Comparison of (a) individual particle tracking vs. (b) tracer pattern changes.

The aforementioned observation is computationally performed in what is called interrogation regions (IR's), which are smaller regions of the entire image. For example, an eleven megapixel camera, as will be used in this experiment, takes a 2672x4008 pixel image. For PIV, this image would be broken down into multiple 16x16 pixel or 32x32 pixel subregions. Each subregion computation results in a vector that, over the entire flow field, creates a detailed velocity vector map of the flow.

The computations are completed by PIV processing software, developed by Jeon (2000), which takes the two images and converts them into two signals in the frequency

domain. The accuracy of the computations is dependent upon the existence of high cross-correlation signal peaks which appear when many particles from the subregion of image one match up with their spatially shifted equivalent in the same subregion of the second image. High contrast in the images between particles and the background produces a favorable signal-to-noise ratio (i.e. more distinct signal peaks). Having distinct particles in a PIV image (i.e. high signal-to-noise ratio) allows for higher accuracy in the cross-correlation solution. Inaccurate, or small signal peaks appear when individual particles from the subregion in the first image match up with different particles in the same subregion of the second image. Figure 4 shows an example of a cross correlation for a subregion (Willert & Gharib, 1991). The grid depicts pixels within a subregion and the high peaks represent the location of particles. The high peak of the cross-correlation represents the solution for displacement within the subregion. Surrounding lesser peaks represent noise within each image and in the cross-correlation solution.
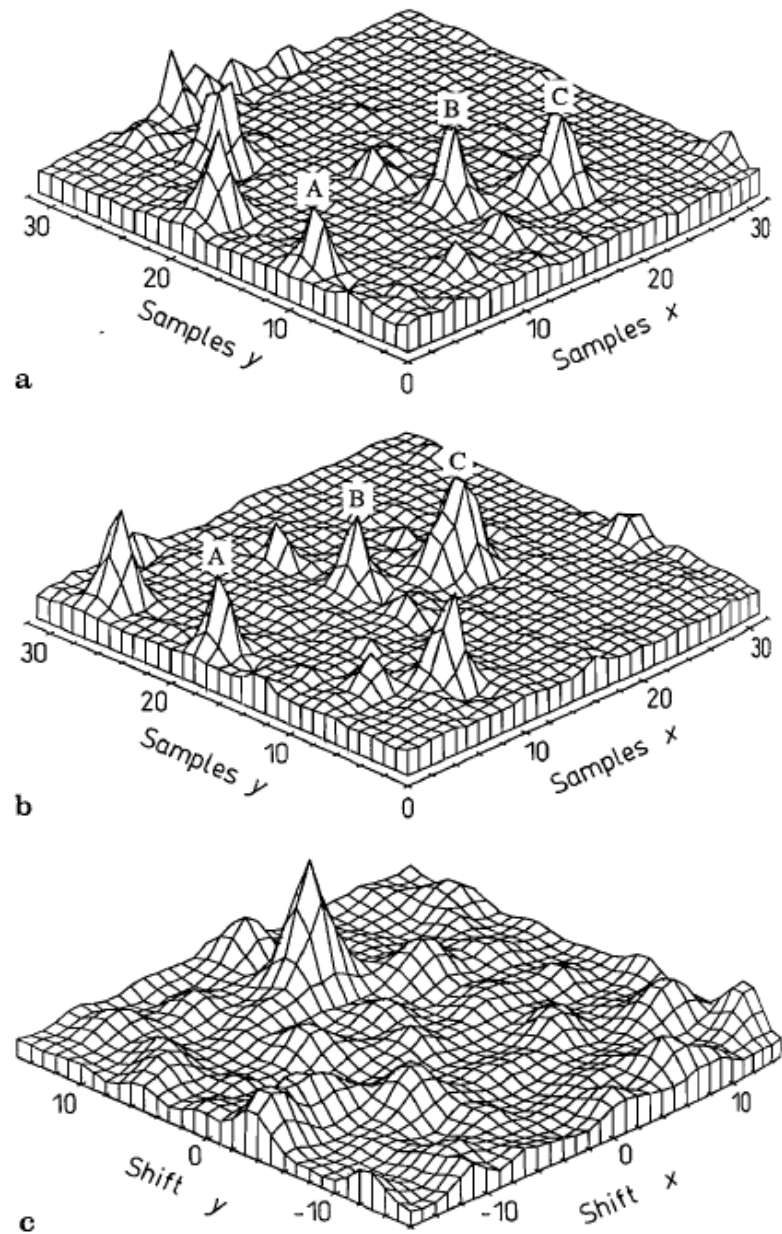
Figure 4: Particle intensities for a subregion of two images, (a) and (b), and their cross-correlation estimate (c) given a particle displacement of ~8 pixels in y (Willert & Gharib, 1991).

For each subregion, a 2-D cross-correlation is performed in order to determine the likely speed and direction of the flow. When deciding on the size of a subregion it is important to consider the distance a particle travels in a designated time increment in order to avoid significant signal drop out. Signal drop out refers to tracer particles in a subregion for the first image that are not present in the second image. Since a cross-correlation is calculated for each subregion, no correlation will be made for a particle present in only one of the two images. Instead, the missing particle from one subregion becomes noise for the neighboring subregion in which it enters, contributing to signal drop out. The errors attributed to signal drop out can be minimized by creating larger subregion's and estimating the velocity of a particle in the flow to ensure a sufficiently sized subregion for given tunnel speed. Also, overlapping the neighboring subregion by a certain percent can capture particles that travel distances that place them outside their original subregion. Using the overlapping technique produces more vectors than not overlapping since more effective subregions are examined (Jeon, 2000).

An example of the subregion solutions displayed in vector form can be seen in Figure 5, which shows results from a prior PIV experiment conducted to examine the water tunnel free stream velocity. Each vector represents the unique solution of a subregion.
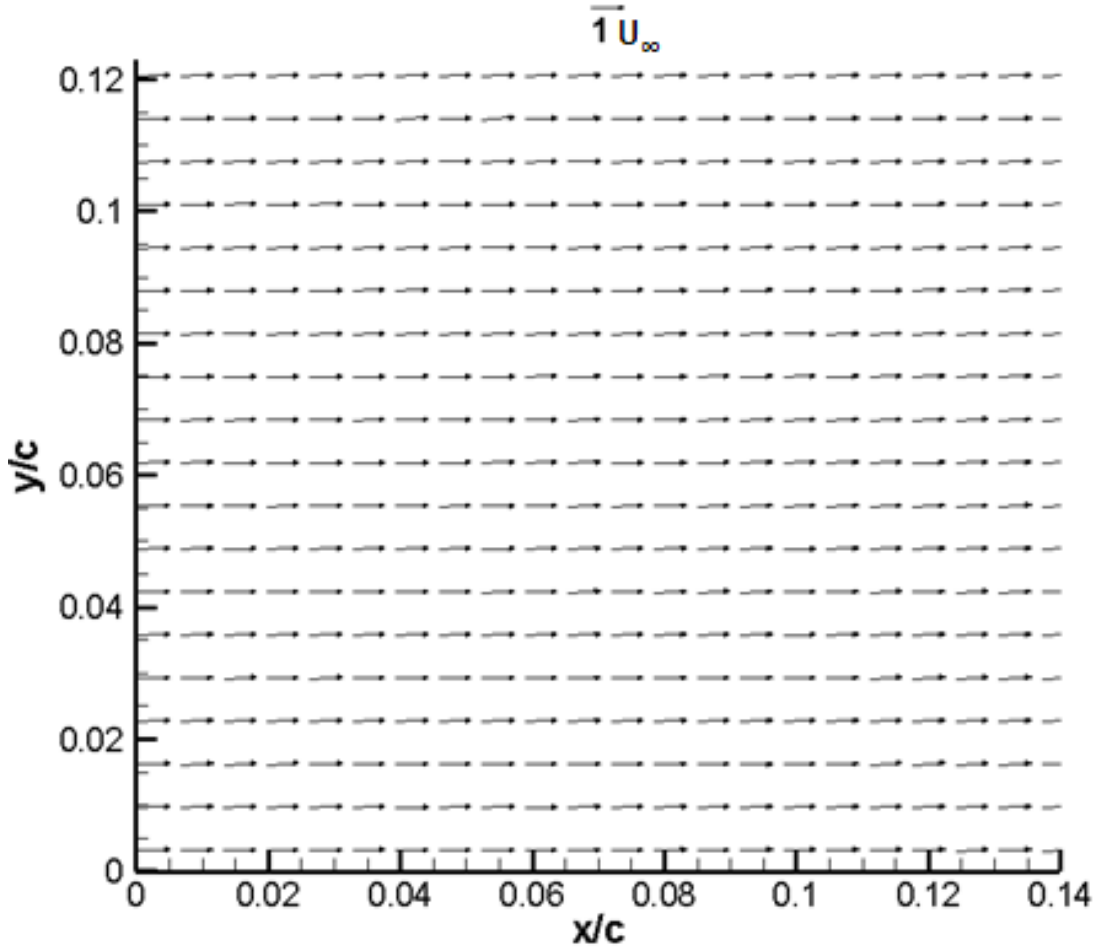
Figure 5: Free stream PIV velocity vector map taken for this experiment.

In Figure 5, as is typical with velocity vector maps, the magnitudes of the velocity vectors are non-dimensionalized by the free stream flow.

It is important to note that single image pair solution can have anomalies (i.e. due to turbulence, blooming, particle debris) that can affect their accuracy. Averaged velocity solutions of PIV, as shown in Figure 5, are not typically based on the solution of a single image pair, but instead on the average of many image pair solutions. Capturing numerous image pairs is necessary for an average flow field result. For dynamic

experiments, such as the one discussed in this report, it is important to average image pair results from the same phase of the motion. This is accomplished using phase-averaging. For each phase of interest, many image pairs are captured and processed to present an averaged result of the flow field. Phase averaging assumes the flow field is periodic.

Once the average velocities have been found, the average out of plane vorticity can be computed for using Equation 15 (Adrian, Gharib, Merzkirch, Rockwell, & Whitelaw, 1998).

$$\omega_z = \frac{\partial V}{\partial x} - \frac{\partial U}{\partial y} \qquad (15)$$

where

$$\omega_z = \text{vorticity component normal to the light sheet}$$

2.3.1. Illumination Source

The illumination source is one of the major components of any PIV system. Its primary purpose is to illuminate flowing seed particles so that images of the flow can be captured. The flow captured by the images need to appear frozen and not blurred in order to attain accurate PIV measurement. For dynamic experiments, such as the one detailed in this report, the pulsing of light is critical to precisely capturing the flow field. Furthermore, it is important to have a light source capable of delivering such a light pulse in rapid succession such that the particles in the two images provide a good cross-correlation for the PIV measurements. The time between each light pulse equivalent to and serves the same purpose as Δt in the PIV process. For this reason, pulsed lasers are

most commonly used for PIV illumination. Pulsed lasers satisfy the aforementioned requirements of a PIV illumination source with nearly precise uniformity. Pulsed lasers are also common enough that they have become user friendly and diverse enough to complete their job for countless experimental set ups. The laser most often used for PIV is the frequency doubled neodymium yittrium aluminum garnett (Nd:YAG) laser. It offers a high energy light beam, short pulse duration (<10 ns), and short 532 nm wavelength emission (Adrian, Gharib, Merzkirch, Rockwell, & Whitelaw, 1998).

The high energy light provided by a pulsed laser is important because in order to capture an image of the flow field, the beam of light must be spread into a sheet for planar illumination. As the light scatters in the sheet, the intensity of the light suffers. It is therefore important to have a light sheet wide enough to illuminate the area of interest for PIV yet small enough to have sufficient light intensity. Besides the width of the light sheet, it is also important to focus the light sheet in order to not sacrifice its intensity with its thickness. However, too thin of a light sheet will increase the likelihood of particles moving out of the plane of the laser sheet. Particle drop out, or signal drop out, is caused by any out of plane velocities experienced in the flow. A slightly thicker light sheet allows for a more forgiving threshold for any minor out of plane movement and, therefore, less signal drop out in the flow field PIV solution.

Light sheets can be manipulated using spherical lenses and cylindrical lenses in order to create the desired size, shape, and thickness. The required size and thickness is dependent upon the experiment performed. Large flow fields require larger light sheets, but size comes at the cost of reduced light intensity. The larger thickness also reduces the light intensity, although not as severely as light sheet size does. The required thickness

of a light sheet for an experiment depends upon the required threshold for capturing particles experiencing out of plane velocities For example, there is less required light sheet thickness for experiments with negligible out of plane affects compared to the additional light sheet thickness required for stereo PIV, which captures out of plane motions.

2.3.2. *Image Capturing Device*

The requirements of an image capturing device for PIV are similar to those of the PIV illumination source previously discussed. However, the purpose of the PIV image capturing device is to capture a pair of images in rapid succession, repeatedly, for the duration of a test.

Technological advances in computer and electronic imaging have provided researchers with immediate feedback on the image quality of the PIV data recorded. There are a variety of electronic image sensors available. The most commonly used is the charge coupled device (CCD) of a digital camera. A CCD is an electronic sensor that converts light into an electric charge (electrons). When referring to a CCD it is important to understand that the reference is to an array of many individual CCD's. Each CCD is typically on the order to 10 x 10 μm and represents a single pixel in the captured image (Adrian, Gharib, Merzkirch, Rockwell, & Whitelaw, 1998). The more electrons captured by CCD sensors, the more white the pixel appears. Image blooming is the result of the number of electrons exceeding that allowed by a single CCD, therefore migrating over to a neighboring CCD. The consequences of image blooming are seen in the results of the

PIV solution. The particle being cross-correlated will appear larger than its actual size in one or both of the acquired PIV images and possibly obscure the signals of the surrounding particles.

Since each individual CCD represents one pixel in the image and not a unit of length, a conversion of pixels to distance is required. This pixel per distance conversion is often referred to as pixel resolution and is defined by Equation 16.

$$Pixel\ Resolution = \frac{pixels}{d} \qquad (16)$$

where

$$d = \text{distance (m)}$$

The required distance for the pixel resolution is found by taking an image of a linear measuring device at the location which the camera is focused on the light sheet. The pixel resolution is then used in the PIV computations in order to convert the observed distances from pixels to meters. Pixel resolution should be sought considering both the tracer particle size and the flow field area of interest being researched. Individual pixels are incapable of sub-pixel deciphering, so ideally each tracer particle will be the summation of multiple pixels in order to have clearly defined shape.

2.4.   CFD Overview

Computational fluid dynamics, or CFD, has grown into a popular and dependable tool used to analyzed aerodynamic phenomena in modern day. There are several major benefits to CFD when compared to the experimental method, including cost and facility requirements to name a few. Experiments are used to validate CFD results. However, CFD also offers researchers the opportunity for mutual validation, the ability to examine possible flaws in the experimental setup and procedure (i.e. blockage in tunnel test section, interference of the model support structure, flow quality).

There was a separate 2-D time accurate CFD effort completed for mutual validation of the results attained experimentally in this research. The separate CFD effort benchmarked two different CFD approaches: a common Reynolds averaged Navier-Stokes code (RANS) and an extension of the immersed boundary method (IB). For both methods the usual issues of turbulence model, capture of transition in boundary layers and shear layers, wall effects, and grid/temporal resolution were considered (McGowan, Gopalarathnam, Ol, Edwards, & Fredberg, 2008).

The commonly used RANS code used in the separate but coordinated study is called CFL3D was developed and used at NASA Langley Research Center. CFL3D solves the Thin-Layer Navier Stokes equations and is written in a structured framework capable of calculating solutions on one-to-one, patched, or overset grids. The CFD grid is created around the test specimen geometry, an airfoil in this case. Grids are adapted to the airfoil geometry and nodes in the grid coincide with the boundary of the airfoil. The nodes are spaced closer to one another near the airfoil surface to refine the accuracy of

the boundary layer solution. The entire grid moves to simulate the fluid motion surrounding the airfoil (McGowan, Gopalarathnam, Ol, Edwards, & Fredberg, 2008).

The immersed boundary method resolves flow features by inserting a given geometry, an airfoil in this case, into a pre-existing computational mesh. This method avoids the complexity associated with grid adaptation, overset grids, and/or moving grids. Boundary points of the airfoil do not need to align with grid nodes. Instead, the effects of the immersed boundary are included by defining band cells, grid cells through which the airfoil boundary overlie, and prescribing conditions on these cells. The immersed boundary code then solves the incompressible Navier-Stokes equation utilizing the finite volume method (McGowan, Gopalarathnam, Ol, Edwards, & Fredberg, 2008).

3. Methodology

3.1. Experimental Apparatus and Setup

3.1.1. Water Tunnel System

All experiments were performed at the Air Force Research Laboratory Air Vehicles Directorate (AFRL/RB) Horizontal Free-Surface Water Tunnel (HFWT), Wright Patterson Air Force Base (WPAFB). The test section is 0.46 m x 0.61 m x 2.74 m. The contraction ratio is 4:1, with two honeycomb screens and three wire-mesh screens used to create a uniform flow over the cross section of the test section. A 12 in. axial impeller, driven by a 15 hp motor, gives a flow velocity range of approximately 3.8 to 45 cm/s. Single-component hot-film measurements report a stream wise turbulence intensity of approximately 0.1% (Kaplan, Altman, & Ol, 2007). The velocity of the flow in the HFWT was controlled using a pump drive digital control unit, measuring in units of Hertz (Hz). A picture of the AFRL/RB water tunnel at WPAFB, OH, is shown in Figure 6, and additional details are given in previous research by Ol (2007, 2008).
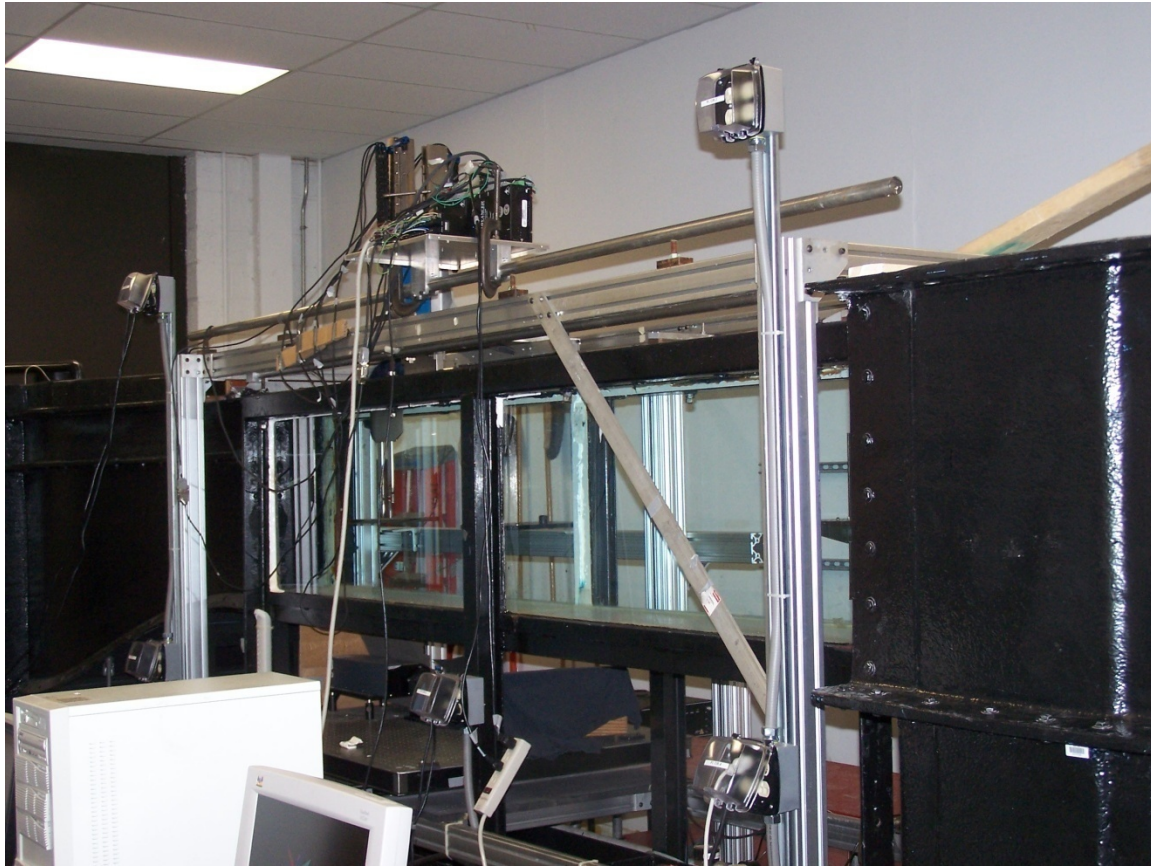
Figure 6: AFRL's Horizontal Free-surface Water Tunnel (HFWT) with motion rig on top.

The flow medium of the tunnel consists of water at room temperature, approximately 70 ºF. The power and flow speed of the HFWT is managed by a digital control box. The control box runs the pump of the tunnel in units of frequency (Hz).

In order to determine the effects of Reynolds number, if any, on the results for the experiments, the tunnel was run at different speeds. Table 1 shows the water tunnel frequency, flow speed, and Reynolds number achieved with the 152.4 mm chord airfoil for the research conducted.

Table 1: Tunnel pump variable frequency drive and equivalent Reynolds number.

	Water Tunnel Pump Drive	Equivalent Free-stream Velocity (U_∞)	Reynolds number (Re_c)
Pure-Plunge	8.68 Hz	6.6 cm/s	10,000
	34.9 Hz	26.5 cm/s	40,000
Pure-Pitch	8.68 Hz	6.6 cm/s	10,000
	34.9 Hz	26.5 cm/s	40,000

The SD7003 airfoil was used for all experiments conducted in the HFWT. Consequently, with matching tunnel speeds, equivalent Reynolds numbers [Equation (12)] were achieved for a comparison of each case (i.e. pure-plunge and pure-pitch).

3.1.2. *High-Intensity Pitch/Plunge Oscillator Rig (HIPPO)*

The high-intensity pitch/plunge oscillator rig (HIPPO) allows for the experimenter to uniquely design the motion of an airfoil at various pitch and plunge frequencies and amplitudes. HIPPO consists of two H2W A-40-series linear servomotors (H2W Technologies, Inc., 2007) mounted vertically on top of a plate on rails above the water tunnel's free surface, shown in Figure 7.
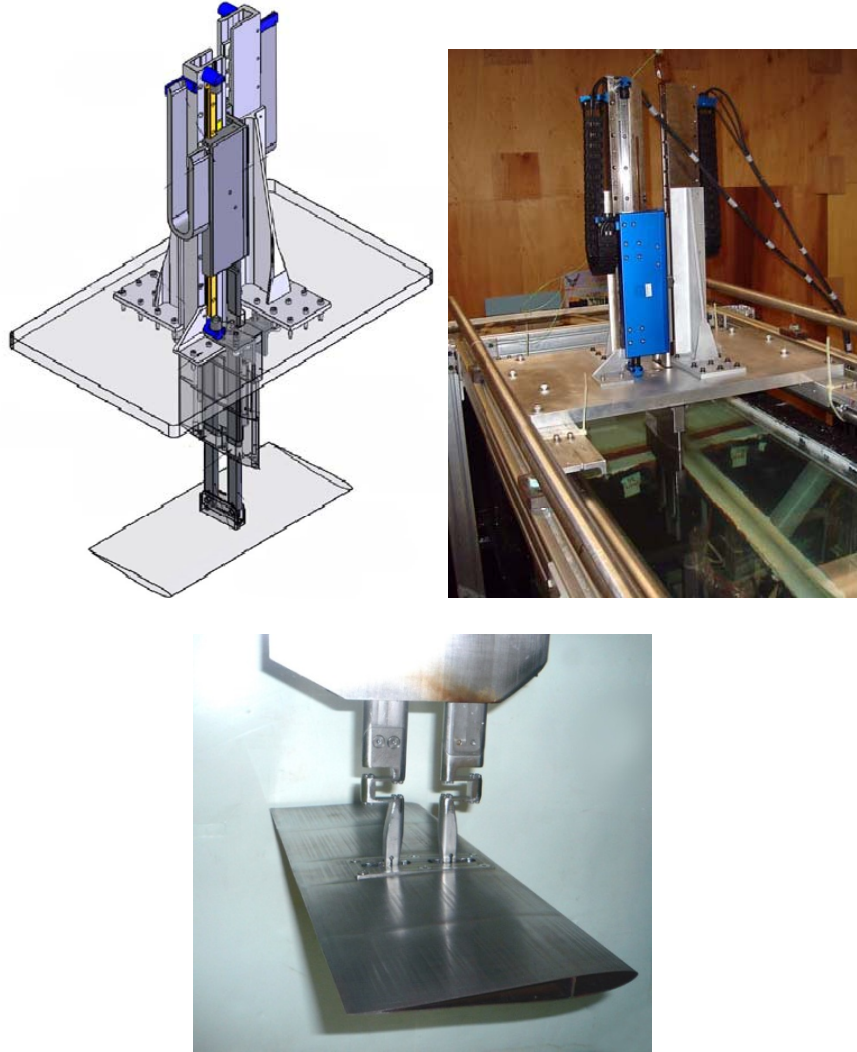
Figure 7: HIPPO: (a) schematic, (b) seen from above tunnel, and (c) image of rods attached to SD7003 airfoil in the water tunnel.

Important to note is that since HIPPO is located above the free surface of the water tunnel and the light sheet is projected through the bottom of the tunnel, the airfoil is upside down in order to capture the flow field of the low pressure side of the airfoil. The low pressure side of the airfoil, traditionally the upper surface of an airfoil, is pointing down in the water tunnel. However, this flip is accounted for in all the motion software to be

discussed, and in the results the airfoil appears in the traditional configuration, low pressure side upward.

Each motor actuates a vertically oriented rod, which connects to the SD7003 airfoil (Selig, 2006) at a fixed pivot point on the airfoil chord, shown in Figure 7. Free surface effects are largely unavoidable with this setup, but acceptable since the data is taken in planar slices well away from the centerline of the airfoil. The motion of each rod is programmed independently, which allows for single degree-of-freedom motions such as sinusoidal pure-pitch or pure-plunge, as well as nonlinear and combined motions. The precision of the motions are to within approximately 300 counts, where 5000 position counts is representative of 1 mm. The pivot point for pitching motions can be altered as well, but for the purposes presented in this paper, the pivot for all pitching motions is located at the quarter-chord.

The motions for the experiment were created using the spreadsheet, "data_generation.xls" shown in Appendix A, and are run using software specifically designed for HIPPO, namely DMC Smart Terminal. Motions are created based on the point of rotation along the chord (i.e. quarter-chord in this case), physical frequency, f, and amplitude, h or θ. For the plunge case, amplitude refers to the vertical motion of the airfoil in units of chord. The pure-plunge motion of the airfoil creates a motion-induced angle of attack which will be matched for the pure-pitch case with the geometric angle of attack. The amplitude for the pitch case is then the geometric angle of attack bounded by the motion-induced angle of attack of the plunge case. Table 2 shows the physical frequency, amplitude, and reduced frequency of the experiments conducted for this research.

31

Table 2: Parameters of the plunge cases and pitch cases performed.

Test Case	Physical Frequency, (f)	Amplitude	Reduced Frequency, (k)	Strouhal Number, (St $_{T.E.}$)
Plunge, $Re_c=10\times10^3$	0.53 Hz	±0.05 chord	3.93	0.12
Plunge, $Re_c=40\times10^3$	2.13 Hz	±0.05 chord	3.93	0.12
Pitch, $Re_c=10\times10^3$	0.53 Hz	21.5˚	3.93	0.69
Pitch, $Re_c=40\times10^3$	2.13 Hz	21.5˚	3.93	0.69

The created motions and respective angles of attack for the plunge case and the pitch case

are plotted in Figure 8 and Figure 9.
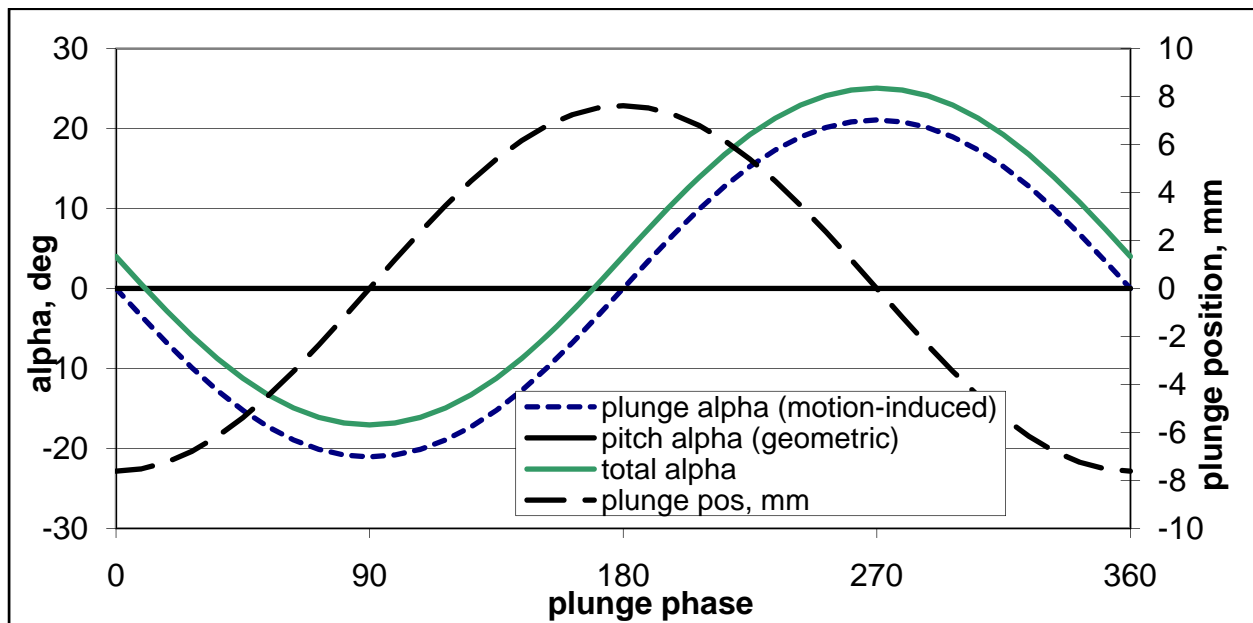
Figure 8: Pure-plunge case motion and alpha plot over one phase at quarter-chord.
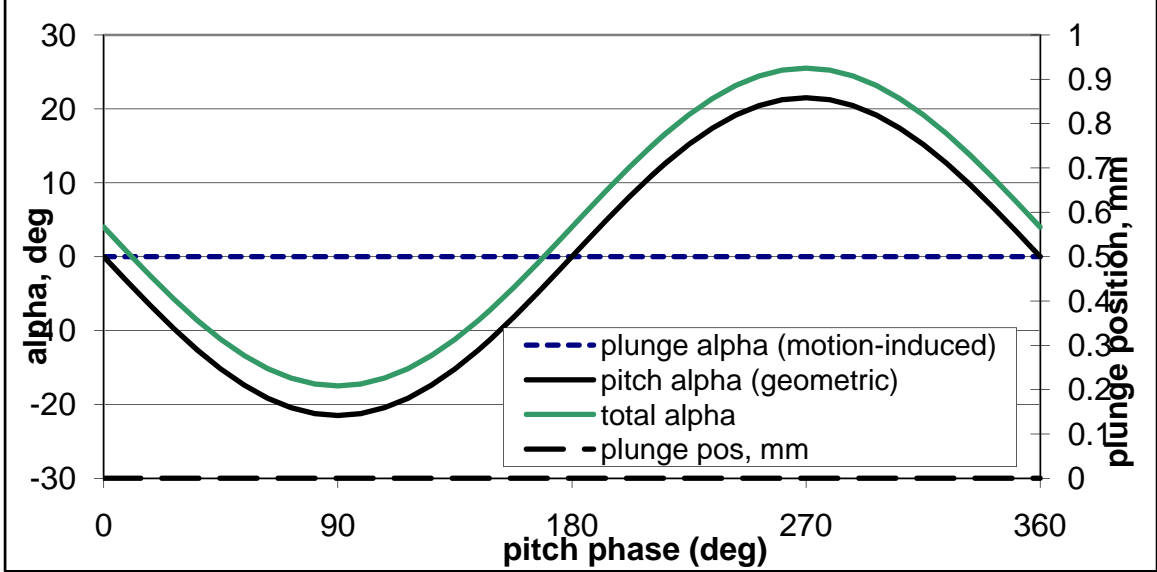
Figure 9: Pure-pitch case motion and alpha plot over one phase at quarter-chord.

The total angle of attack, shown in Figure 8 and Figure 9, includes the initial 4˚ offset as mentioned in *Section 2.1*.

The flow over a flapping wing is constantly changing during the pitch or plunge. It is therefore important, in an investigation such as this one, to designate what part of the phase PIV data should be collected. One complete phase refers to the completion of one oscillation of the airfoil, either plunge or pitch. For example, one phase of the pure-plunge case and pure-pitch case were shown in Figure 8 and Figure 9. Points along the phase are chosen to trigger the light source and camera for PIV acquisition. For the purposes of examining an oscillating airfoil, phase 0˚, 90˚, 180˚, and 270˚ (i.e. 0, 0.25, 0.5, and 0.75 of the full period, respectively) were chosen since they represent the top of the plunge/pitch, the midpoint in the down plunge/pitch, the bottom of the plunge, or pitch, and the midpoint in the up plunge, or pitch, of the airfoil. At these phases PIV

results will be phase-averaged in order to give an averaged representation of the flow field.

A graphical comparison of the pure-plunge motion and the pure-pitch motion examining the trailing edge position is shown in Figure 10. The y-axis is defined as the direction perpendicular to the free stream and the x-axis is defined as direction parallel to the free stream flow. Note that the y-position of the trailing edge is considerably larger for pitch than for plunge.

Trailing edge position during one phase

| plunge y-position |
| plunge x-position |
| pitch y-position |
| pitch x-position |
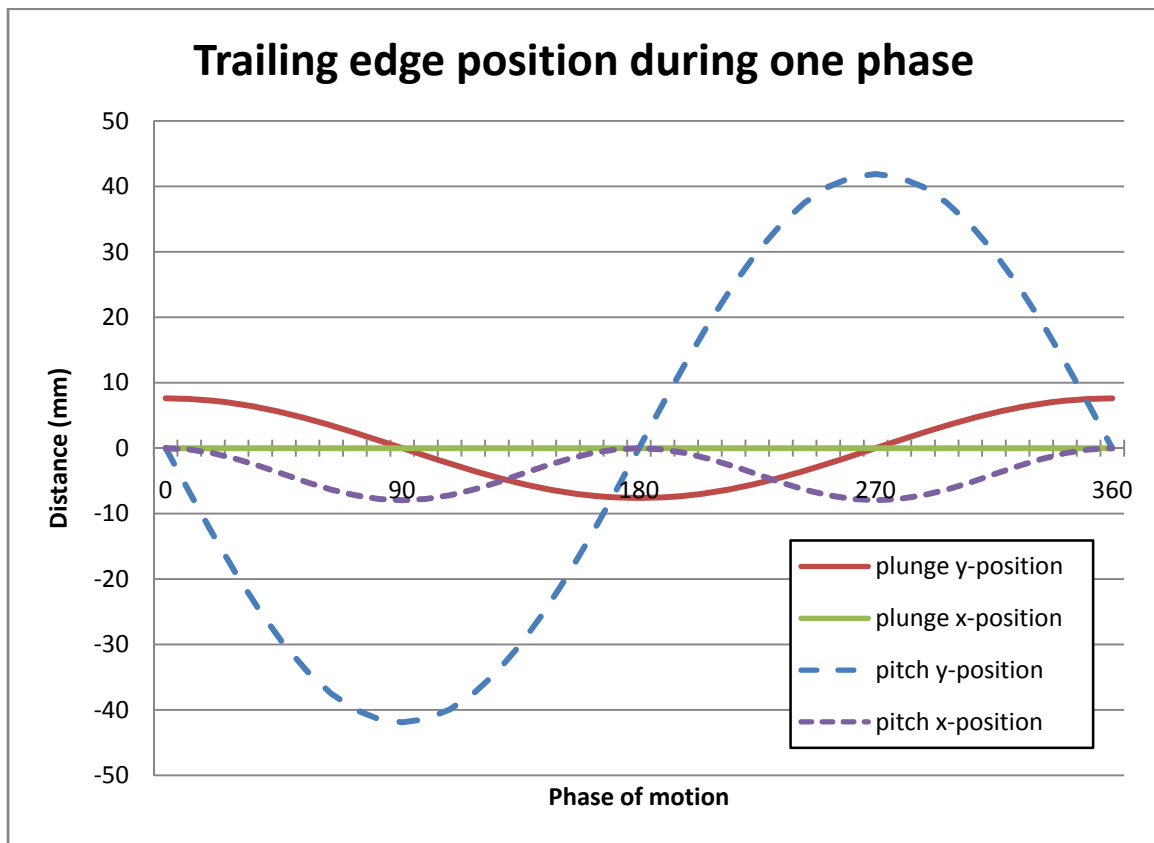
Figure 10: Trailing edge position comparison of pure-plunge case and pure-pitch case.

A comparison of the velocities of the trailing edge in the y-direction, v, and in the x-direction, u, are shown in Figure 11 and Figure 12 respectively. Note the trailing edge velocities of the pure-pitch case are considerably greater than that of the pure-plunge case.
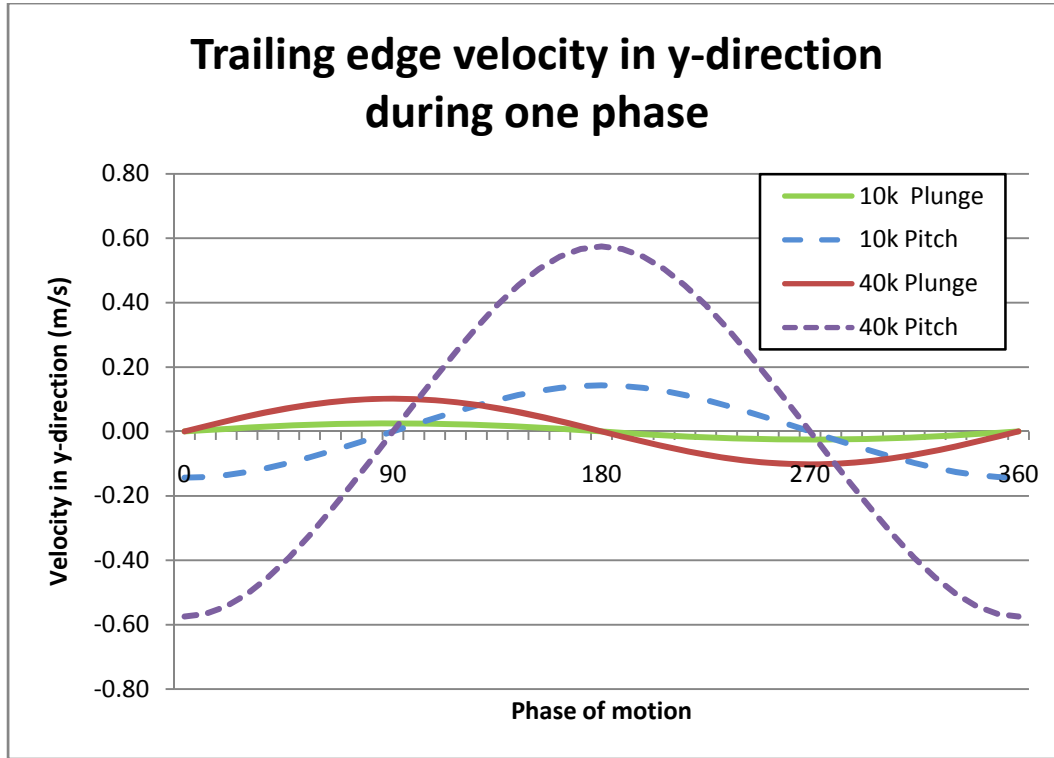
Figure 11: Trailing edge y-velocity comparison of pure-plunge case and pure-pitch case.
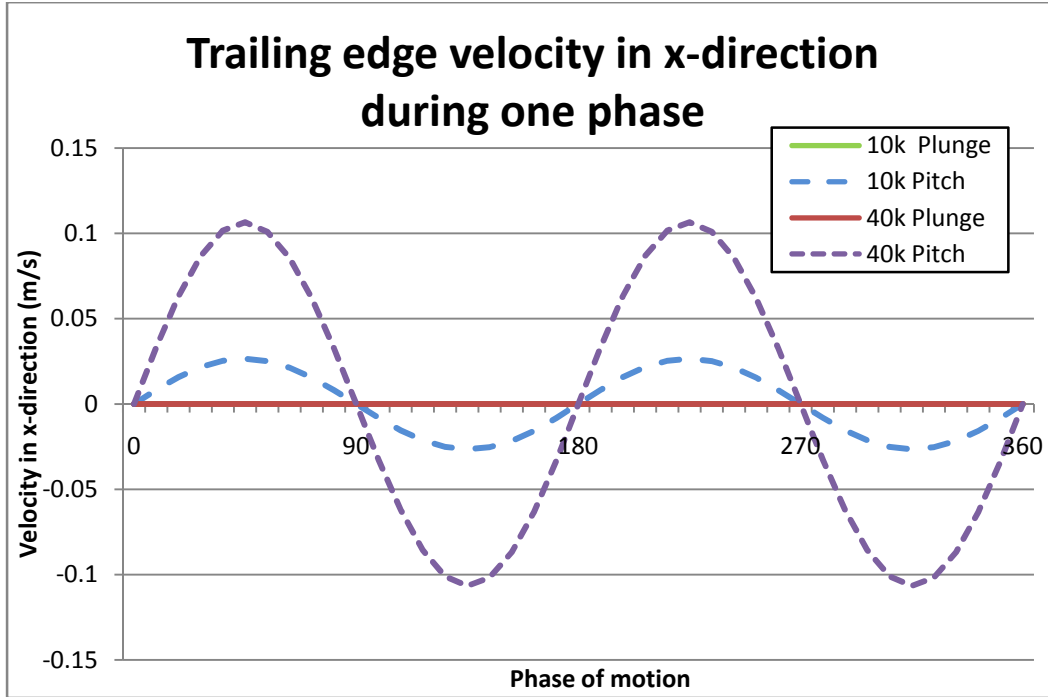
Figure 12: Trailing edge position comparison of pure-plunge case and pure-pitch case.

Although the reduced rate and effective angle attack have been matched at the quarter-chord, the motion at the trailing edge of the airfoil varies greatly. The velocities in the y-direction of the trailing edge for the pure-pitch case are much greater than those of the pure-plunge case. Unlike the pure-pitch motions, the pure-plunge motions experiences no velocities in the free stream direction, or x-direction. One would assume that these differences could contribute to dissimilarities in the PIV results of flow field.

3.1.3. PIV System

The PIV system used for the research discussed in this report consisted of a triggering device, image capturing device, illumination device, and a PIV processing computer. The camera and laser were both triggered off a pulse derived from the motion software (DMC Smart Terminal), where any single position in the phase of the motion can be selected as the trigger to acquire data. A schematic of the PIV system used is shown in Figure 13.
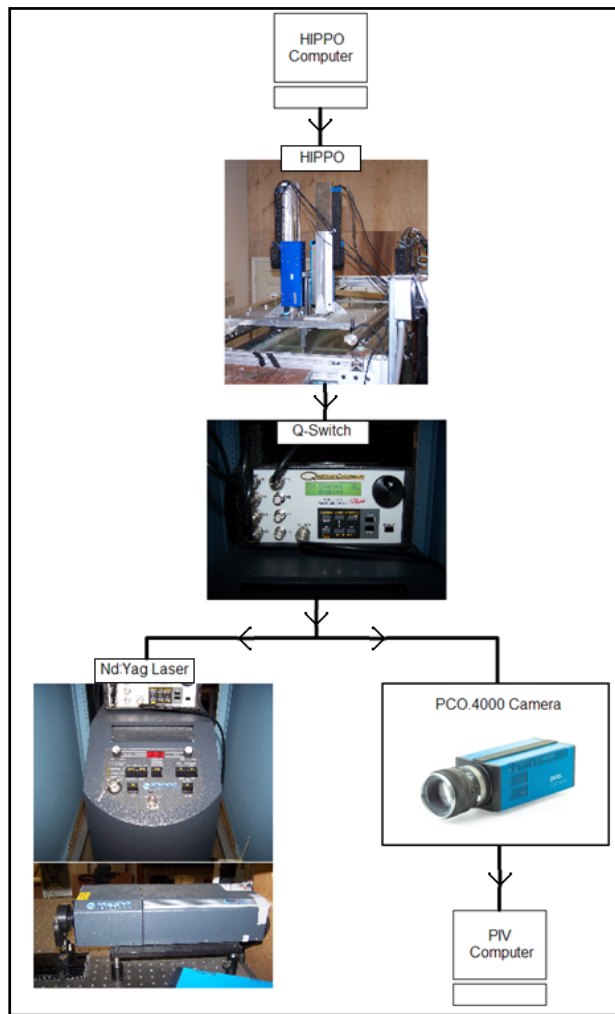
Figure 13: Schematic of water tunnel, motion rig, laser, and PIV system connections.

After the motion is created with a trigger point, it is downloaded to the motion rig (HIPPO). The motion commences, and at specific points in the phase a pulse is sent to the Q-Switch (Quantum Composers Pulse Generator Plus, model 9618). The Q-switch is also where the time separation between laser pulses (Δt) is set for the laser and camera. This is set based upon the velocities observed in the flow field of a specific case and the optimal distance for a tracer particle to travel for a good PIV cross-correlation.

The pulse laser used for this experiment was the New Wave Research Solo PIV, double pulsed (nominally 125mJ/pulse), 15 pulse/s Nd:YAG Laser. The laser is located beneath the water tunnel test sections and the light sheet is created and reflected using two spherical lenses (CKV075 with a negative focal point and CKX025) and a cylindrical lens for focusing (all manufactured by Newport Corp.), shown in Figure 14. Lenses and mirrors were positioned using Melles Griot mounts.
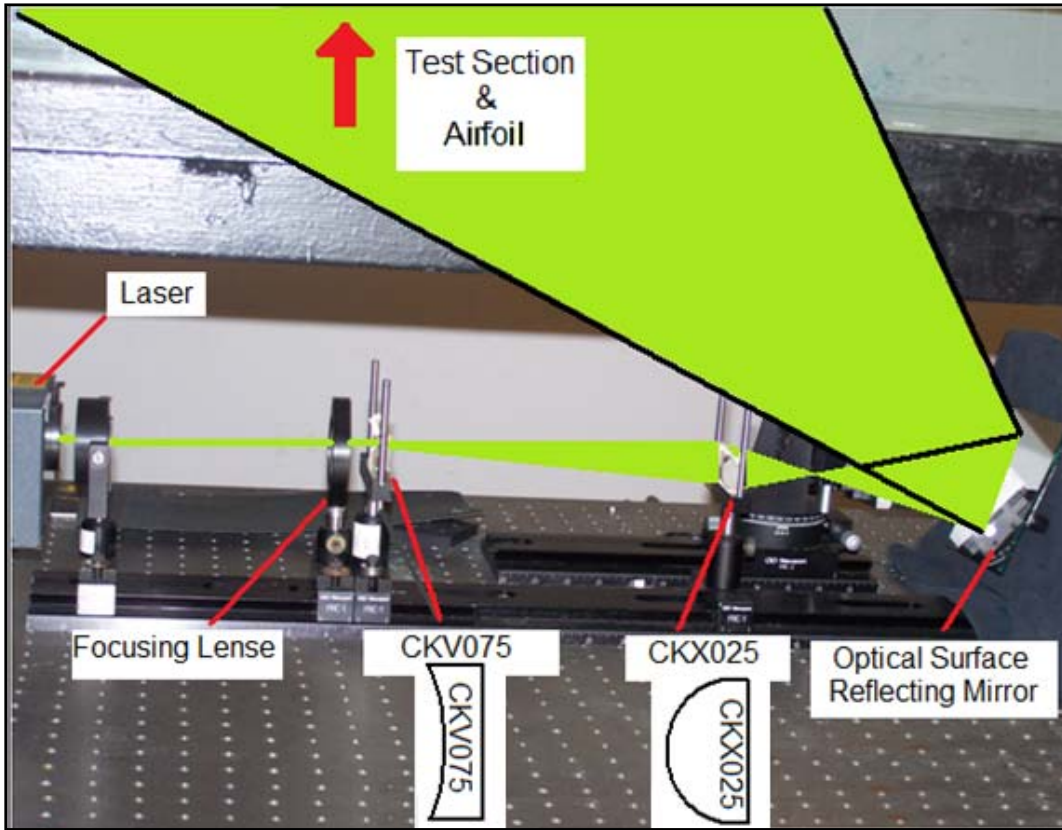
Figure 14: Laser sheet, lenses, and mirror.

The Laser sheet created was approximately 2 mm thick and 45 cm wide at the midpoint of the flow field of interest. Lens configuration was based on ideas detailed by Adrian et al. (1998). Due to its large size and thickness, collimation of the light sheet was difficult. During PIV tests the laser was set to 90-99% full energy to account for the large light sheet required for capturing the flow field around the airfoil and its wake. It is important to note that the light sheet illuminates only one side of the airfoil in this configuration. The upper, pressure side of the airfoil is in shadow and therefore is not beneficial to the comparisons intended for this research.

Titanium Dioxide (TiO_2) was used as the PIV seed material. TiO_2 is insoluble in water, has a specific gravity of 4 (water = 1), a diameter of <1 μm, and is relatively inexpensive when compared to other, more exotic seeding particles (OSHA 2007). Due to the small particle size, the settling velocity of TiO_2 is considerably lower than the velocity of the water in the tunnel. For the tunnel velocities and duration of this experiment, the inertial effects of TiO_2 tracer particles, being denser than the water, can be neglected. Furthermore, TiO_2 is rather resistant to clumping and has high reflectivity, providing bright and even illumination without blooming the camera's CCD pixels (as would a large particle or debris). With recurrent observation and experimentation, it is also concluded that TiO_2 does not stick to test specimen in the water tunnel.

It is important to handle TiO_2 properly for the safety of the user. TiO_2 particles, due to their small size, can easily be inhaled if airborne. It is therefore recommended to wear a mask (i.e. painters mask) to cover both the nose and mouth of those handling the TiO_2 prior to it seeding the water flow. If TiO_2 collects on skin wash with soap and water, and if inhaled, one should seek medical attention immediately if any respiratory symptoms should occur.

A PCO 4000 11 Megapixel camera with 105 mm Nikon lens was used at *f*-stop 8 to capture instantaneous images of the TiO_2 particles in the flow field illuminated by the laser sheet. The focal length was approximately 2 m. Since the airfoil was in motion during and the camera was stationary in all the experimental runs, parallax was an issue. The border of the airfoil closest to the camera would overlap the boundary layer of the plane of interest close to the airfoil surface. Figure 15 shows an example of parallax on a plunging airfoil viewed straight on.
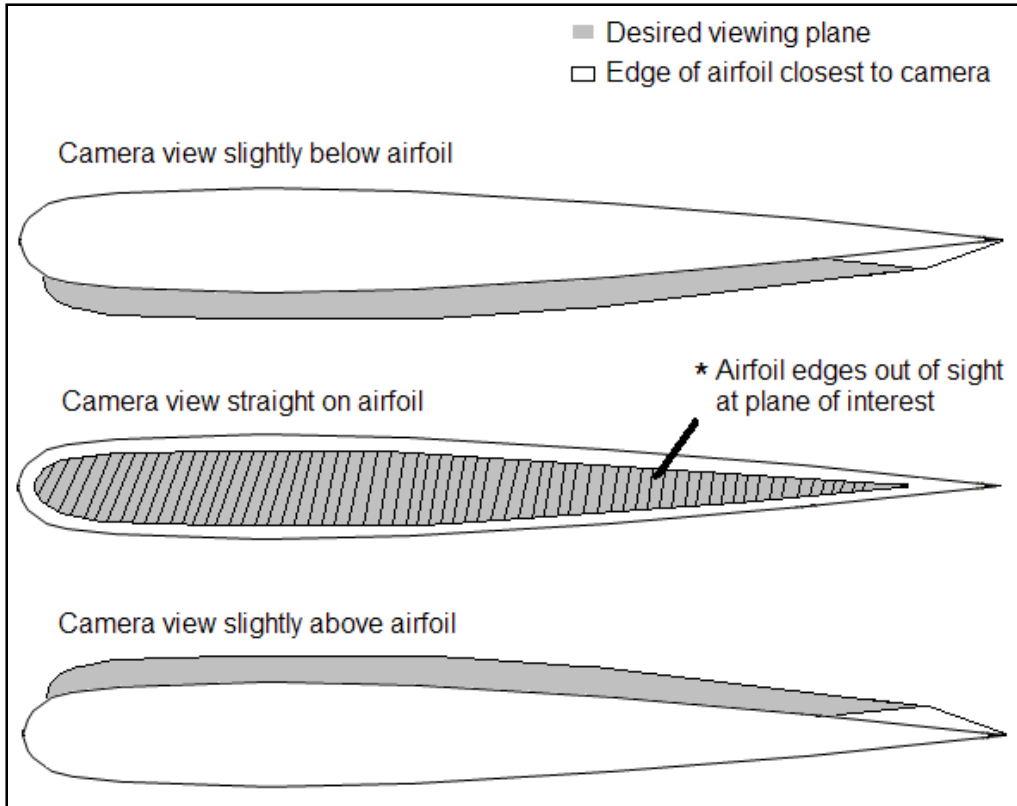
Figure 15: Parallax example for plunging airfoil.

The parallax issue contributed to a loss of reliable boundary layer results approximately 0.02c off the airfoil surface. Although undesirable, this did not hinder the overarching purpose of this research, comparing entire flow fields of oscillating airfoils.

The camera shutter opens when it receives the triggering pulse from the Q-Switch corresponding to the laser firing. The camera collects images corresponding to two succinct pulses, separated by Δt. The captured images are recorded using PCO Camware v2.15 software. Camware also allows the user to easily change the exposure time of each image pair prior to collecting the entire data set. Instantly viewing the captured images using Camware allows the opportunity to stop, adjust, and restart the test, saving additional time spent collecting and processing image data of poor quality. Overexposing

or underexposing either of the two images captured could result in poor cross-correlations in the PIV processing. The exposure time was easily adjusted for each test since it varied slightly on a case by case basis, since tracer particle density in the flow field was never constant. With laser energy constant, the higher the particle density, the brighter the illumination for image capturing and less exposure time required. The captured images from the camera are then displayed and transferred to the PIV computer for processing.

Velocity data (i.e. PIV images) were acquired at the four individual predetermined phases in the period (i.e. 0°, 90°, 180°, 270). So, for each case (pure-plunge $Re_c = 10x10^3$, pure-plunge $Re_c = 40x10^3$, pure-pitch $Re_c = 10x10^3$, and pure-pitch $Re_c = 40x10^3$) there were four image data sets. Image data sets were limited to 120 images because of the allotted camera memory. Phase-averaged results for each phase were based upon 115 image pair solutions. The first five image pairs of each velocity data set were ignored to account for startup transients that could otherwise erroneously affect the results of the PIV experiment. Therefore, the phase-averaged PIV solution, was based on 460 image pairs, or 115 image pairs for each of the four phases in each experiment.

PIV processing was accomplished using programs developed in previous research by David Jeon (2000), described in more detail in Appendix B. The programs software is DOS, LINUX, and UNIX based and written in Practical Extraction and Report Language (PERL) script. The main processing software, DPIV, performs the cross-correlation in the subregions (size set by user) of an image pair. The solution can then be examined for outliers, or inaccurate cross-correlation solutions, by setting a threshold when comparing neighboring vectors to each other. For each stage of the PIV processing program,

individual image pair solutions can be viewed to check for solution quality. Finally, the average of all the solution data of each image pair is combined into one final solution that is then converted, using utility software, to a format suitable for Tecplot (Tecplot 360 , 2006). Tecplot is then used to create contour plots, vector plots, and perform further analysis on the flow field of interest for this research.

3.1.4. Additional Experimental Cases

During the course of this research additional airfoil oscillating motions were programmed into the HIPPO and tested on the SD7003 airfoil using PIV. However, the motions do not directly contribute to the comparison between pure-plunge and pure-pitch. Many of the supplementary tests were for separate research efforts in need of experimental results and validation detailed in this report. PIV results of these additional tests are shown in Appendix C. A brief overview of the parameters used for the additional PIV experiments are shown in Table 3.

Table 3: Parameters of additional PIV experiments completed on oscillating airfoils.

Pure-plunge oscillating airfoil wake PIV	$k = 3.93$, $Re_c = 60\times10^3$, $h = 0.05$, $\alpha_o = 4°$, pivot = 0.25c
Low frequency pure-plunge oscillating airfoil	$k = 0.25$, $Re_c = 60\times10^3$, $h = 0.05$, $\alpha_o = 8°$, pivot = 0.25c
Low frequency pitch leading plunge oscillating airfoil	φ (pitch offset) = 90°, $k = 0.25$, $Re_c = 60\times10^3$, $h = 0.05$, $\alpha_o = 8°$, $\theta_o = 8.42$, pivot = 0.25c
Mixed plunge and pitch	φ (pitch offset) = 90°, $k = 8$, $Re_c = 10\times10^3$, $h = 0.1$, $f_{plunge} = 1.10281$, $f_{pitch} = 2.20561$, $\alpha_o = 4°$, $\theta_o = 15°$, pivot = 0.5c

The pure-plunge oscillating airfoil wake PIV test produced results for the wake to complement previous PIV boundary layer work on the same case (Ol, 2007). The boundary layer results and wake results tested separately were successfully combined and showed good correlation.

The low frequency pure-plunge oscillating airfoil and pitch leading plunge oscillating airfoil experiments were conducted for Lian, Ol, and Shyy (2008). The purpose of this experiment was to examine the flow characteristics on a pitching-plunging airfoil and compare them to results attained computationally. Results were ultimately motivated by kinematics for maximum propulsive efficiency. Reasonable qualitative agreement was found between experiment and computations.

The mixed plunge and pitch experiment was conducted for Webb et al (2008) who examined the vortex shedding of an oscillating airfoil where the frequencies of the plunge and pitch are not equal. The motivation was to consider flows with very large

excursions in total angle of attack, for assessment of motion time history effects. Furthermore, the experiment was completed in order to validate results achieved computationally for flow field with massive unsteadiness. Results showed that the observable flow field structures between particle image velocimetry at $Re_c = 10x10^3$ compared to an immersed boundary computation were quite good for two plunge periods after motion startup, but degraded thereafter.

3.2.   Experimental Procedure

3.2.1. PIV Data Collection

The same procedure was followed for each experimental case examined. The procedure can be broken into five required actions: (1) running the water tunnel, (2) seeding the flow, (3) activate components required for image capturing, (4) starting HIPPO, (5) focusing camera, and (6) capturing data for PIV processing. At the start of each test, initial PIV image pairs were examined in order to validate the experimental setup. This was done in order to minimize time spent analyzing inaccurate results of a complete image acquisition.

Running the water tunnel involved cleaning the test section, turning on the tunnel power supply, activating the tunnel pump digital control box, and setting the tunnel flow rate accordingly. The water tunnel test section and the airfoil were cleaned regularly to remove sunken debris and TiO_2 particles that settled while the flow was stagnant. Failure to do so could have resulted in significant shadowing of the light sheet, which travels through the transparent bottom of tunnel test section, and/or excess illumination of the airfoil surface. In the case of an emergency, the tunnel power supply can be used as a shut off switch. However, in regular use, the tunnel should be turned off initially with the digital control box to the pump. Using the control box, the frequency of the motor driving the pump was set to achieve the desired flow speed. Procedure requires waiting ample time in order for the water to accelerate to the desired speed.

Seeding the water tunnel required the safe handling of TiO_2. A painter's mask was worn at all times when handling TiO_2 in its powder state. To seed the water tunnel, a

bucket was filled with approximately one gallon of water. Using a small scoop, one or two tablespoons of TiO_2 were inserted into the bucket of water slowly, to avoid allowing the TiO_2 to become air born. The water in the bucket was stirred and a quarter of the mixture was carefully poured into the free surface of water tunnel. After pouring, the procedure requires two to five minutes of waiting in order to allow the TiO_2 to evenly distribute in the flow. Finally, the particle density in the flow of the test section was observed and more TiO_2 particles were added to the flow if required.

The components required for image capture included starting the laser, activating the Q-Switch, turning on the camera, and initializing the PIV software. In regards to laser usage, proper protective eyewear was worn at all times while the laser was in use. After turning on the laser, the desired energy of the laser for PIV image capture was set, and the laser trigger setting was changed from internal to external, awaiting the pulse from the Q-Switch. Next, the Q-Switch was activated and the initial time increment between image captures and laser pulses, Δt, was set based on the free stream flow velocity. The Camware camera controls are shown in Figure 16.
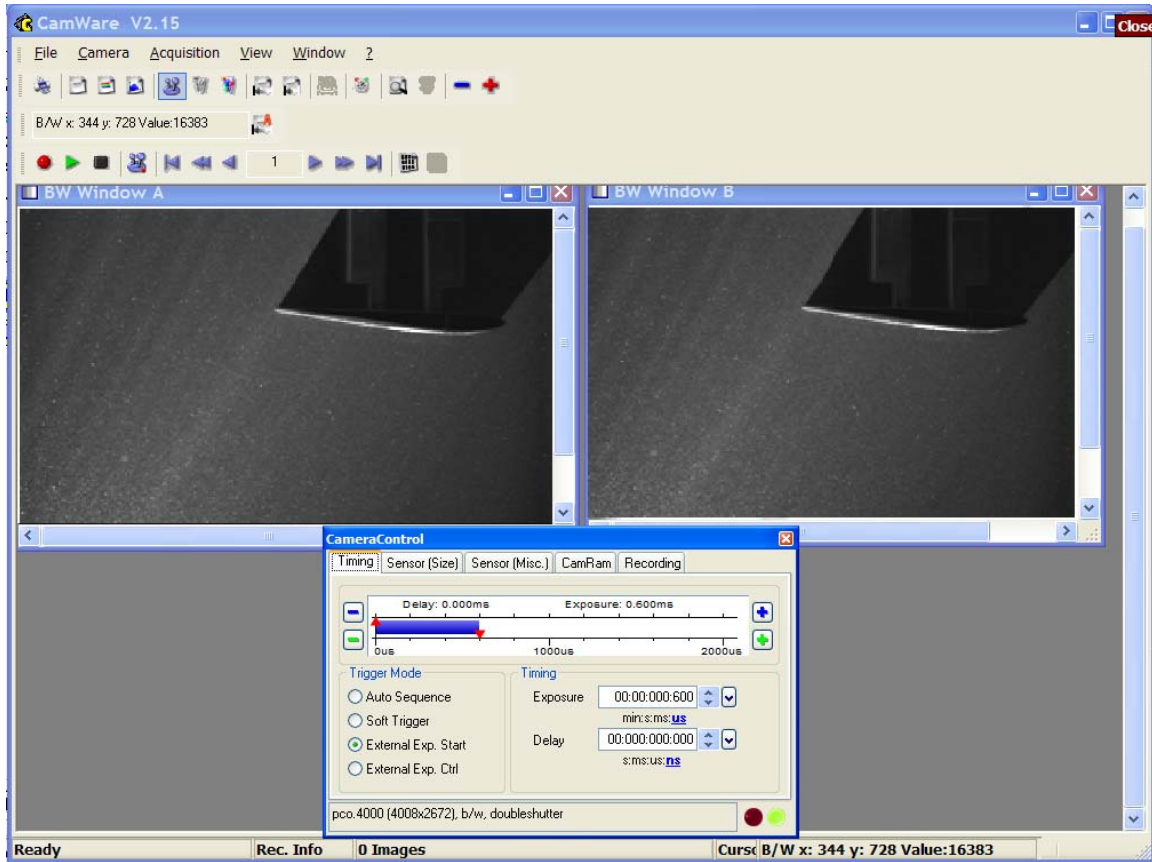
Figure 16: Camware v2.15 controls screen shot.

After turning on the camera, the Camware software was initiated on the PIV computer. The exposure time was set and the recording function was initiated. The recording function places the software in a mode ready to record images once they are sent from the camera. Recall that the camera does not begin to capture or send images to the software prior to receiving the pulse from the Q-Switch, which receives it pulse from the HIPPO.

Running HIPPO required the motion created to be uploaded to the rig software. Once uploaded, HIPPO can be activated, stopped, and shut off from the computer. The created motions contained the phase points which sent a pulse to the Q-Switch

periodically during the motion. The lights in the lab were shut off and the motions were initiated causing the pulse from the Q-Switch to trigger the laser and camera. The camera began capturing images that could be viewed simultaneously using the Camware software. As it continued to capture images, the camera was focused by viewing the images as they were recorded to the PIV computer, using Camware. The exposure time was also adjusted accordingly based on image brightness. Properly focused and illuminated images were then processed to provide a sample PIV processed solution. This allowed for immediate feedback on the PIV image quality taken before commencing the actual test, consisting of 120 image pairs for each phase. These sample results were used in order to adjust the Δt of the Q-Switch and check PIV quality.

Once the PIV quality was deemed sufficient, HIPPO was stopped, ending the pulses sent to the Q-Switch triggering the laser and camera. The Camware software was stopped and the memory allotted for images was cleared in preparation for a complete 120 PIV image pair acquisition. The record function of Camware was activated and the HIPPO motions were restarted. Images were first recorded to Camware allocated memory and were then saved to the PIV computer hard drive. The lights of the lab were turned back on and a ruler was placed in the focused plane of the camera in order to capture a calibration image. An example calibration image is shown in Figure 17.
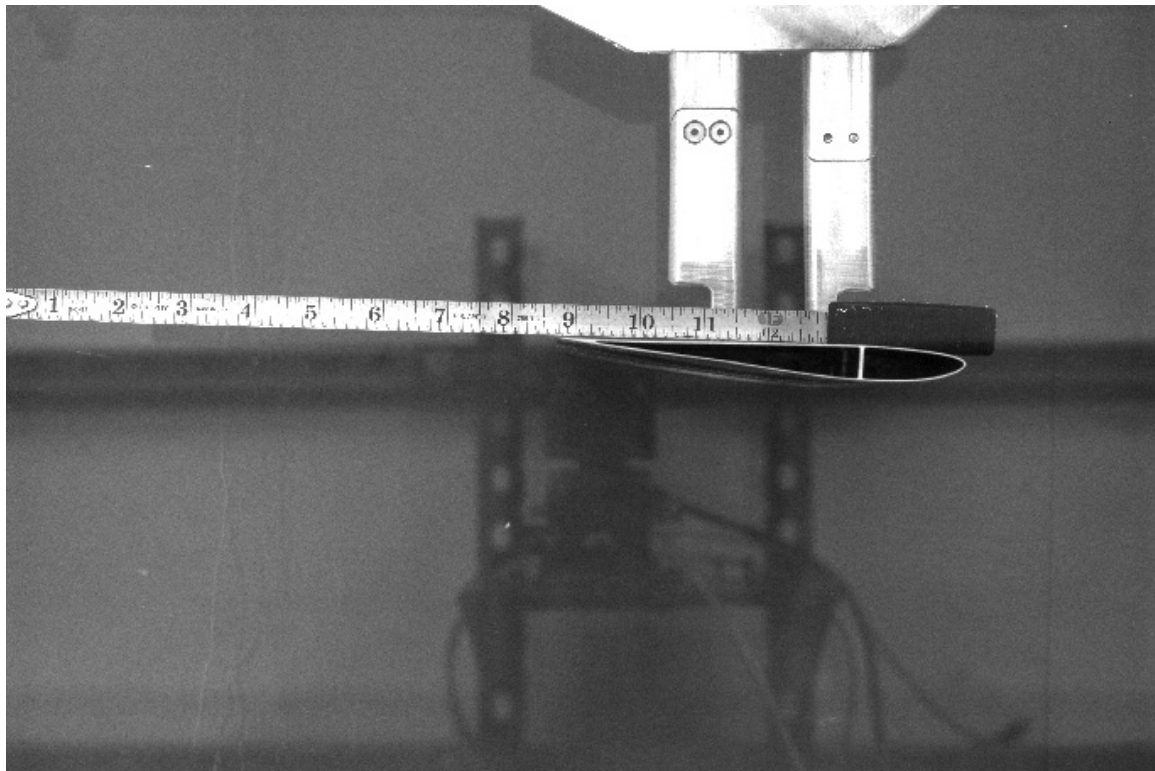
Figure 17: Calibration image captured for PIV processing.

From a calibration image, as seen in Figure 17, the pixel resolution for a test case is found and used in the PIV processing, as discussed in *Section 2.3.2*. Finally, the images gathered during the test were then converted to a raw format, as required by the PIV processing software.

3.2.2. PIV Processing

The PIV processing was accomplished with the cross-correlation technique described in *Section 2.3* using the PIV software functions developed by David Joan (2000).   The subregion's were 32 x 32 pixels and had a 50% overlap.   The pixel resolution was approximately 88 pixels/cm for the $Re_c = 10x10^3$ cases and 110 pixels/cm for the $Re_c = 40x10^3$ cases.   Pixel resolution differed by approximately 25% due to camera repositioning after the $Re_c = 10x10^3$ cases, allowing the camera to be mounted at a greater distance from the test section.   Processing required the creation of a par file, in which the interrogation region size, image size (2672 x 4008 pixels), and pixel resolution are set.

With the processing software used, one could mask out, or neglect, portions of the image map, airfoil model and shaded region, where there was no signal for PIV to be accomplished.   These regions appeared in the results as a large group of random outliers. For each test, image pairs were individually solved, meaning that a cross-correlation solution was found and the outliers were corrected using a moving average validation. Since neighboring vectors should be approximately the same size, the moving average validation is an iterative filter that ignores solutions of vectors which deviate beyond an accepted value.   The disregarded vector solution is then replaced by the average of its neighbors. Figure 18 shows an example schematic of the PIV solutions, pure-pitch $Re_c = 40x10^3$ case at this point in the processing.
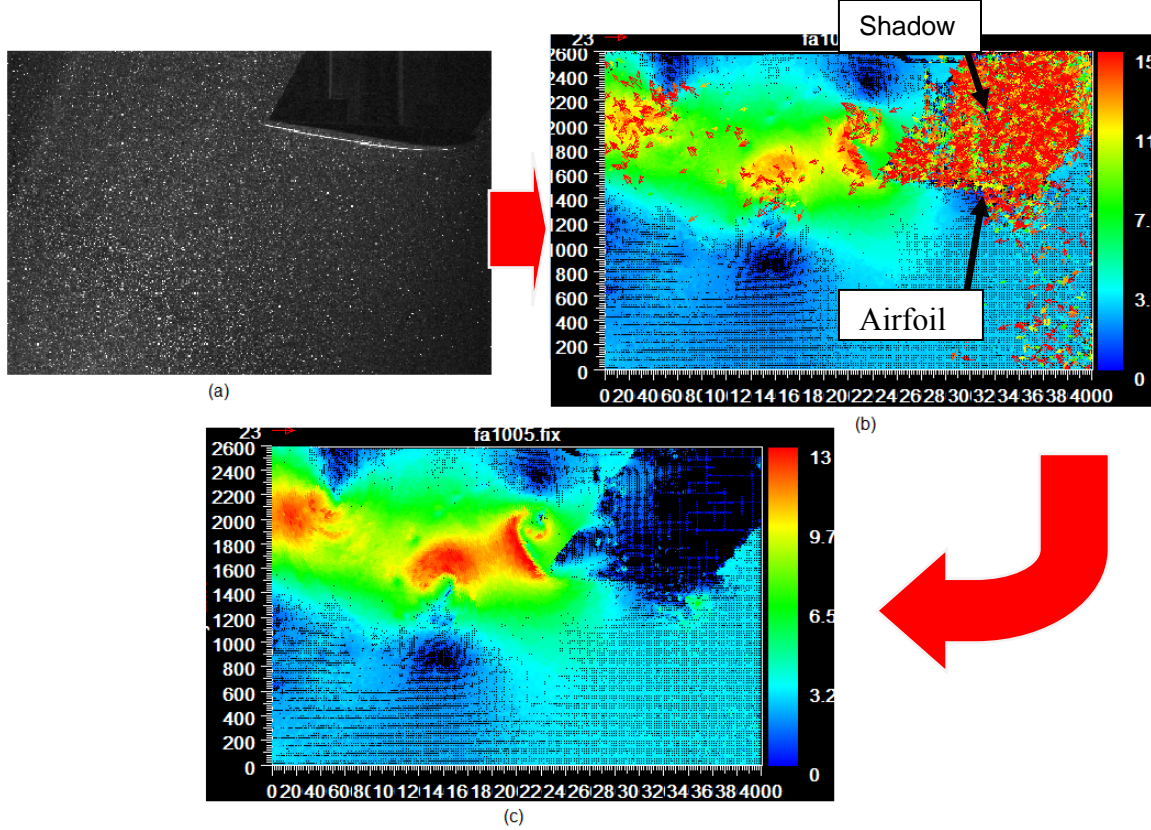
Figure 18: (a) Raw PIV image, (b) cross-correlation solution shown as contour vector plot of u (pix/cm), and (c) solution after moving average validation.

The individual image pair velocity solutions are then used to find their respective vorticity solutions. Finally, the individual image pair solutions are converted from pixels to cm, combined, phase-averaged for a better flow field representation, and saved in a format suitable for post-processing.

The processed PIV data is read into Tecplot (2006) and rescaled into units of chord. In Tecplot, the solution data (u, v, and ω_z) can be viewed using vector plots, contour plots, or a combination of both. In order to conceal the airfoil and shaded region of the processing solution, a mask was created to pictorially represent the respective

areas. Figure 19 shows an example of a plot and mask used for the pure-pitch case at phase 0º, $Re_c = 40x10^3$. As described earlier, the solution shown in Figure 19 is rotated 180º so the airfoil is in a conventional orientation.

(a)

(b)

(c)
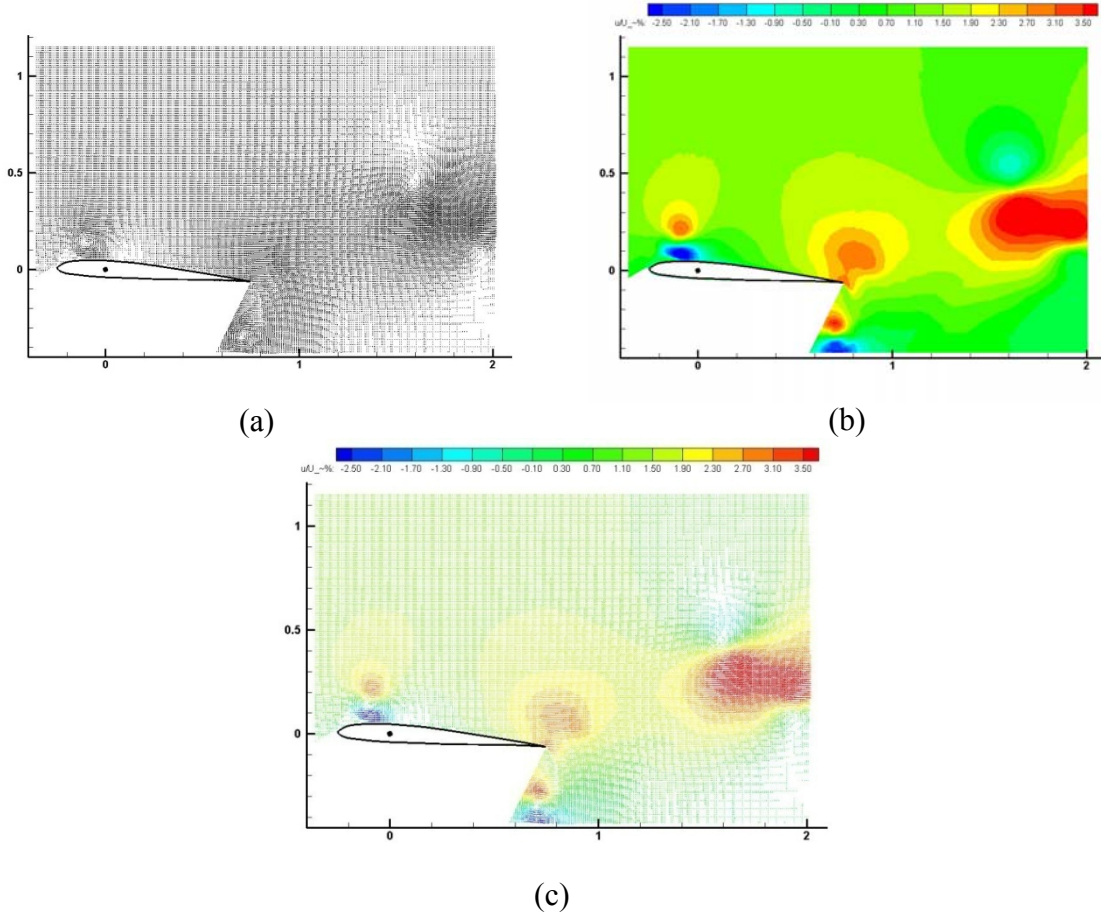
Figure 19: Shown are (a) velocity (u/U_∞) vector plot, (b) contour plot of u/U_∞, (c) combination of both taken for $Re_c = 40x10^3$ pure-pitch case, phase 0º.

4. Results and Analysis

4.1. Pure-Plunge Case

PIV was accomplished for the pure-plunge motions described in *Section 3.1.2* for $Re_c = 40x10^3$ and $Re_c = 10x10^3$. The purpose of performing the pure-plunge case for varying Reynolds numbers was to assess the assumption that Reynolds number effects are negligible in the deep stall flow fields present for these high frequency cases, at $Re_c = 10x10^3$ and $Re_c = 40x10^3$. Table 4 shows a summary of the parameters used for creating and comparing the pure-plunge cases.

Table 4: Pure-plunge experimental parameters.

	Free-stream velocity (U_∞)	Physical frequency (f)	PIV Δt	Reduced frequency (k)	Strouhal number (St_h)
Plunge (Re_c=40,000)	26.5 cm/s	2.13 Hz	1.8 ms	3.93	0.12
Plunge (Re_c=10,000)	6.6 cm/s	0.53 Hz	8 ms	3.93	0.12

Note that, like the Reynolds numbers, the free-stream velocity, physical frequency, and Δt all vary by a factor of four. This was accomplished in order for the reduced frequency to remain equivalent between both Reynolds number cases. Since the flow was four times faster for the $Re_c = 40x10^3$ case, it makes sense that Δt for capturing images for PIV would vary by approximately the same factor.

Sample images from each phase for the $Re_c = 40\text{x}10^3$ test run are shown in Figure 20. The image brightness was unvarying between the first and second images. This was due to the real time exposure time correction capability that was possible, prior to recording image data for results, using the Camware software described in *Section 3.2.1*. The images in Figure 20 are of consistent quality for the $Re_c = 10\text{x}10^3$ pure-plunge case. Note that in this figure the flow is from right to left.
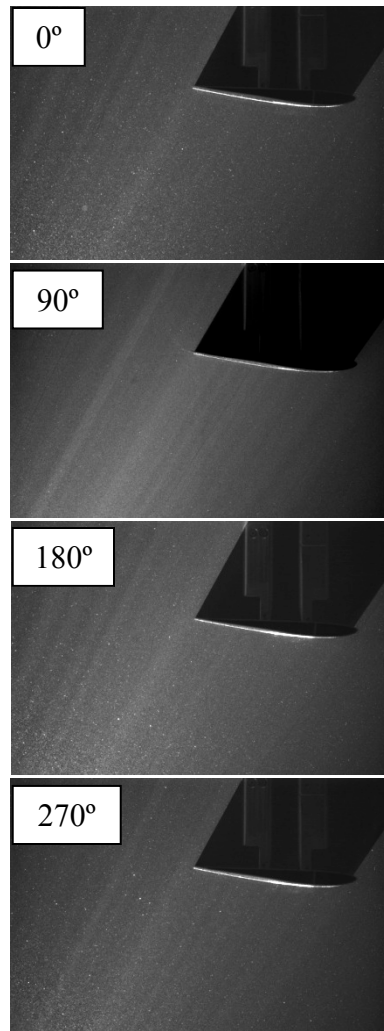
Figure 20: Sample raw PIV images of airfoil at each phase for $Re_c = 40\text{x}10^3$ pure-plunge case, flow from right to left.

Recall that the airfoil is inverted in the water tunnel due to motion rig and laser configuration. During the processing of the images, they are inverted to a proper orientation. The sample images in Figure 20 are rotated by 180º and presented in Figure 21, free stream left to right.
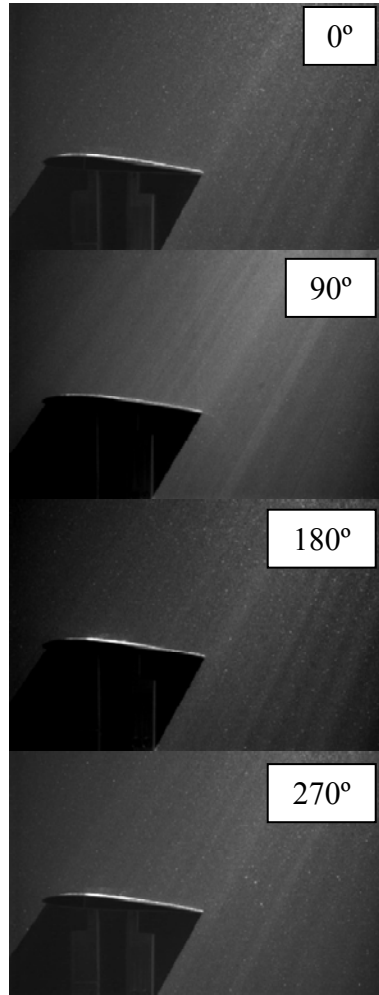
Figure 21: Raw PIV images of airfoil inverted to a traditional orientation for $Re_c = 40x10^3$ pure-plunge case, flow is left to right.

Recall that 120 image pairs are captured, but only 115 image pairs are used for processing in order to avoid the startup effects of a motion. Each of the 115 image pairs formed a unique solution of the flow field. The results of the PIV processing of the pure-plunge cases showed the characteristic flow fields of an airfoil in deep stall. Vortices for both $Re_c = 40x10^3$ and $Re_c = 10x10^3$ formed at the leading edge of the airfoil and traveled along the surface toward the trailing edge. Both velocity contours plots and vorticity contours plots are helpful in illustrating the flow field of an oscillating airfoil. Individual image pair results are shown in the contour plot and vorticity contour plot in Figure 22, non-dimensionalized by the free stream flow.

Velocity (u/U∞)   **Vorticity (ω_z/U∞/c)**
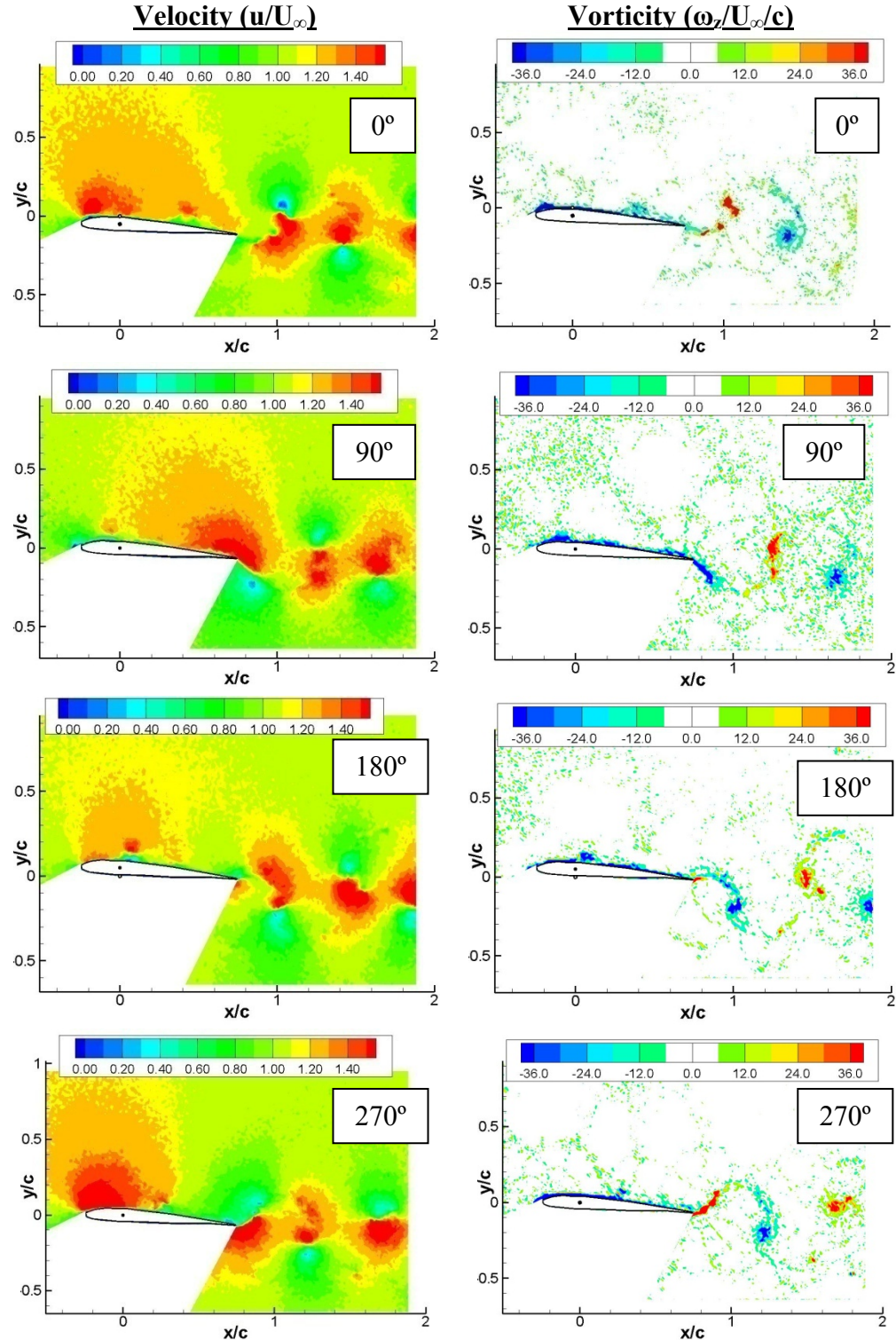
Figure 22: Contour plots of streamwise velocity (u/U∞) and vorticity (ω_z/U∞/c) based on a single

image pair for each phase for pure-plunge Re_c = 40k.

The individual image pair solutions were then phase-averaged in order to form a more accurate solution for the resulting flow field. The velocity contour plots of the resulting flow fields for the pure-plunge case are shown in Figure 23. Figure 24 shows the immersed boundary method (IB) results, $Re_c = 40x10^3$, of the coordinated separate CFD effort (McGowan, Gopalarathnam, Ol, Edwards, & Fredberg, 2008). The 2-D computational results, shown in Figure 23, were in qualitatively excellent agreement with those achieved experimentally. The contour plots are scaled to the free stream velocity.
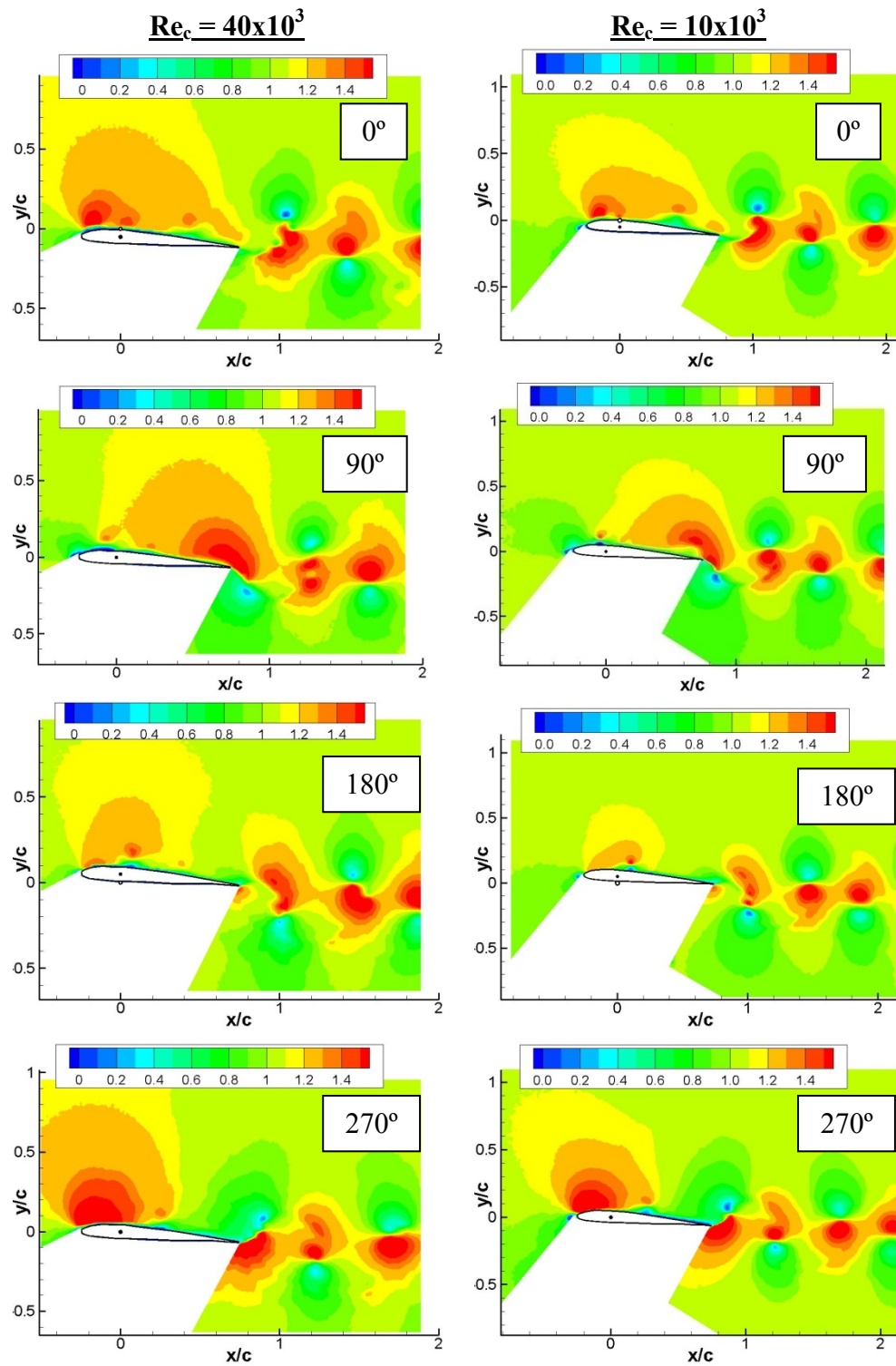
Figure 23: Streamwise velocity (u/U∞) contour plot comparison of Re$_c$=40x10^3 and Re$_c$=10x10^3 for pure-plunge.
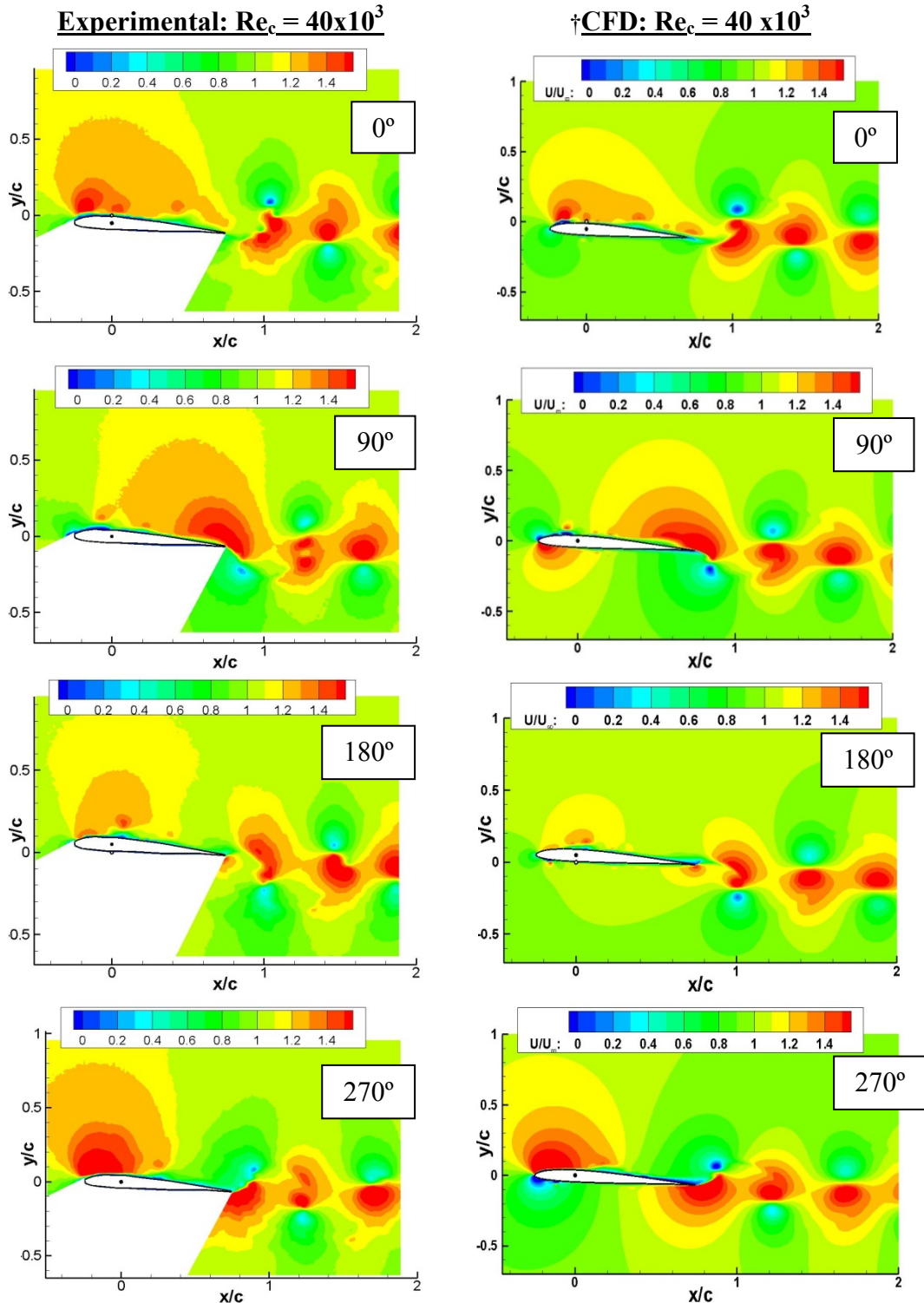
Figure 24: Streamwise velocity contour (u/U$_\infty$) plots comparing experimental pure-plunge results to immersed boundary method CFD results, Re$_c$ = 40x10^3. †(McGowan, Gopalarathnam, Ol, Edwards, & Fredberg, 2008).

The velocity contour plots show a strong shear layer at the trailing edge for both Reynolds number cases. This phenomenon was also captured by both methods used in the separate CFD effort.

The vorticity contour plots for the pure-plunge case are shown in Figure 25. The vortices present in the flow fields of both cases are similar and both show periodicity, justifying the phase-averaging method. Vortex magnitudes vary slightly, but there is no significant change in the overall flow field between the two different Reynolds number cases. The appearance of negative vorticity upstream of the leading edge of the airfoil is probably a side effect of parallax, as discussed in *Section 3.1.3*, and not an accurate portrayal. The separate immersed boundary method CFD results are also compared and shown in Figure 26.
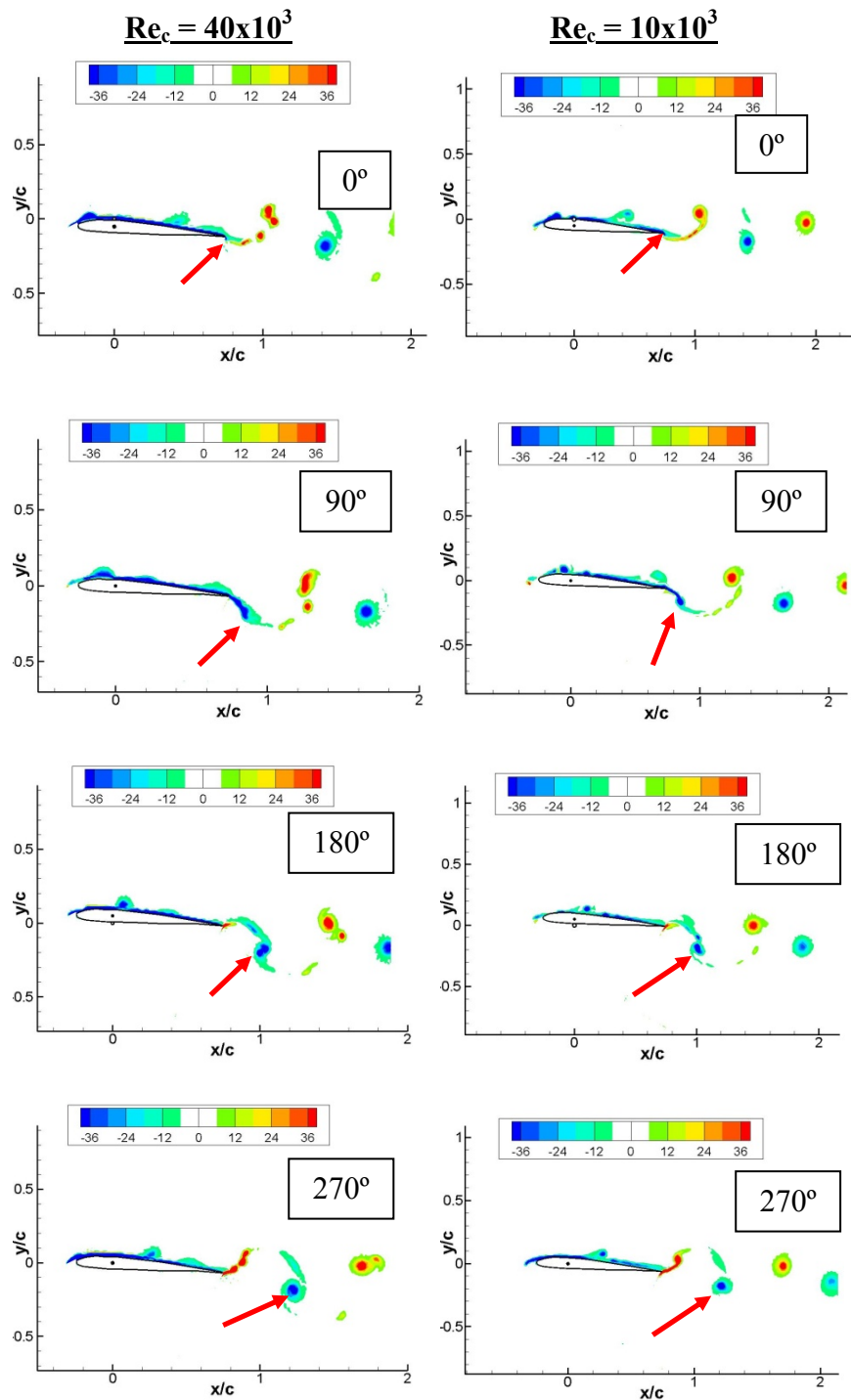
Figure 25: Vorticity ($\omega_z/U_\infty/c$) contour map comparison $Re_c=40x10^3$ and $Re_c=10x10^3$ for experimental pure-plunge results.
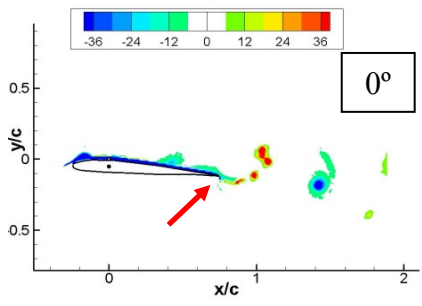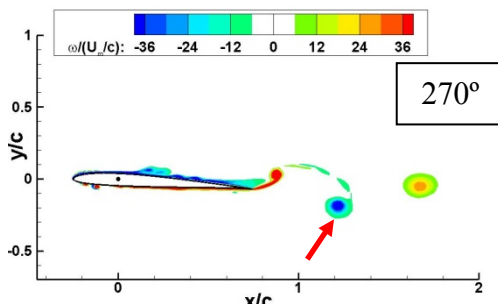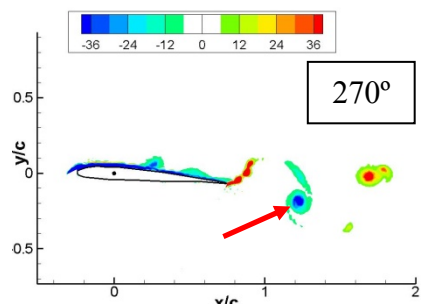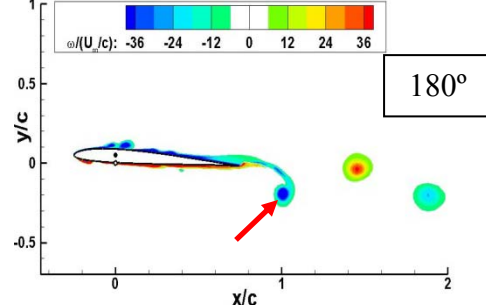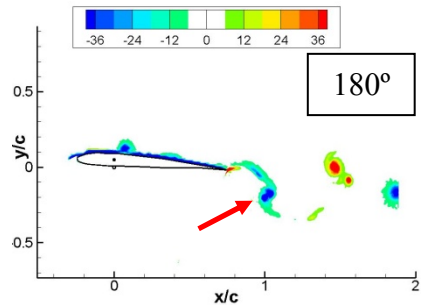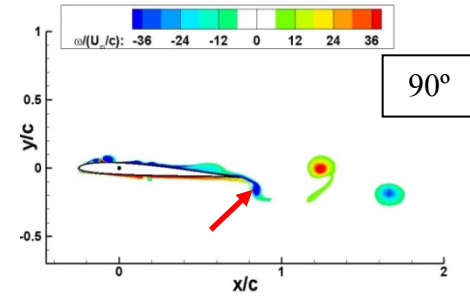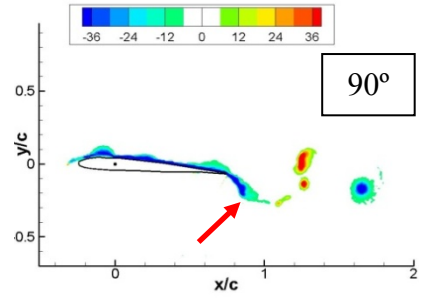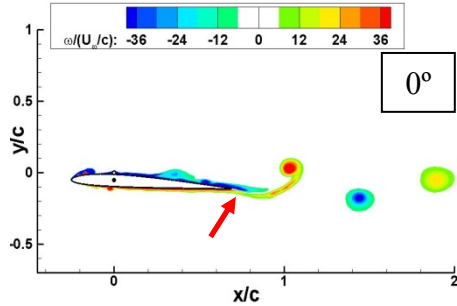
Figure 26: Vorticity ($\omega_z/U_\infty/c$) contour plot comparing experimental pure-plunge results to immersed boundary method CFD results, $Re_c = 40x10^3$. †(McGowan, Gopalarathnam, Ol, Edwards, & Fredberg, 2008).

To further quantify the pure-plunge results, analysis was completed on the location of vortices within the flow field. For both Reynolds number cases and for the immersed boundary CFD method the position of a particular vortex (highlighted by a red arrow in Figure 25 and Figure 26) was tracked during the pure-plunge motion. The origin was placed at the quarter-chord. The vortex position results are presented in Table 5 and based on the point of maximum vorticity within the tracked vortex. For the pure-plunge case the quarter-chord is translating up and down in the y-direction, therefore the vortex position is measured from the quarter chord of the midpoint motion (90º or 270º), where $h = 0$. The tracked vortex was chosen based on its presence in all four phases examined. However, for the first phase, 0º, the vortex had not fully formed and was difficult to observe in all three cases (i.e. $Re_c = 40x10^3$, $Re_c = 10x10^3$, and immersed boundary CFD). Therefore, the vortex location is assumed to be approximately at the trailing edge of the airfoil for all pure-plunge 0º phase cases.

Table 5: Vortex location in reference to quarter-chord for pure-plunge, Re_c=40 x10^3 and Re_c=10x10^3. *Vortex signified by " ➡ " in Figure 25 and Figure 26.

Phase	Experimental		CFD (Immersed Boundary)	
Plunge (Re_c=10x10^3)	x/c	y/c		
0º	0.75	-0.11		
90º	0.85	-0.17		
180º	1.01	-0.18		
270º	1.22	-0.18		
Plunge (Re_c=40x10^3)	x/c	y/c	x/c	y/c
0º	0.75	-0.11	0.75	-0.11
90º	0.85	-0.17	0.85	-0.15
180º	1.02	-0.18	1.01	-0.19
270º	1.23	-0.18	1.22	-0.18

Differences in vortex position, for the pure-plunge $Re_c = 40x10^3$ and $Re_c = 10 x10^3$ cases, were on the order of 1 mm. The results of the CFD vortex position analysis show excellent agreement with that measured experimentally.

The vorticity contour plots, in Figure 25, show what is described by McGowan et al as "fingering" of vorticity, where a shear layer rolls up into a sequence of small discrete vortices (2008). Although present in all the pure-plunge vorticity plots, fingering is more prominent with a higher Reynolds number for the pure-plunge cases. Fingering was not accurately captured by either method in the separate CFD effort. However, the CFD vortex core location results accurately matched those achieved experimentally.

An analysis of the downstream wake was also completed to verify the similar flow fields of the $Re_c = 40x10^3$ and $Re_c = 10x10^3$ pure-plunge case. The velocity wake profiles at x/c = 1.8 downstream of the airfoil quarter-chord are shown in Figure 27.
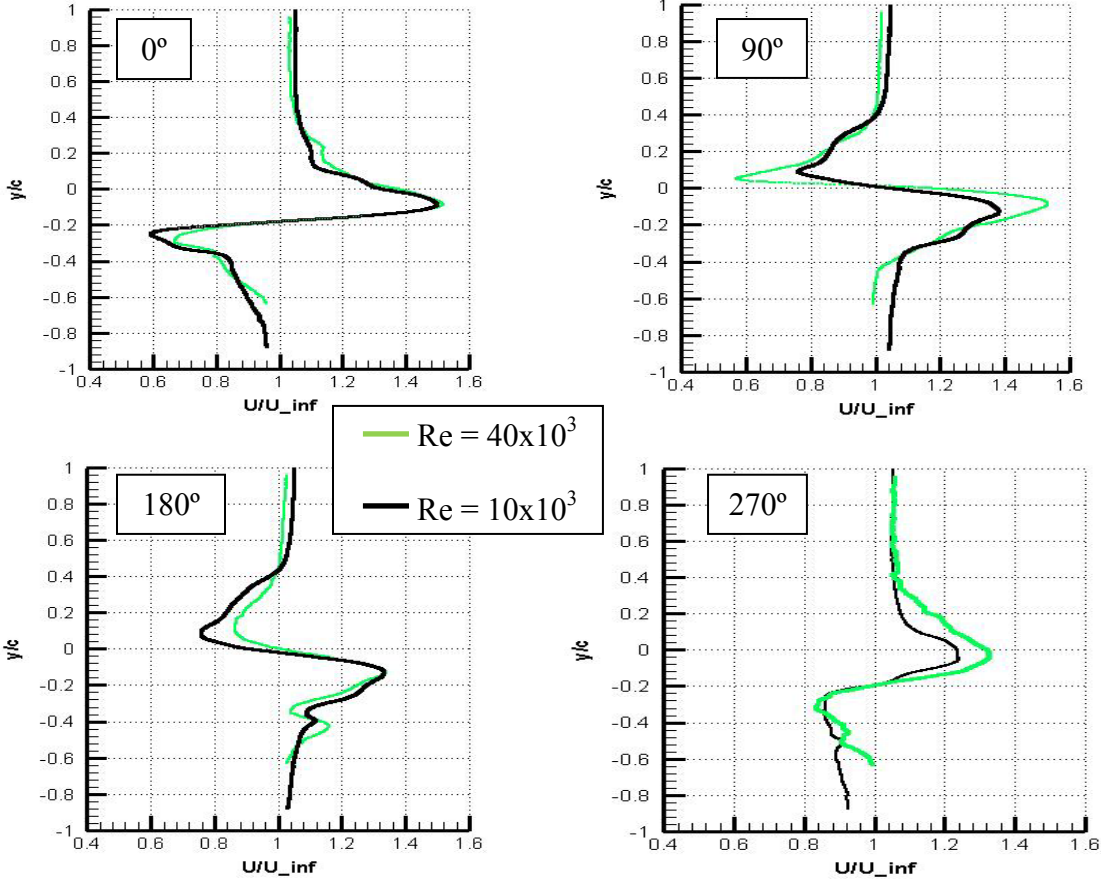
Figure 27: Downstream velocity (u/U$_\infty$) wake profile comparison at x/c = 1.8, for pure-plunge cases, Re$_c$=40x10^3 and Re$_c$=10x10^3.

All the wake data shows good agreement between both cases with similar peaks and valleys. However, at 270° there is a small wake disturbance that differs between each case, but elsewhere shows a similar wake velocity profile.

The results and analysis of the pure-plunge cases show that the deep stall flow fields present are generally insensitive to Reynolds number variations within Re = 10x10^3 to Re = 40x10^3. This is based on the fact that there were no significant inconsistencies found in the comparative results of Re$_c$ = 40x10^3 case and Re$_c$ = 10x10^3 case for a pure-plunge oscillating airfoil.

4.2. Pure-Pitch Case

A pure-pitch experiment was performed at $Re_c = 40\times10^3$ and $Re_c = 10\times10^3$ in order to support or confirm the assumption of negligible Reynolds number effects on a high frequency pure-pitch oscillating airfoil in deep stall. Table 6 shows a summary of the experimental parameters of the pure-pitch cases.

Table 6: Pure-pitch experimental parameters.

	Free-stream velocity (U_∞)	Physical frequency (f)	PIV Δt	Reduced frequency (k)	Strouhal number (St_0)
Pitch $(Re_c=40,000)$	26.5 cm/s	2.13 Hz	1 ms	3.93	0.69
Pitch $(Re_c=10,000)$	6.6 cm/s	0.53 Hz	3.8 ms	3.93	0.69

As in the pure-plunge cases the Reynolds numbers, free-stream velocity, and physical frequency all vary by a factor of four. This was accomplished in order for the reduced frequency to remain equivalent between both Reynolds number cases.

Figure 28 shows example raw images taken during the pure-pitch, $Re_c = 40\times10^3$ experiment.
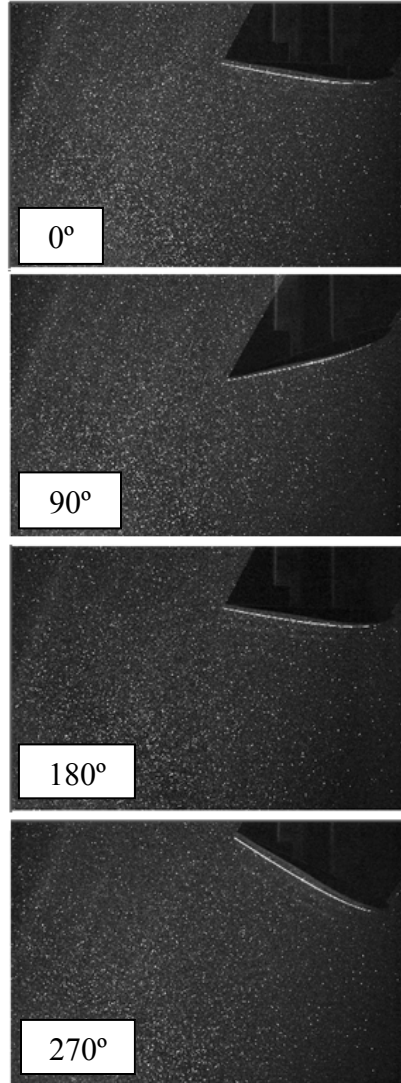
Figure 28: Raw PIV images of airfoil at each point in, $Re_c = 40 \times 10^3$, pitching phase: 0deg, 90deg, 180 deg, and 270 deg, free stream right to left.

Again, the images of Figure 28 are of the inverted airfoil setup in the water tunnel. The conventional orientation of the airfoil with low pressure surface upward is shown in Figure 29, free stream left to right.
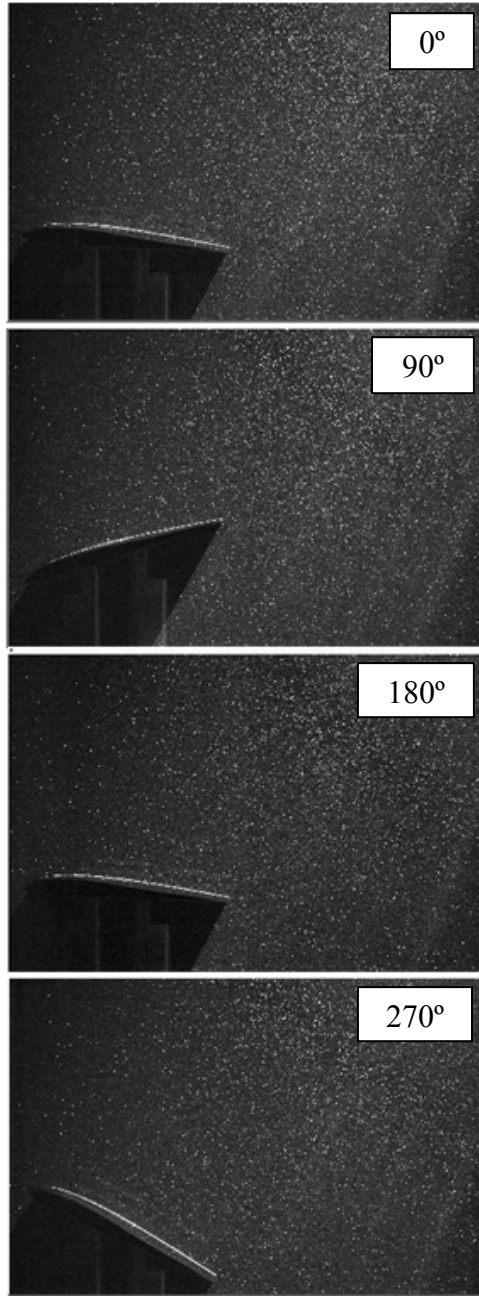
Figure 29: Raw PIV images of airfoil inverted to a traditional orientation for Re$_c$ = 40x10^3 pure-pitch case, free stream left to right.

The particle density of the Re$_c$ = 40x10^3 pure-pitch case was noticeably higher than that of the Re$_c$ = 40x10^3 pure-plunge case previously shown. Particle density can

vary between test runs depending on when the flow was last seeded and/or time between tests. Figure 29 shows an excellent example of good signal-to-noise ratio, high contrast between the particles (white) and the surrounding noise (dark grey or preferably black), as discussed in *Section 2.3*, which correlate to more distinct signal peaks in the cross-correlation solution.

Images like the examples shown in Figure 29 were used to form individual image pair solutions. Example individual image pair solutions are shown in the velocity and vorticity contour plots in Figure 30. Note the increased severity of turbulence in the vorticity contour plots for the pure-pitch motion, especially when compared to the pure-plunge individual image pair plots previously shown in Figure 22, *Section 4.1*.

Velocity (u/U∞) **Vorticity (ω$_z$/U∞/c)**
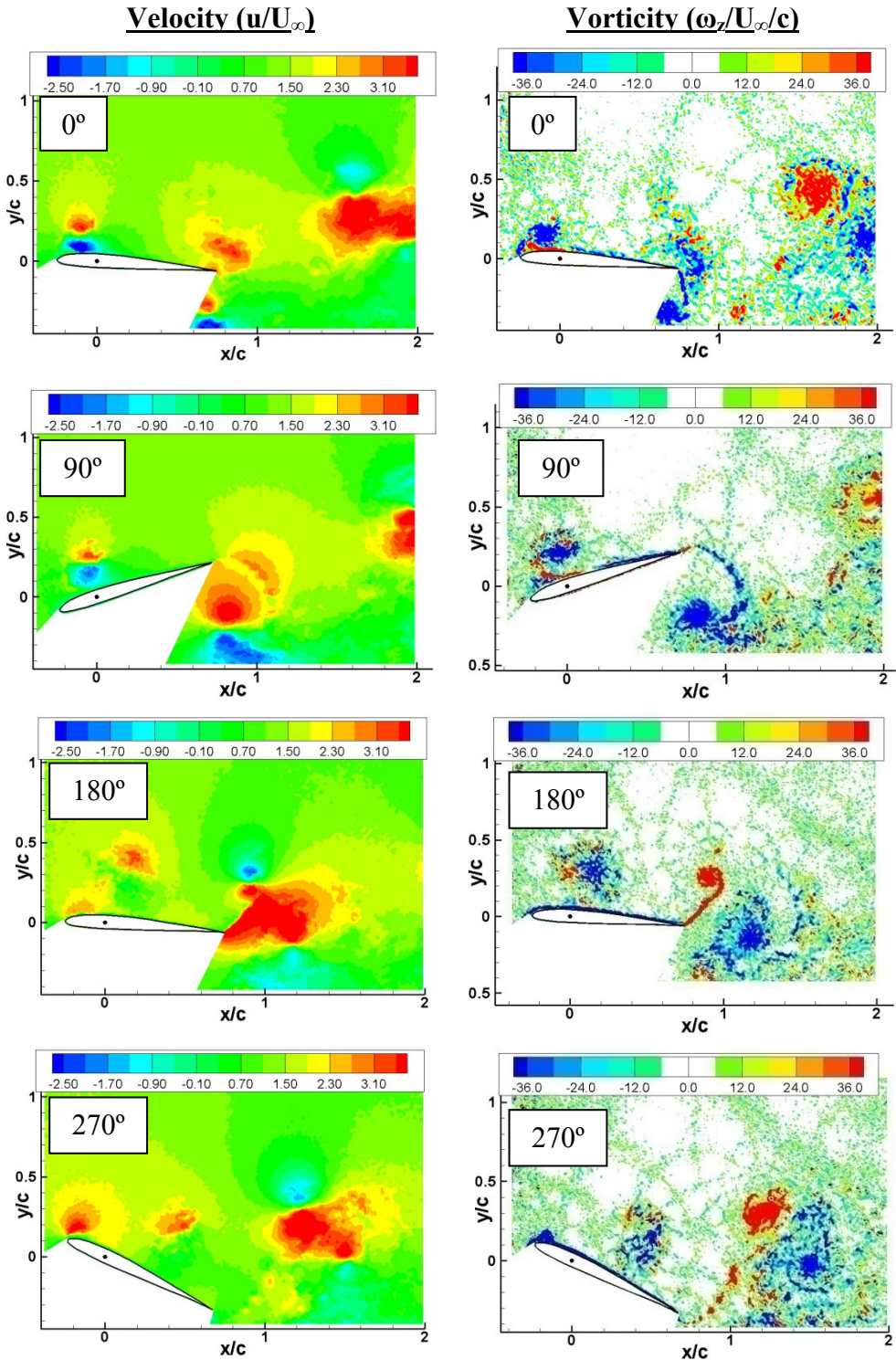
Figure 30: Contour plots of streamwise velocity (u/U∞) and vorticity (ω$_z$/U∞/c) based on a single

image pair for each phase for pure-plunge Re$_c$ = 40k.

The ensuing phase-averaged results of the 115 individual image pair solutions are shown in a velocity contour plot, Figure 31. The pure-pitch $Re_c = 40x10^3$ and $Re_c = 10x10^3$ velocity contours are compared. The separate 2-D computational results using the immersed boundary method are also shown in Figure 32 (McGowan, Gopalarathnam, Ol, Edwards, & Fredberg, 2008).
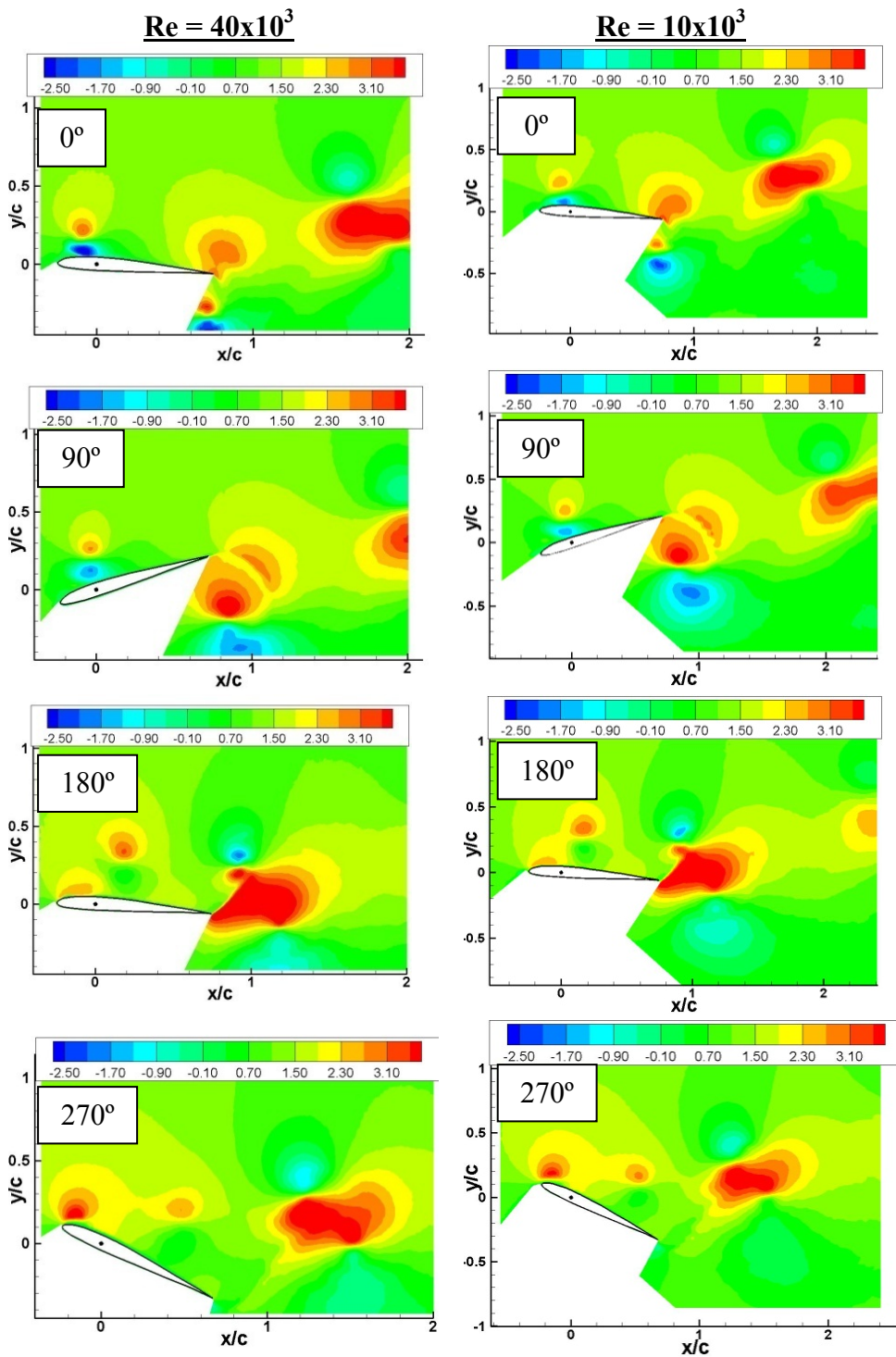
Figure 31: Streamwise velocity (u/U$_\infty$) contour plot comparison Re$_c$ = 40x10^3 and Re$_c$ = 10x10^3 for pure-pitch.

Figure 32: Experimental pure-pitch streamwise velocity (u/U$_\infty$) results compared to immersed boundary method CFD results, Re$_c$ = 40x10^3. †(McGowan, Gopalarathnam, Ol, Edwards, & Fredberg, 2008).

There is an excellent correspondence for the flow fields of the two experimental results taken at $Re_c = 40x10^3$ and $Re_c = 10x10^3$. However, there is a significantly different flow field result for the computational methods used. This difference will be discussed later. Further comparison of the two experimental pure-pitch cases were examined using the vorticity contour plots shown in Figure 33.
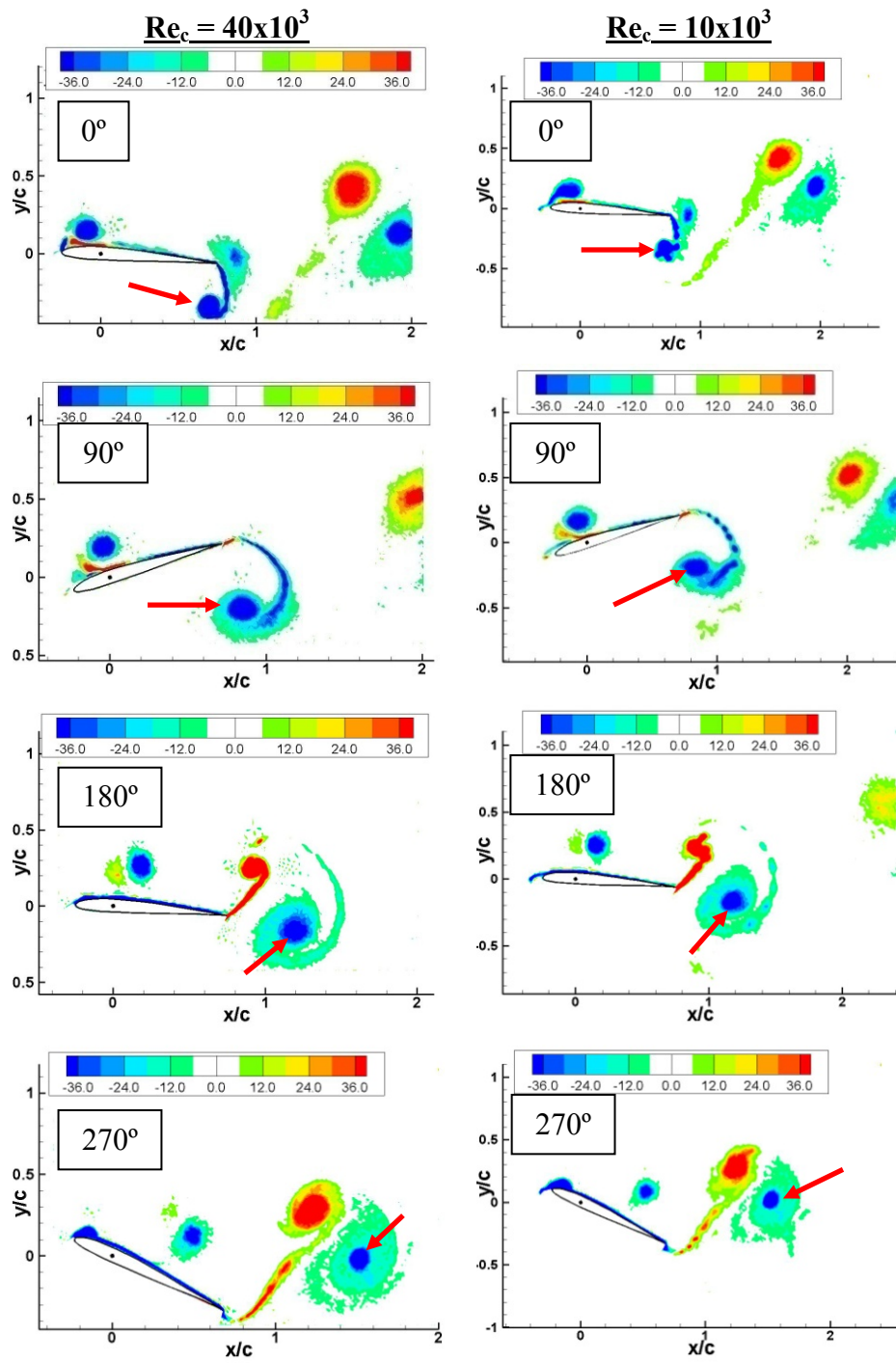
Figure 33: Vorticity ($\omega_z/U_\infty/c$) contour map comparison $Re_c = 40 \times 10^3$ and $Re = 10 \times 10^3$ for pure-pitch.

The immersed boundary method CFD vorticity results were also compared to those achieved experimentally, in Figure 34.
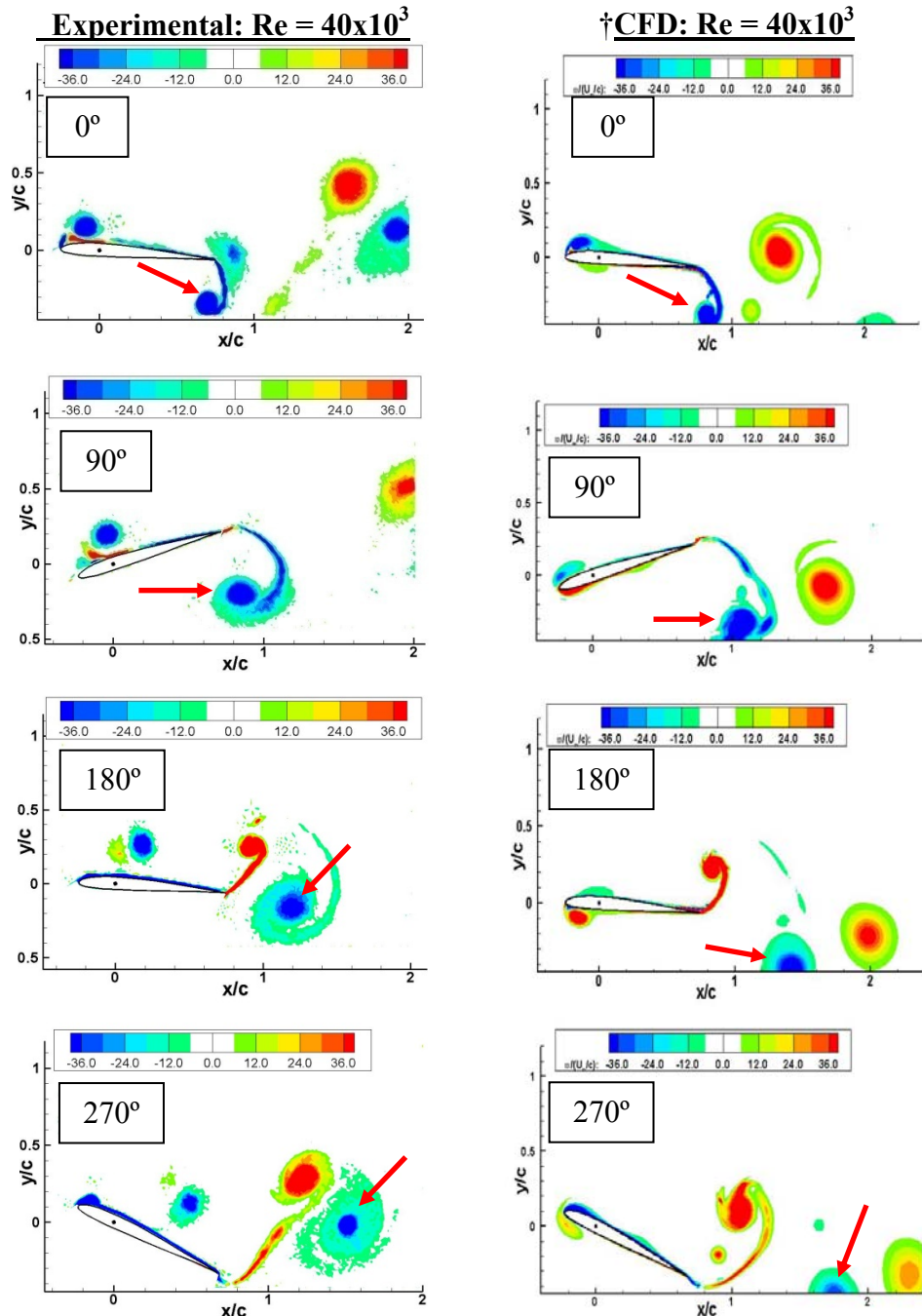
Figure 34: Experimental pure-plunge vorticity ($\omega_z/U_\infty/c$) results compared to immersed boundary method CFD results, Re_c = 40x10^3. †(McGowan, Gopalarathnam, Ol, Edwards, & Fredberg, 2008).

The vorticity contour plots, in Figure 33 and Figure 34, show that the pure-pitch oscillating airfoil has a deep stall flow field. The vortices were formed at the leading edge and proceeded to travel downstream. Vortex fingering was also apparent in the pure-pitch case. However, unlike the pure-plunge case, fingering was more prominent at the lower Reynolds number.

Another phenomenon present in the pure-pitch flow field is the apparent inclined angle of the vortex street. This, however, is not totally unexpected since similar flow fields have been documented for plunging airfoils at high Strouhal numbers (Lai & Platzer, 1999). Lai and Platzer indicated that with a maximum non-dimensional plunge velocity greater than one, $kh_o>1$, vortex streets inclined upward were observed (1999). For the pure-pitch case at hand, if h_o, defined by the maximum y-position of the trailing edge and the reduced frequency, k, was 3.93, then the maximum non-dimensional "pitch" velocity is $kh_o = 1.08$.

The wake structures of the computational results for the pure-pitch case, previously shown in Figure 34, were markedly different than those achieved experimentally. Test section walls (i.e. top and bottom of test section) were modeled in the CFD with the same result and free stream turbulence was examined prior to testing with no significant disturbances observed (McGowan, Gopalarathnam, Ol, Edwards, & Fredberg, 2008). However, the surface deformation (i.e. free surface) was not modeled, but treated as another wall. The flow fields of the pure-pitch show more turbulence in the flow field compared to the pure-plunge test, evident in single image pair solutions. Definite reason for the lack of agreement between the experimental and computational pure-pitch results is presently left unresolved. However, the disagreement is thought to

be with the computations since there was also a lack of agreement between the CFL3D and immersed boundary methods results detailed by McGowan et al (2008). Further investigation into the 2-D assumption of both CFD methods is recommended, since there is evidence of possible 3-D effects on the resulting flow fields.

The wake structures for the pure-pitch cases of different Reynolds numbers, like the plunge cases, are in excellent agreement. To further quantify their similarity, the location of a particular vortex (highlighted with a red arrow in Figure 33 and Figure 34) was tracked with respect to the quarter-chord. Unlike the pure-plunge cases, the quarter-chord was stationary for the pure-pitch cases. The vortex position results for the pure-pitch $Re_c = 40x10^3$, $Re_c = 10x10^3$, and the $Re = 40x10^3$ immersed boundary CFD cases are shown in Table 7 and are based on the point of maximum vorticity within the tracked vortex.

Table 7: Vortex location in reference to quarter-chord for pure-pitch, Re=40x10^3 and Re=10x10^3.

Vortex signified by "➡" in Figure 33 and Figure 34.

Phase	Experimental		CFD (Immersed Boundary)	
Pitch (Re$_c$=10x10^3)	x/c	y/c		
0°	0.70	-0.33		
90°	0.84	-0.19		
180°	1.17	-0.17		
270°	1.52	0.02		
Pitch (Re$_c$=40x10^3)	x/c	y/c	x/c	y/c
0°	0.70	-0.34	0.82	-0.39
90°	0.85	-0.20	1.07	-0.33
180°	1.20	-0.16	1.42	-0.44
270°	1.52	-0.02	1.76	-0.48

The experimental position results in Table 7 further show the similar wake structures of the experimental pure-pitch oscillating airfoil cases, without regards to their respective Reynolds number. Differences in position are between <1 mm and 3 mm. The vortex position was based on the point of maximum vorticity within the vortex. The computational results for vortex location were in disagreement with those experimentally obtained. Furthermore, the apparent positive inclination of the vortex of street observed experimentally was not present in computational results.

A wake analysis was also performed in order to further analyze the flow fields of a pure-pitch oscillating airfoil at $Re_c = 40\text{x}10^3$ and at $Re_c = 10\text{x}10^3$. The results of the experimental wake analysis were in excellent agreement with each other for all phases and are shown Figure 35. The velocity wake profile of 90º is similar, same peaks and valleys, but the magnitudes are greater for the $Re = 40\text{x}10^3$ case.
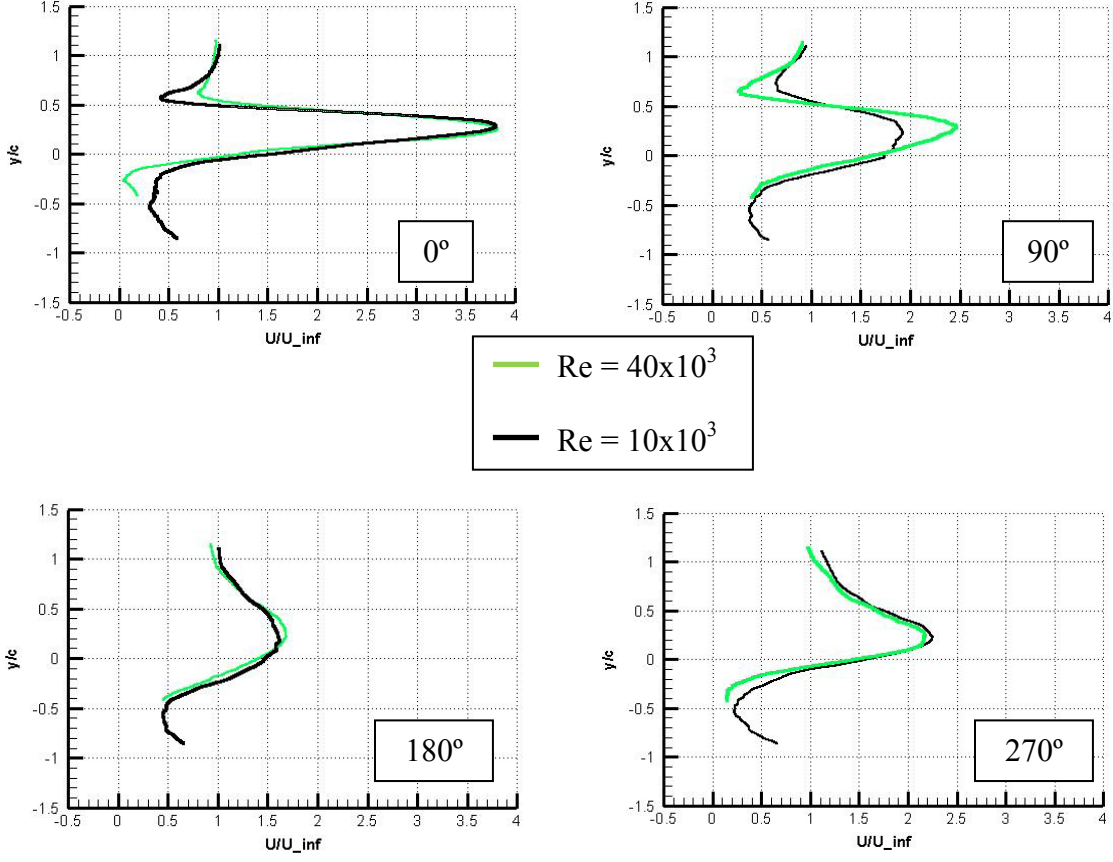
Figure 35: Downstream velocity (u/U∞) wake profile comparisons at x/c = 1.8 for pure-pitch cases, Re_c=40x10³ and Re_c=10x10³ (McGowan, Gopalarathnam, Ol, Edwards, & Fredberg, 2008).

The initial assumption that Reynolds number effects have little effect on the high-frequency motions researched was validated for a pure-pitch oscillating airfoil in deep stall. There were no significant discrepancies between the Re = 40x10³ case and the Re = 10x10³ case. However, the immersed boundary CFD results were markedly different. The reason for the CFD method results inconsistency with those achieved experimentally remains unresolved and deserving of further investigation (McGowan, Gopalarathnam, Ol, Edwards, & Fredberg, 2008).

4.3.   Pure-Plunge and Pure-Pitch Comparison

The overarching purpose of this research is to compare the deep stall flow fields of a pure-plunge and pure-pitch oscillating airfoil.   The results, previously discussed independently, are summarized in order to identify dissimilarities that existed in the flow field.   Table 8 shows a summary of the experimental parameters for the $Re_c = 40x10^3$ pure-plunge and pure-pitch cases.

Table 8: $Re_c = 40x10^3$ pure-plunge and pure-pitch experimental parameters.

	Free-stream velcocity (U_∞)	Physical frequency (f)	Reduced frequency (k)	Strouhal number (St)	Effective AOA (a)
Plunge (Re$_c$=40,000)	26.5 cm/s	2.13 Hz	3.93	0.12	4°± 21.5°
Pitch (Re$_c$=40,000)	26.5 cm/s	2.13 Hz	3.93	0.69*	4°± 21.5°

Note that the effective angle of attack is matched for both motions.   Recall that the effective angle of attack is achieved by the motion-induced angle of attack for the pure-plunge case and by the geometric angle of attack for the pure-pitch case.

Figure 36 shows the velocity contour plots with matched effective angle of attack for the pure-plunge and pure-pitch cases at $Re_c = 40x10^3$.   The flow fields interpreted from the velocity contour plots show that they are distinctly different.   Scales for each plot were made equivalent in order to have a better visual representation for the comparison of the pure-plunge and pure-pitch cases.
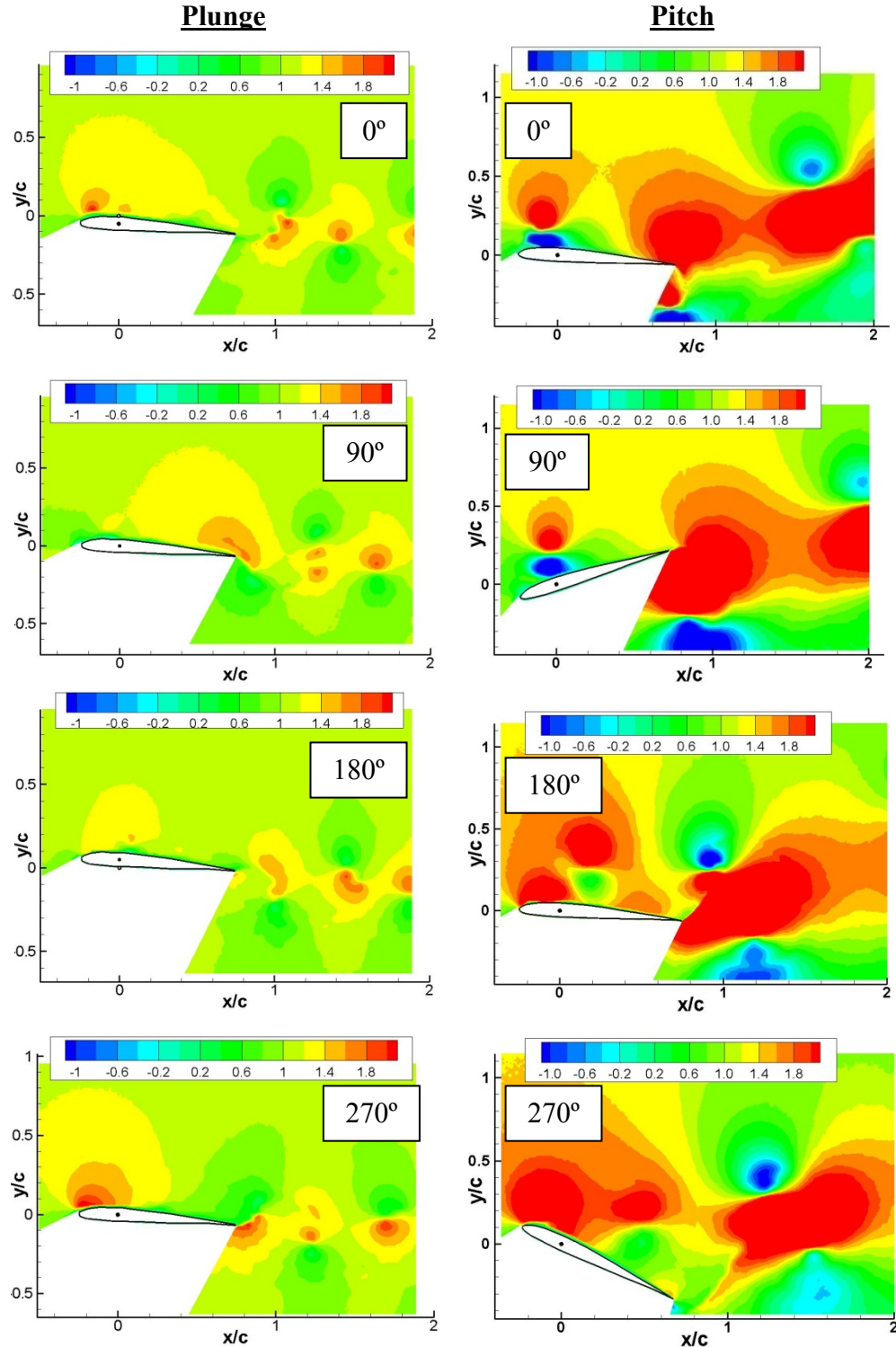
Figure 36: Contours of the streamwise component of velocity (u/U_∞) for comparing pure-plunge to pure-pitch for $Re_c = 40 \times 10^3$ with equivalent effective angles of attack.

Not only are the pure-pitch flow field structures vastly different from those of the pure-plunge case, but the velocities of the flow field are of magnitudes significantly greater than those of the pure-plunge case. This difference in velocity could possibly be attributed to the differences of the trailing edge kinematics between each case, as discussed in *Section 3.1.2*. To illustrate the impact of the trailing edge kinematics, the velocity contour plots were scaled to the maximum trailing edge velocity perpendicular to the free stream flow, v_{TEmax}, is shown in Figure 37.
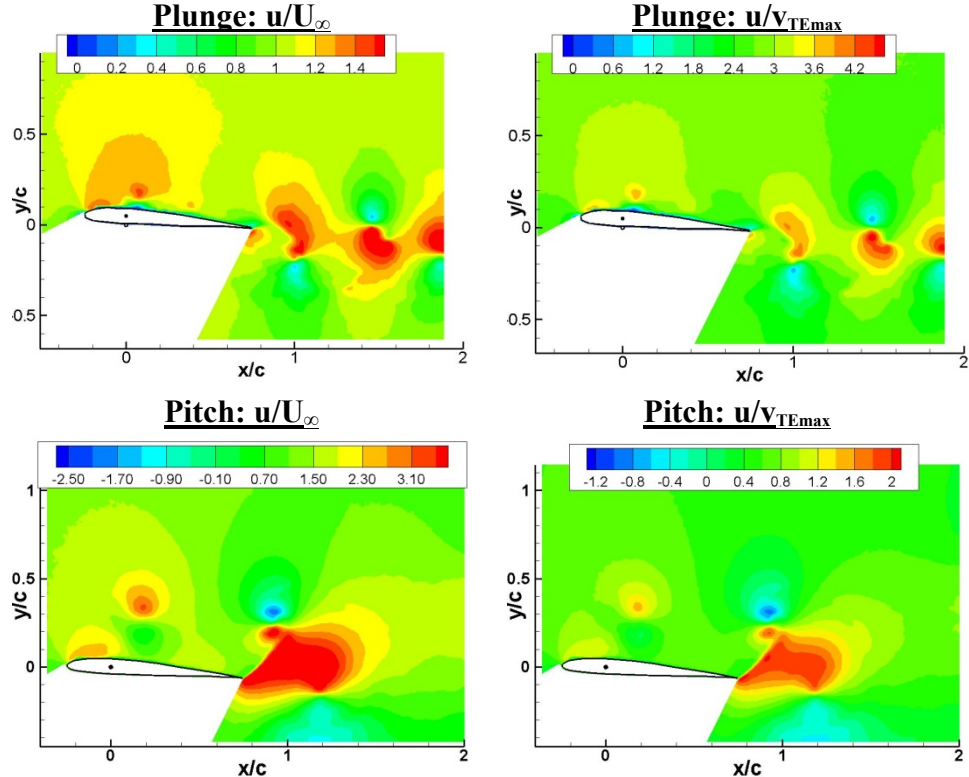
Figure 37: Contours of the streamwise component of velocity (u) scaled to the maximum trailing edge velocity (v_{TEmax}) for pure-plunge case and pure-pitch case at $Re_c = 40 \times 10^3$.

Note the different scales of Figure 37. When normalized by the free stream velocity (U_∞) the pure-pitch case shows the largest velocity magnitudes. However, when non-dimensionalized by the maximum trailing edge velocity perpendicular to the free stream flow, v_{TEmax}, the pure-plunge case shows a greater velocity magnitudes compared to the pure-pitch case. This further illustrates the significantly higher velocities experienced by the trailing edge of the pure-pitch case when compared to the pure-plunge case.

In order to further discriminate the flow fields of the two cases, the vorticity contour plots are shown in Figure 38.
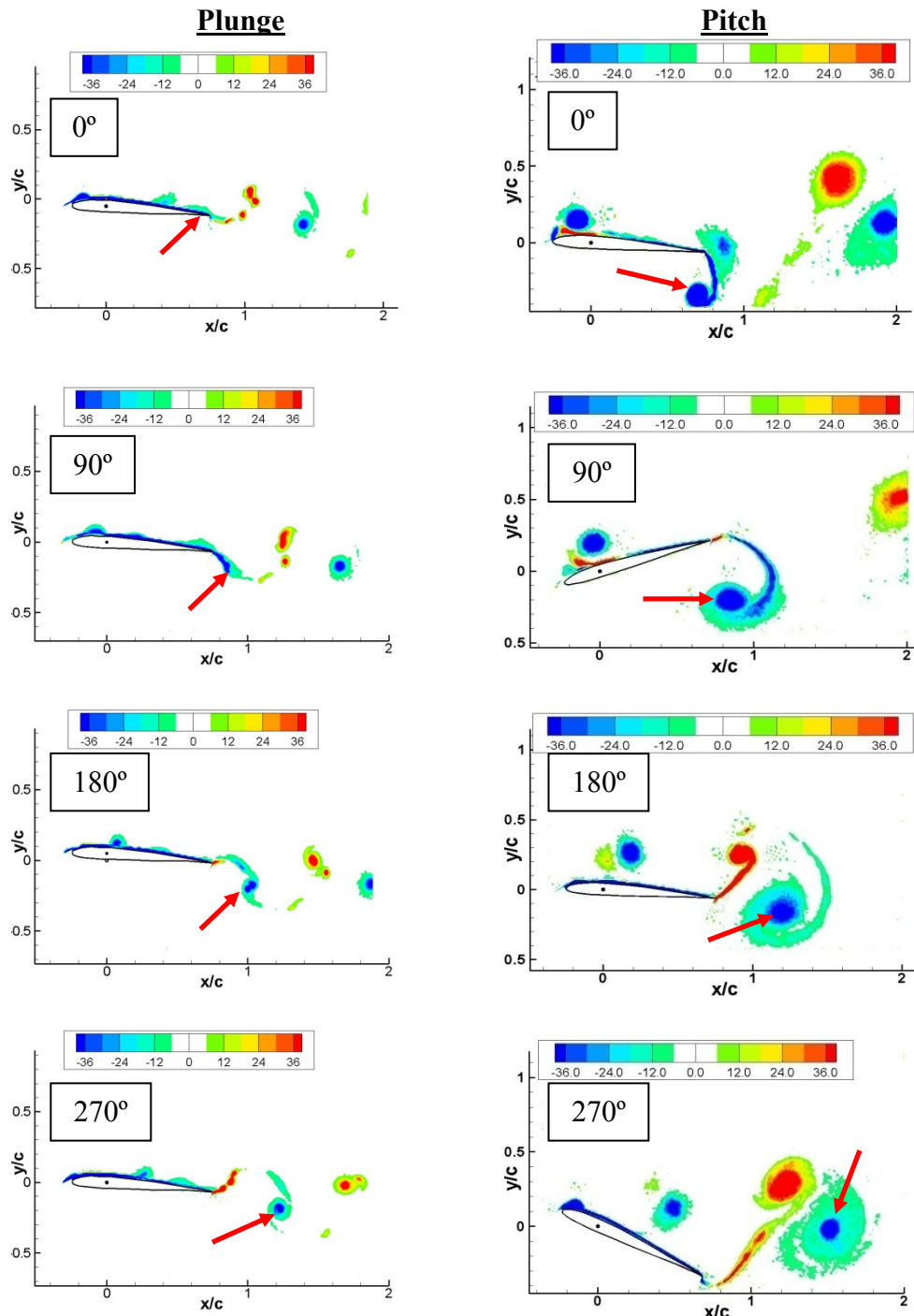
Figure 38: Vorticity ($\omega_z/U_\infty/c$) contours for comparing pure-plunge to pure-pitch for Re$_c$ = 40x10^3.

The vorticity plots of the pure-plunge and pure-pitch cases, Figure 38, show obvious differences in the vortex formations of the flow. Although both airfoils experience deep stall, the vortices of the pure-pitch case are more pronounced and of higher magnitude. The prominent difference between the pure-plunge and pure-pitch case are especially evident at the trailing edge. The pure-pitch trailing edge heave amplitude is much greater than that of the pure-plunge case, as discussed in *Section 3.1.2*. The kinematic differences of the trailing edge seem to be a root cause for the nontrivial differences in each respective flow field. These observations raise basic questions on the validity of matching reduced frequency and effective angle of attack at the quarter chord. Furthermore, nontrivial nonlinearities may be present in the resulting flow fields for a given angle of attack time history.

The position of the vortex highlighted by the red arrow in Figure 38 was measured with respect to the quarter chord. For the pure-pitch case, the quarter-chord is stationary, however for the pure-plunge case it translates as the airfoil heaves perpendicular to the free stream flow. The quarter-chord used for the vortex position analysis was at the midpoint of the pure-plunge motion (quarter-chord location of phases 90º and/or 270º). The results, shown in Table 9, confirm the dissimilarity of the pure-plunge and pure-pitch cases. Positional differences range from 1 mm to 45 mm. Any positional similarities are concluded coincidental since flow fields are so markedly different.

Table 9: Vortices location in reference to quarter- chord comparing pure-plunge and pure-pitch at

$Re_c = 40x10^3$.

Phase	Vortex Coordinates (" → ")	
Plunge ($Re_c = 40 \times 10^3$)	x/c	y/c
0º	0.76	-0.12
90º	0.85	-0.17
180º	1.02	-0.18
270º	1.23	-0.18
Pitch ($Re_c = 40x10^3$)	x/c	y/c
0º	0.70	-0.34
90º	0.85	-0.20
180º	1.20	-0.16
270º	1.52	-0.02

To further illustrate the different resulting flow fields of the pure-plunge case and pure-pitch case, the downstream velocity wake profiles of each case are shown in Figure 39.
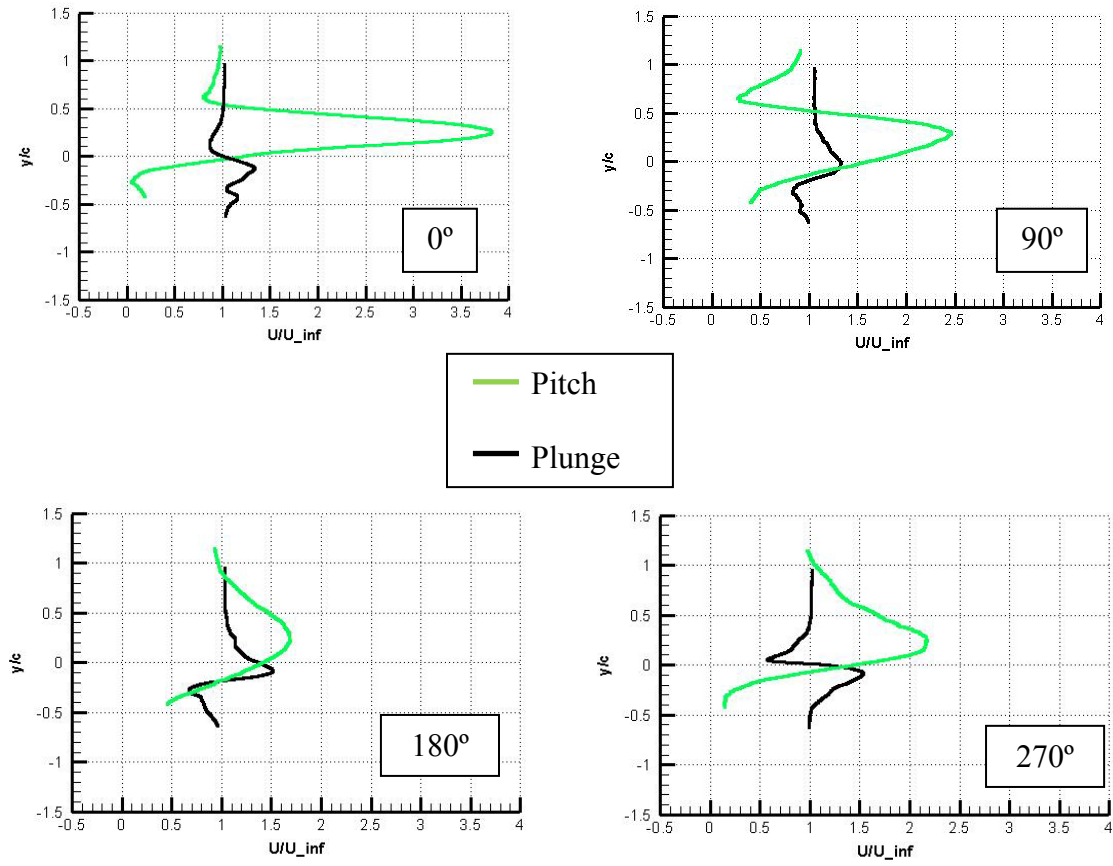
**Figure 39: Downstream velocity (u/U∞) wake profile comparisons at x/c = 1.8 for pure-plunge case and pure-pitch case, Re$_c$=40x10^3.**

The wake profiles, peaks and valleys, and magnitudes show no correlation between the pure-plunge case and pure-pitch case.

4.4. Further discussion

The results of the additional experiments discussed in *Section 3.1.4* offer further opportunity for understanding the flow fields of oscillating airfoils and the capabilities of the HIPPO. These PIV results require more analysis to be useful in determining the effects of combined pitch and plunge motions. Due to time restrictions, a proper analysis of these separate pitch and plunge results was not attempted here. However, the results given in Appendix C offer some proof that the HIPPO is capable of providing useful information for future research.

5. Conclusions and Recommendations

5.1. Research Conclusions

The flow fields of a pure-plunge oscillating airfoil and pure-pitch oscillating airfoil were successfully examined using PIV in the AFRL/RB water tunnel using their HIPPO system. Results of the test cases lead to several conclusions.

(1) At a high reduced frequency, $k = 3.93$, a pure-plunge oscillating airfoil in deep stall shows little Reynolds number sensitivity within the range tested, Re = $40\text{x}10^3$ and Re = $10\text{x}10^3$. Resulting flow fields were in excellent correspondence with one another for the Re = $40\text{x}10^3$ and the Re = $10\text{x}10^3$ cases. The wake structure of each Reynolds number case showed periodicity, justifying the phase-averaging method used for attaining PIV results. Vortex "fingering" was evident in both pure-plunge cases, but more prominent with the higher Reynolds number. The 2-D CFL3D and immersed boundary method results showed good quantitative agreement with those achieved experimentally for the pure-plunge cases.

(2) The flow field of pure-pitch oscillating airfoil at high reduced frequency, $k = 3.93$, also experiences the aerodynamic phenomenon associated with deep stall. The variation of Reynolds number had little effect on the resulting flow fields for the Re = $40\text{x}10^3$ and Re = $10\text{x}10^3$ pure-pitch cases, as documented by previous research. Vortices

in both flow fields were very pronounced, respectively, and formed an apparent inclination of the vortex street. Considering documented results from previous research of a pure-plunge oscillating airfoil with similar non-dimensional "plunge" velocity, the vortex street inclination was not totally unexpected. Vortex "fingering" was evident in both the pure-pitch cases. However, unlike the pure-plunge case, vortex fingering was more evident at the lower Reynolds number. Both computational methods failed to capture accurate portrayals of the flow fields for both Reynolds number cases when compared to those accomplished experimentally. The flow fields of a pure-pitch oscillating airfoil are complex and it is believed that the computational disagreement could be due to the initial 2-D assumption of the problem and/or the robustness of either solution method performed. The lack of agreement between computational methods further supports the argument against their respective ability to correctly solve such a complex flow field.

(3) The flow field of a pure-plunge oscillating airfoil was compared to that of a pure-pitch oscillating airfoil using PIV. Based on other oscillating airfoil research, certain parameters were matched at the quarter chord of the airfoil, the reduced frequency and effective angle of attack. The motion-induced angle of attack for the pure-plunge case was matched to the geometric angle of attack of the pure-pitch case. Results from the experiment point to inaccuracy in the assumption that the deep stall flow field of a pure-plunge oscillating airfoil is equivalent to that of a pure-pitch oscillating airfoil when the effective angles of attack are matched. The wake structures of each case were markedly different as observed in velocity and vorticity contour plots, both in magnitude

and vortex position. Analysis of the trailing edge kinematics of each case show large disagreement and is a probable source for wake structure disagreement in experimental results.

5.2.   Impact of this Research

The goal of the information detailed in this report is to spur on further research in to what, if any, parameters of a pure-plunge and pure-pitch oscillating airfoil would have to be matched in order to have similar resultant flow fields. Understanding these parameters would allow researchers the ability to better understand and predict wake structures for MAV's or other flapping wing technology. Furthermore, successful computational modeling of the complex flow fields of oscillating airfoils would confirm or refine researcher's understanding of this subject. The improved knowledge of oscillating airfoils could potentially lead to breakthroughs in propulsive technologies, aircraft stability and control, and MAV design.

5.3.   Recommendations

Further research is warranted in this area. First and foremost a similar experiment needs to be performed examining points along the chord, other than the quarter-chord, at which kinematic properties could be matched in order to achieve, if possible, similar resulting flow field for a pure-plunge case and a pure-pitch case. The effect of matching the Strouhal number on the flow field should be taken into consideration, especially at the trailing edge where the positions are vastly different between pure-plunge and pure-pitch.

The reduced frequency and effective angle of attack were matched at the quarter-chord for the pure-plunge and pure-pitch cases, and the flow field results showed inequality. Some sort of point sweep along chord with the same matched parameters should be researched in order to justify or dismiss making them equivalent for the pure-pitch and pure-plunge cases.

As part of the CFD-validation process, out of plane velocities should be examined using Stereo PIV. Significant spanwise motion would lead to a breakdown of the 2-D flow assumption used in this CFD study. The full 3-D observation of the flow field could offer some insight into improving computational methods of such complex flow fields.
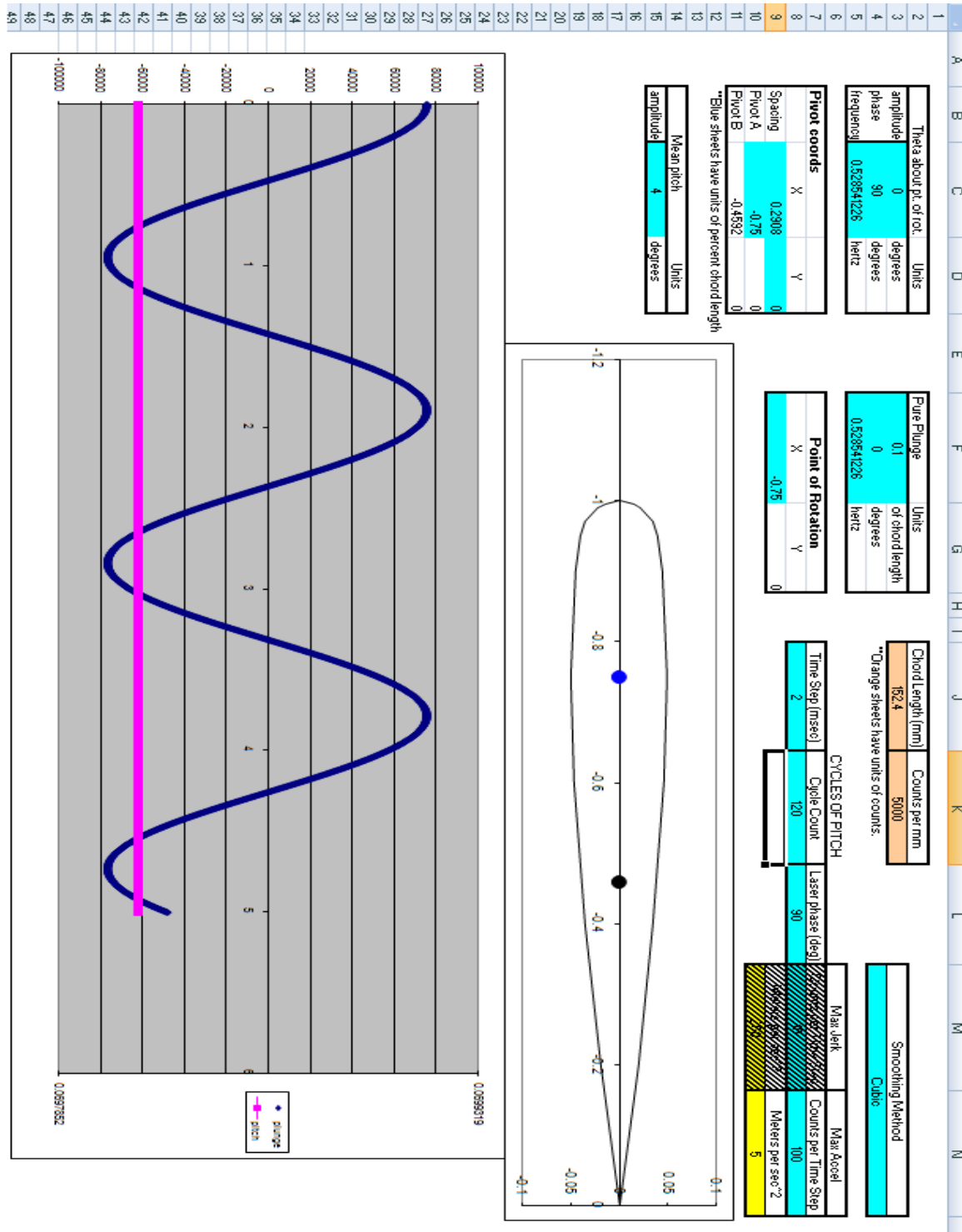
Appendix B: PIV Processing Software

(Jeon, 2000)

Example processing perl script

```
$strt = 1001;
$strtpsycho = 1006;
$last = 1121;
$inc = 1;
$first = a;
$second = b;
$outstub = z;
$parfile = par3216;
$convparfile = cpar3216;
$psychostringmean = avg;
$psychostringprime = prime;
$psychostringcross = cross_prime;
$psychocross = rr;
$psychoprime = pp;
$psychomean = mn;
$pivout = fsx;
$vorout = vor;
$psychovor = ww;

$pivfam = fa;

for ($filenum=$strt;$filenum<=$last;$filenum+=$inc)

{

      system "dpiv -c $parfile.par $pivfam$filenum$first.raw
$pivfam$filenum$second.raw $pivfam$filenum.piv";
      system "fix_data 2 $pivfam$filenum.piv $pivfam$filenum.fix";
      system "smooth $pivfam$filenum.fix $pivfam$filenum.smo";
      system "smeg -c $parfile.par $pivfam$filenum$first.raw
$pivfam$filenum$second.raw $pivfam$filenum.smo $pivfam$filenum.smg";
      system "fix_data 3 $pivfam$filenum.smg $pivfam$filenum.fsx";
      system "del $pivfam$filenum.smo";
      system "del $pivfam$filenum.fix";
      system "convdpiv -c $convparfile.par $pivfam$filenum.fsx
$outstub$pivfam$filenum.fsx";
      system "vortage $outstub$pivfam$filenum.fsx
$outstub$pivfam$filenum.vor";
}

      system "psycho 2 $outstub$pivfam $pivout $strtpsycho $last 1";
      system "bintotec avg u/U_~% v/U_~% -o $psychomean$pivfam.dat
$outstub$pivfam$psychostringmean.$pivout";
      system "bintotec Re_stress u'v'/U_~%^2 dummy -o
$psychocross$pivfam.dat $outstub$pivfam$psychostringcross.$pivout";
      system "psycho 1 $outstub$pivfam $vorout $strtpsycho $last 1";
      system "bintotec vor omega -o $psychovor$pivfam.dat
$outstub$pivfam$psychostringmean.$vorout";
```

Processing software

dpiv

Main DPIV processing software. Perform cross correlation of image pair.

fix_data

Checks for outliers greater than the user determined threshold and replaces them with the average of neighbors.

smooth

Iterative filter to reduce noise in the image data

smeg

Window shifting and spatial windowing version of DPIV. Used after DPIV has already run. Further reduces noise by increasing the number of matching particles in the two interrogation windows

convpiv

Converts units from pixels to cm using user created par file (based ruler image results).

vortage

Computes vorticity using analytical derivatives of natural splines. Considered a good way to compute derivatives of high order without suffering from excessive noise. Although more sensitive to noise than a more typical vorticity computation program, it has significantly better spatial resolution.

psycho

Time statistics program. Computes averages and fluctuating quantities and various correlations. Operates on scalars, vectors, vectors with scalars, and scalars with scalars. Operates on sequences of files, but can safely skip missing files- a useful feature for phase-averaging.

bintotec

Converts a DPIV binary file into TecPlot friendly text file.

Appendix C: Additional Experimental Cases
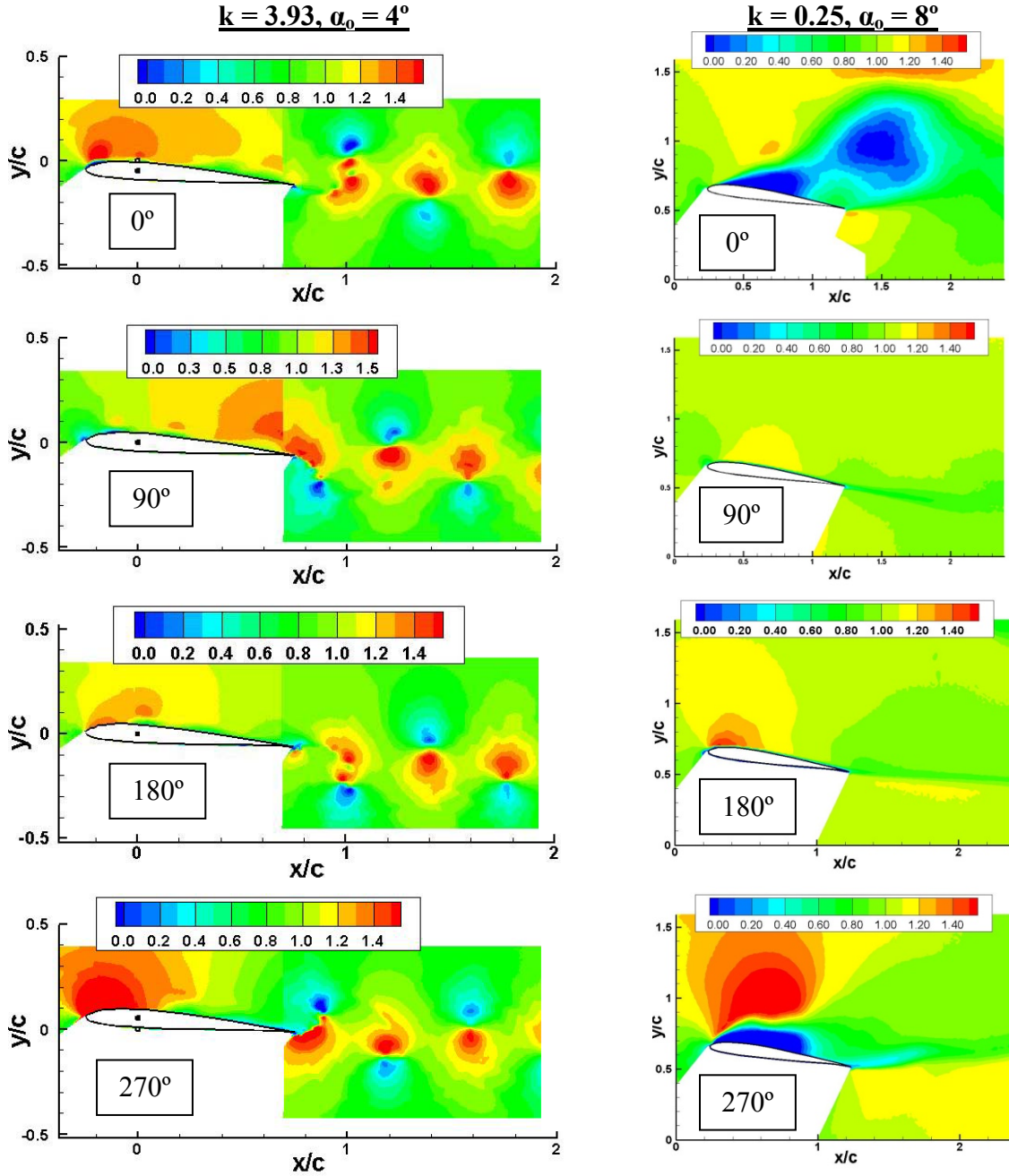
Figure 40: Velocity (u/U$_\infty$) contours examining reduced frequency effects for pure-plunge for *k* = 3.93 and *k* = 0.25, Re = 60x10^3.

k = 3.93, α₀ = 4°   **k = 0.25, α₀ = 8°**
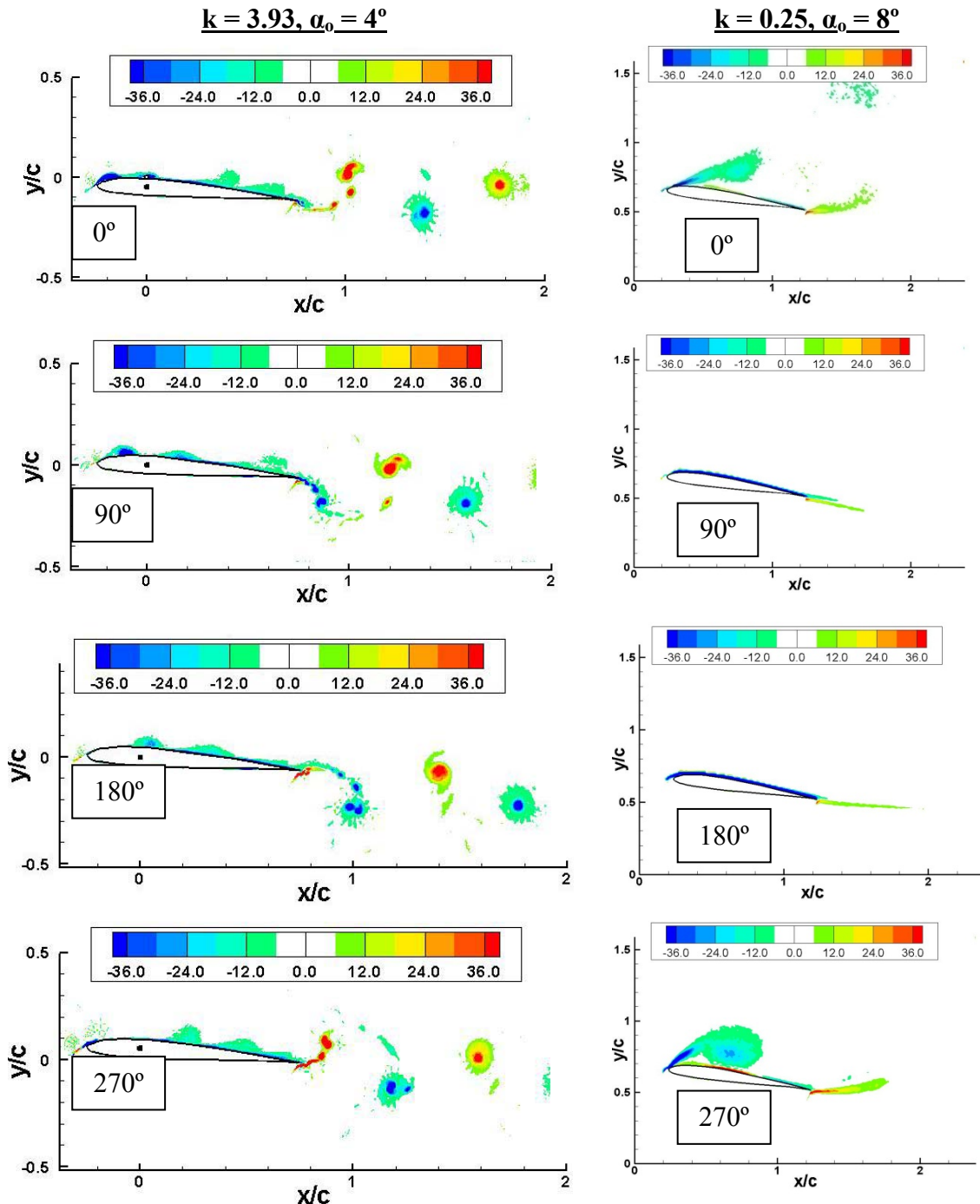

Figure 41: Vorticity ($\omega_z/U_\infty/c$) contours examining reduced frequency effects for pure-plunge for $k =$ 3.93 and $k = 0.25$, Re = 60×10^3.
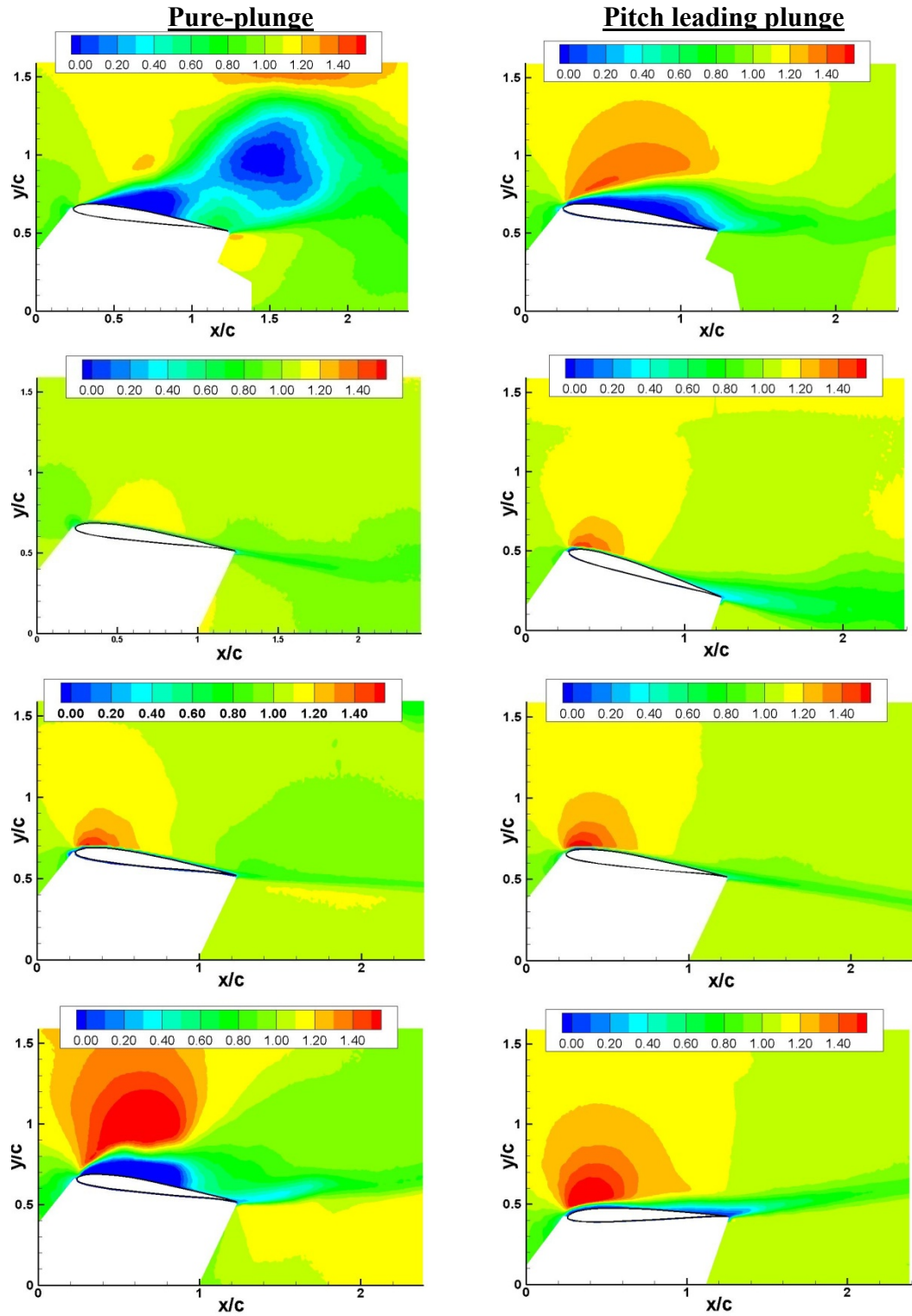
Figure 42: Compare velocity (u/U$_\infty$) contour plots of u for pure-plunge and pitch leading plunge at same reduced frequency, k = 0.25 and Re = 60x10^3.

Pure-pitch   **Pitch leading plunge**
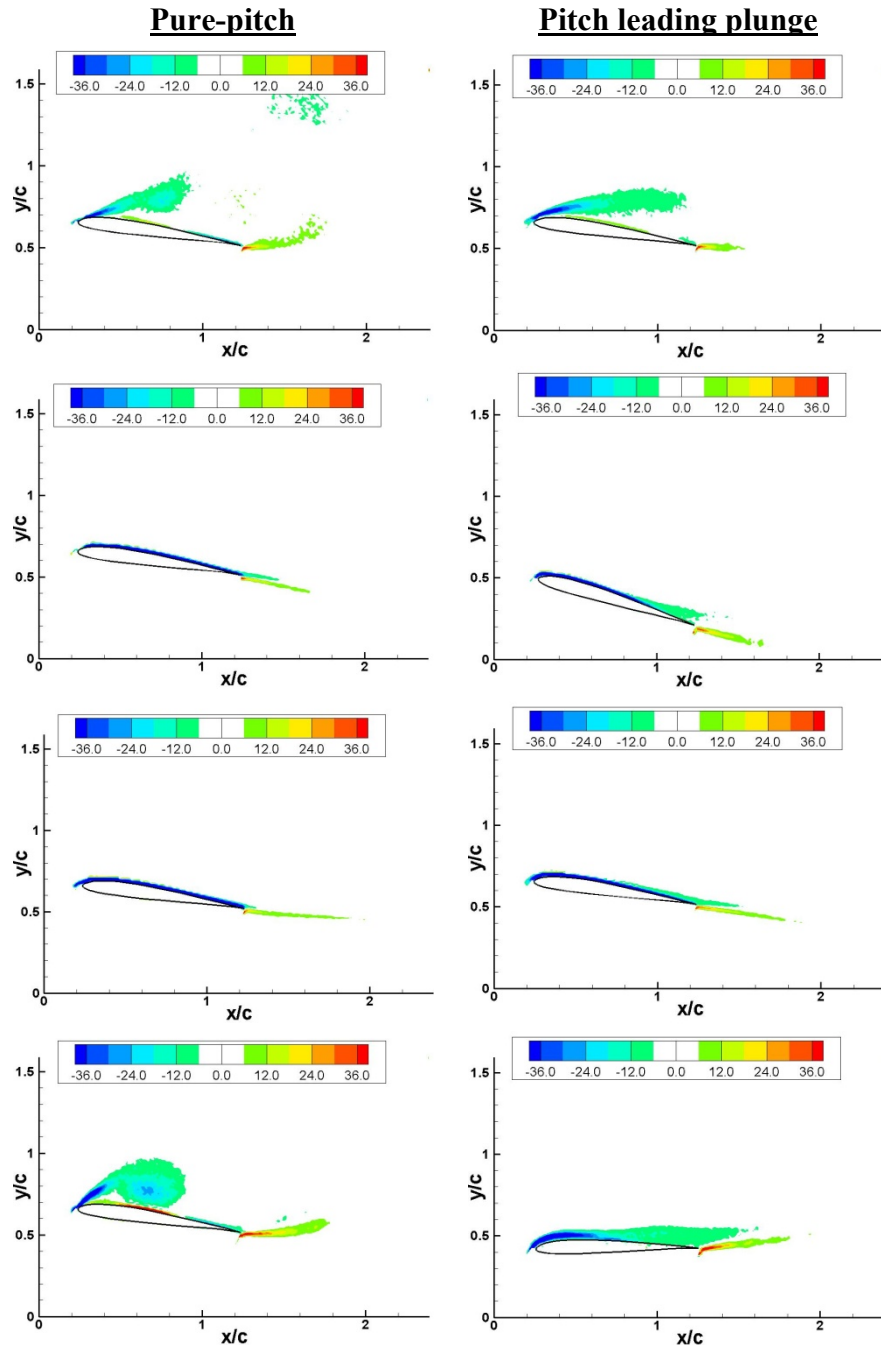
**Figure 43: Compare vorticity ($\omega_z/U_\infty/c$) contour plots of pure-plunge and pitch leading plunge at same reduced frequency, $k = 0.25$.**
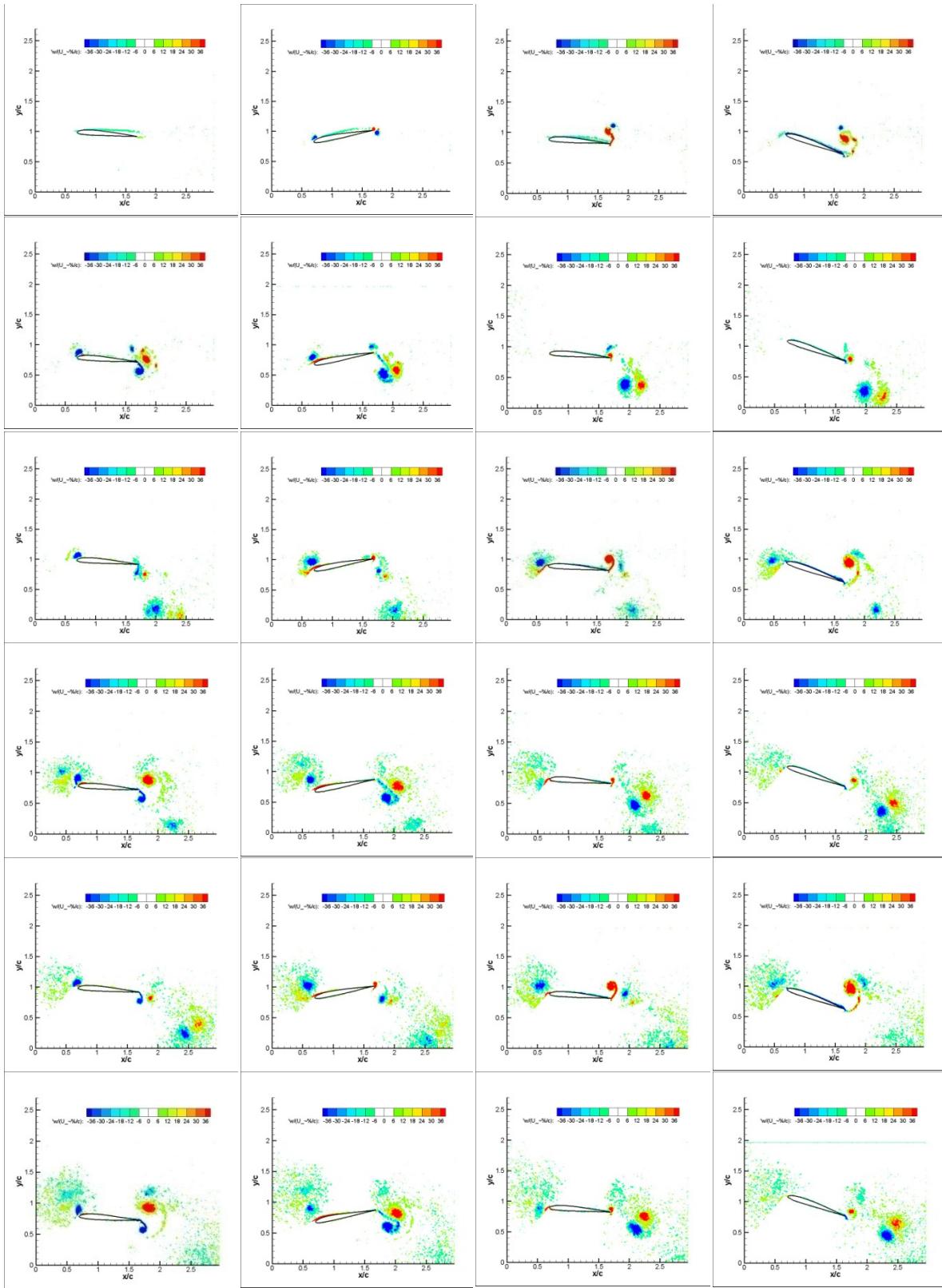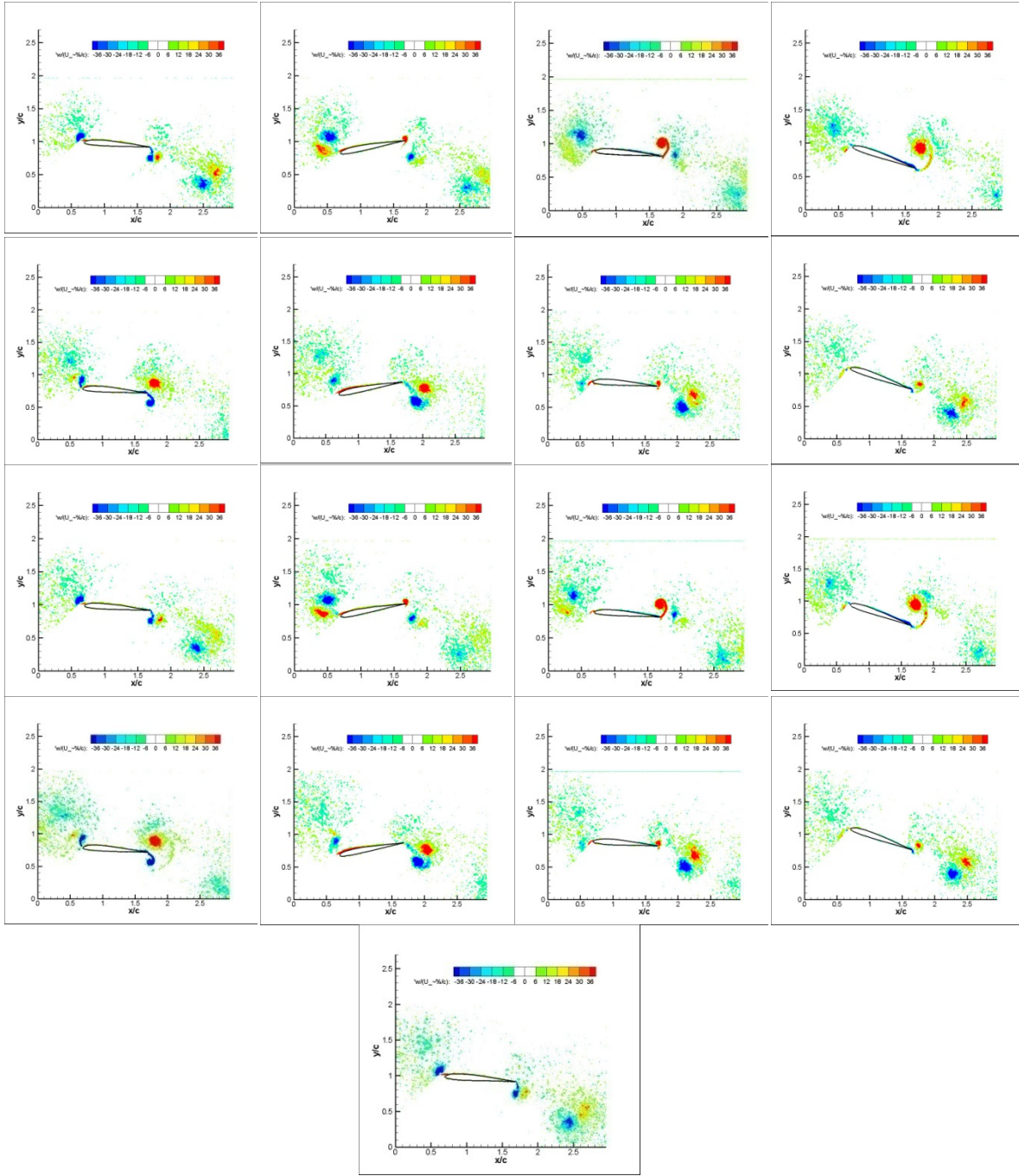
Figure 44: Mixed frequency case, vorticity ($\omega_z/U_\infty/c$) contour plots (rotation about 0.5c and frequency offset for plunge and pitch).

References

Adrian, Gharib, Merzkirch, Rockwell, & Whitelaw. (1998). *Particle image velocimetry: a practical guide.* Germany: Springer-Verlag Berlin Heidelberg.

Adrian, R. (2005). Twenty years of particle image velocimetry. *Experiments in Fluids* , pp.159-169.

Anderson, J., Streitlien, K., Barrett, D., & Trientafyllou, M. (1998). Oscillating foils of high propulsive efficiency. *Journal of Fluid Mechanics, Vol.360* , pp.41-72.

Erm, L. (2006). Development of a dynamic testing system for a water tunnel. *24th AIAA Applied Aerodynamics Conference.* San Francisco, CA: AIAA-2006-3879.

H2W Technologies, Inc. (2007). *SR Positioning Stage*. Retrieved January 12, 2008, from H2W Technologies: http://www.h2wtech.com/srstage.htm

Jeon, D. (2000, May 19). On cylinders undergoing one- and two-degree of freedom forced vibrations in a steady flow. *PhD dissertation.* . Pasadena, CA: Graduate Aeronautical Laboratories California Institute of Technology.

Kaplan, S., Altman, A., & Ol, M. (2007). Wake vorticity measurements for low aspect ratio wings at low reynolds number. *Journal of Aircraft, Vol.44, No.1, January-February* , pp.241-251.

Kramer, B. (2002). Experimental evaluations of superposition techniques applied to dynamic aerodynamics. *40th AIAA Aerospace Sciences Meeting and Exhibit.* Reno, NV: AIAA-2002-0700.

Lai, J., & Platzer, M. (1999). Jet characteristics of a plunging airfoil. *AIAA Journal, vol.37, No.12, Dec.* , pp.1529-1537.

Lian, Y., Ol, M., & Shyy, W. (2008). Comparative of pitch-plunge airfoil aerodynamics at transitional Reynolds number. *46th AIAA Aerospace Sciences Meeting and Exhibit.* Reno, NV: AIAA 2008-652.

Maresca, C. J., Favier, D. J., & Rebont, J. M. (1981). Unsteady aerodynamics of an airfoil at high angle of incidence performing various linear oscillations in a uniform stream. *Journal of the American Helicopter Society, Vol.26, Apr. 1981* , pp.40-45.

McCroskey, W. J. (1981). *The phenomenon of dynamic stall.* NASA Ames Research Center. NASA TM 81264.

McGowan, G., Gopalarathnam, A., Ol, M., Edwards, J., & Fredberg, D. (2008). Computation vs. experiment for high frequency low-Reynolds number airfoil pitch and plunge. *46th AIAA Aerospace Sciences Meeting and Exhibit.* Reno, NV: AIAA-2008-653.

Melling, A. (1997). Tracer particles and seeding for particle image velocimetry. *Measurement Science & Technology,No.8* , pp.1406-1416.

Office of the Assistant Secretary of Defense. (1997, December 12). *DARPA selects micro air vehicle contractor.* Retrieved December 12, 2008, from U.S. Department of Defense News Release No. 676-97: http://www.defenselink.mil/releases/release.aspx?releaseid=1538

Ohmi, K., Coutanceau, M., Daube, O., & Loc, T. (1991). Further experiments on vortex formation around and oscillating and translating airfoil airfoil at large incidences. *Journal of Fluid Mechanics, Vol.225* , pp.607-630.

Ohmi, K., Coutanceau, M., Loc, T., & Dulieu, A. (1990). Vortex formation around and oscillating and translating airfoil airfoil at large incidences. *Journal of Fluid Mechanics, Vol.211* , pp.37-60.

Ol, M. (2007). Vortical Structures in High Frequency Pitch and Plunge at Low Reynolds Number. *37th AIAA Fluid Dynamics Conference and Exhibit.* Miami, FL: AIAA 2007-4233.

OSHA, O. S. (2007). *Occupational safety and health guidelines for titanium dioxide.* Retrieved August 20, 2007, from U.S Department of Labor: http://www.osha.gov/SLTC/healthguidelines/titaniumdioxide/recognition.html

Selig, M. S. (2006 , 11 29). *Airfoil Coordinates Database - Version 2.0.* Retrieved 10 14, 2007, from UIUC : http://www.ae.uiuc.edu/m-selig/ads/coord_database.html

Tecplot 360 . (2006). Bellevue, Washington, U.S.A.: Tecplot, Inc.

Webb, C., Dong, H., & Ol, M. (2008). Effects of unequal pitch and plunge airfoil motion frequency on aerodynamic response. *46th AIAA Aerospace Sciences Meeting and Exhibit.* Reno, NV: AIAA 2008-582.

Wernert, P., Koerberg, G., Wietrich, F., Raffel, M., & and Kompenhans, J. (1997). Demonstartion by PIV of the non-reproductibility of the flow field around an airfoil pitching under deep dynamic stall conditions and consequences thereof. *Aerospace Science and Technology, No.2* , pp.125-135.

Westerweel, J. (1997). Fundamentals of digital particle velocimetry. *Measurement Science & Technology, No.8* , pp.1379-1392.

Willert, C., & Gharib, M. (1991). Digital particle velocimetry. *Experiments in Fluids, Vol.10* , pp.181-193.

REPORT DOCUMENTATION PAGE

Form Approved
OMB No. 0704–0188

1. REPORT DATE (DD–MM–YYYY)	2. REPORT TYPE	3. DATES COVERED (From — To)
27–04–2008	Master's Thesis	Aug 2007 — Mar 2008

4. TITLE AND SUBTITLE

PIV-Based Examination of Deep Stall on an Oscillating Airfoil

5a. CONTRACT NUMBER

5b. GRANT NUMBER

5c. PROGRAM ELEMENT NUMBER

6. AUTHOR(S)

Daniel E. Fredberg, 2d Lt, USAF

5d. PROJECT NUMBER

5e. TASK NUMBER

5f. WORK UNIT NUMBER

7. PERFORMING ORGANIZATION NAME(S) AND ADDRESS(ES)

Air Force Institute of Technology
Graduate School of Engineering and Management (AFIT/EN)
2950 Hobson Way
WPAFB OH 45433-7765

8. PERFORMING ORGANIZATION REPORT NUMBER

AFIT/GAE/ENY/08-M09

9. SPONSORING / MONITORING AGENCY NAME(S) AND ADDRESS(ES)

AFRL/RBAA
Attn: Dr. Michael V. OL
2130 8th St., Bldg 45
Wright-Patterson AFB, OH 45433-7542   DSN: 255-1196

10. SPONSOR/MONITOR'S ACRONYM(S)

11. SPONSOR/MONITOR'S REPORT NUMBER(S)

12. DISTRIBUTION / AVAILABILITY STATEMENT

APPROVED FOR PUBLIC RELEASE; DISTRIBUTION UNLIMITED

13. SUPPLEMENTARY NOTES

14. ABSTRACT

A number of studies suggest that the deep stall flow fields produced by a pure-pitch and a pure-plunge oscillating airfoil are equivalent, when effective angles of attack are matched. This assumption is examined using particle image velocimetry (PIV). Sinusoidal oscillations of a pure-plunge and pure-pitch airfoil with matched reduced frequency $k = 3.93$ and with kinematically equivalent amplitudes of effective angle of attack are comparatively examined using results of PIV in a free surface water tunnel at AFRL/RB, Wright Patterson AFB. Experiments were conducted at Re = 10,000 and Re = 40,000, based on free stream velocity and airfoil chord, in order to observe the legitimacy of assuming Reynolds number insensitivity on the respective flow fields. Comparisons are made to computational flow field results collected in a separate, but coordinated, CFD effort. Results for both the pure-plunge case and the pure-pitch case confirm the Reynolds number insensitivity for the high frequency motions researched here. The resulting flow fields for pure-plunge case and the pure-pitch case were vastly different. Experimental results for the pure-plunge case closely resembled those achieved by computation. However, the pure-pitch case experimental and computation results were dissimilar even after considering possible wall effects of the water tunnel. The flow field disagreement between the two motions is not surprising considering trailing edge kinematic dissimilarities.

15. SUBJECT TERMS

Particle image velocimetry, oscillating airfoils, water tunnel, deep stall, dynamic stall, oscillating airfoil, vortex shedding

16. SECURITY CLASSIFICATION OF:

a. REPORT	b. ABSTRACT	c. THIS PAGE
U	U	U

17. LIMITATION OF ABSTRACT

UU

18. NUMBER OF PAGES

123

19a. NAME OF RESPONSIBLE PERSON
Dr. Mark F. Reeder

19b. TELEPHONE NUMBER (Include Area Code)
(937) 255-3636, ext 4530; e-mail:
mark.reeder@afit.edu

Standard Form 298 (Rev. 8–98)
Prescribed by ANSI Std. Z39.18